DEVELOPMENT OF A PHYSICS BASED METHODOLOGY FOR THE PREDICTION OF ROTOR BLADE ICE FORMATION

A Dissertation
Presented to
The Academic Faculty

by

Jeewoong Kim

In Partial Fulfillment
of the Requirements for the Degree
Doctor of Philosophy in the
School of Aerospace Engineering

Georgia Institute of Technology
December 2015

DEVELOPMENT OF A PHYSICS BASED METHODOLOGY FOR THE PREDICTION OF ROTOR BLADE ICE FORMATION

Approved by:

Dr. Lakshmi N. Sankar, Advisor
School of Aerospace Engineering
Georgia Institute of Technology

Dr. J. V. R. Prasad
School of Aerospace Engineering
Georgia Institute of Technology

Dr. Daniel P. Schrage
School of Aerospace Engineering
Georgia Institute of Technology

Dr. Ritu P. Marpu
Office in Orlando, FL
CD-adapco

Dr. Jeff Jagoda
School of Aerospace Engineering
Georgia Institute of Technology

Date Approved: October 29, 2015

Dedicated to my parents, parent-in-law, brother and wife

for their unconditional love and support

ACKNOWLEDGEMENTS

I wish to thank God of Ebenezel for his grace that was with me.

I would like to express my sincere and heartfelt appreciation to my advisor and mentor, Dr. Lakshmi N. Sankar, for his support and guidance. His encouragement and kind advice enabled me to accomplish this research work. It was my great pleasure to pursue my Ph. D under his guidance and advice.

I would like to thank my thesis reading committee members, Dr. Daniel P. Schrage, Dr. Jeff Jagoda, Dr. J.V.R Prasad and Dr. Ritu P. Marpu. for providing suggestions for improvement of the thesis document. Their valuable comments and suggestions helped me produce research material worthy of archival.

I also would like to thank Richard E. Kreeger (NASA Glenn Research Center) and Tonja K. Reinert (Boeing) for providing me with the data for simulations. My sincere thanks to our collaborators and industry partners, Dr. Narducci, Robert P (Boeing), Wright, Jason (Boeing) for their suggestions and comments.

I would like to thank all my colleagues in the CFD lab, Dennis Garza, Eliya Wing, Robert Lee, Alpha Bah, Muhammad Ali, Chong Zhou, Zhihang Liu, Rajeeve Atluri, Stephen Marone, and Nana Obayashi for their friendship and support during my years in the lab. Special thanks to Dr. Byung-young Min, Dr. Nandita Yeshala and Dr. Nischint Rajmohan for their comments and encouragement.

I would especially like to thank Dr. Yung H. Yu, Dr. Soo Hyung Park, my former advisor for my Master's degree, and Dr. Yung-Hwan Byun in Konkuk University for their continuous encouragement and support.

I would like to thank all of my Korean friends, both, in the United States and Korea, for their support and friendship.

Last but not the least; I have to say, I am greatly indebted to my parents who have been the pillars of support throughout my life; and their unconditional love and affection has been a great source of strength and confidence. This thesis work is dedicated to them.

TABLE OF CONTENTS

LIST OF TABLES

LIST OF FIGURES

NOMENCLATURE

A, B, C	Flux Jacobian matrices
c	Chord
CF	Chordwise force
C_d	Drag force coefficient $(D/(q_{ref}c_{ref}))$
C_l	Lift force coefficient $(L/(q_{ref}c_{ref}))$
$C_N M^2$	Sectional normal force coefficient $(d(NF)/dr/(0.5 * \rho_\infty * a_\infty^2 * c_{ref}))$
C_p	Specific heat at constant pressure, Pressure coefficient $((p - p_\infty)/q_{ref})$
C_{PM}	Pitching moment coefficient $(PM/(\rho_\infty A V_{tip}^2 R))$
C_Q	Torque coefficient $(Q/(\rho_\infty A V_{tip}^2 R))$
C_T	Thrust coefficient $(T/(\rho_\infty A V_{tip}^2))$
$C_x M^2$	Sectional chord-wise force coefficient $(d(CF)/dr/(0.5 * \rho_\infty * a_\infty^2 * c_{ref}))$
D	Drag force
e	Total energy per unit volume, Hinge offset
E, F, G	Inviscid flux matrices
H	Source vector
I	Identity matrix
J	Jacobian of transformation
k	Thermal conductivity, Reduced frequency
L	Lift force, Reference length
L, D, U	Lower, diagonal and upper block triangular matrix
m	Mass
M	Mach number

NF	Normal force
N_b	Number of blade, Mass faction of water lost
p	Pressure
Pr	Prandtl number
Pr_t	Turbulent Prandtl number
Psi	Azimuth angle
q_{ref}	Dynamic pressure ($\frac{1}{2}\rho_\infty V_{tip}^2$ for rotor analysis)
Q	State variable vector, Vorticity and strain rate balance, Torque
r	Radial location
R	Rotor radius
Re	Reynolds number
RHS	Shorthand notation for the terms on the right hand side for any equation
T	Temperature, Thrust
u, v, w	Cartesian components of velocity
U, V, W	Contravarient velocity
V, U	Velocity
x, y, z	Cartesian coordinates

Greek Symbols

α	Angle of attack, Volume fraction
α_s	Shaft tilt angle
β	Local collection efficiency, Flapping angle
δ	Central difference operator, Boundary layer thickness
Δ	Difference, Grid spacing
γ	Specific heat ratio

μ	Viscosity, Advance ratio
ρ	Density
σ	Surface tension, Solidity
ξ, η, ζ	Curvilinear coordinates
ψ, Ψ	Azimuth angle
Ω	Rotational speed

Subscripts

0	Amplitude of zero-th harmonic
$1c, 1s$	Amplitude of first harmonic
a	air
i, j, k	Indices in three coordinate directions
tip	Value at the blade tip
tw	Twist
w	water
x, y, z	Derivatives with respect to Cartesian coordinates
ξ, η, ζ	Derivatives with respect to curvilinear coordinates
∞, inf, ref	Reference value

Superscripts

-1	Inverse matrix
n, n+1	Time level

Acronyms and Abbreviations

2-D	Two Dimensional
3-D	Three Dimensional

AUSMPW	Advection Upstream Splitting Method with Pressure Weight Function
BC	Boundary Condition
BSL	Baseline
CFD	Computational Fluid Dynamics
DES	Detached Eddy Simulation
FDS	Flux Difference Splitting
GCL	Geometric Conservation Law
GENCAS	Generic Numerical Compressible Airflow Solver
HRKES	Hybrid RANS-KES
KES	Kinetic Eddy Simulation
LU-SGS	Lower-Upper Symmetric Gauss Seidel
LWC	Liquid Water Conent
MUSCL	Monotone Upstream-centered Scheme for Conservation Laws
PDE	Partial Differential Equation
RANS	Reynolds Averaged Navier-Stokes
RHS	Right Hand Side
RPM	Revolutions-per-minute
SA, S-A	Spalart-Allmaras
SIMICE	Simulated Ice
SST	Shear Stress Transform
WENO	Weighted Essentially Non-Oscillatory

SUMMARY

Modern helicopters, civilian and military alike, are expected to operate in all weather conditions. Ice accretion adversely affects the availability, affordability, safety and survivability. Availability of the vehicle may be compromised if the ice formation requires excessive torque to overcome the drag needed to operate the rotor. Affordability is affected by the power requirements and cost of ownership of the deicing systems needed to safely operate the vehicle. Equipment of the rotor blades with built-in heaters greatly increases the cost of the helicopter and places further demands on the engine. The safety of the vehicle is also compromised due to ice shedding events, and the onset of abrupt, unexpected stall phenomena attributable to ice formation.

Given the importance of understanding the effects of icing on aircraft performance and certification, considerable work has been done on the development of analytical and empirical tools, accompanied by high quality wind tunnel and flight test data.

In this study, numerical studies to improve ice growth modeling have been done by reducing limitations and empiricism inherent in existing ice accretion models. In order to overcome the weakness of Lagrangian approach in unsteady problem such as rotating blades, a water droplet solver based on 3-D Eulerian method is developed and integrated into existing CFD solver. Also, the differences between the industry standard ice accretion analyses such as LEWICE and the ice accretion models based on the extended Messinger model are investigated through a number of 2-D airfoil and 3-D rotor blade ice accretion studies. The developed ice accretion module based on 3-D Eulerian water

droplet method and the extended Messinger model is also coupled with an existing empirical ice shedding model.

For de-icing analysis, LEWICE uses 2-D strip theory, and solves the heat conduction equations on a Cartesian grid. A fully 3-D heat conduction analysis that acknowledges curvature of the heat elements, and the finite spanwise extent of the heating elements has been developed in order to improve de-icing modeling.

A series of progressively challenging simulations have been carried out. These include ability of the solvers to model airloads over an airfoil with a prescribed/simulated ice shape, collection efficiency modeling, ice growth, ice shedding, de-icing modeling, and assessment of the degradation of airfoil or rotor performance associated with the ice formation. While these numerical simulation results are encouraging, much additional work remains in modeling detailed physics important to rotorcraft icing phenomena. Despite these difficulties, progress in assessing helicopter ice accretion has been made and tools for initial analyses have been developed.

CHAPTER 1

INTRODUCTION

1.1 Background

Modern helicopters, civilian and military alike, are expected to operate in all weather conditions. Ice accretion adversely affects the availability, affordability, safety and survivability. Availability of the vehicle may be compromised if the ice formation requires excessive torque to overcome the drag needed to operate the rotor. Affordability is affected by the power requirements and cost of ownership of the deicing systems needed to safely operate the vehicle. Equipment of the rotor blades with built-in heaters greatly increases the cost of the helicopter and places further demands on the engine. The safety of the vehicle is also compromised due to ice shedding events, and the onset of abrupt, unexpected stall phenomena attributable to ice formation.

Given the importance of understanding the effects of icing on aircraft performance and certification, considerable work has been done on the development of analytical and empirical tools, accompanied by high quality wind tunnel and flight test data. AGARD Report 344 [1] and Gent [2] provide an excellent review on aircraft icing research. The icing research tunnel (IRT) at the Lewis Research Center was built by NACA in the early 1940's. Since then the systematic research in ice accretion and subsequent aerodynamic performance degradation has been performed. Although there were initial efforts for icing simulation in the late 1920's and early 30's [3], an important foundation and early key milestone in the numerical analysis of aircraft icing were built by the early works of Hardy [4], Messinger [5] and Langmuir & Blodgett [6]. Their early works laid the mathematical foundation but were restricted to simple geometries such as cylinders and spheres. The theoretical research started to focus on more representative geometries such as airfoils, wings and helicopter rotors since the late 1970s.

Sophisticated computer simulations of ice accretion processes and performance degradation have been performed with the advent of high speed computers. In recent years, the certification of aircraft flying in icing condition has been transformed from an dependence on wind tunnel and flight tests to design by analysis with verification by actual tests because numerical simulation is more advantageous in investigating a much broader range of icing environments in a safe and efficient manner. Because it is very expensive and time consuming to test and certify an aircraft for its entire range of operating conditions, it is customary to use icing tunnel test data bench mark configurations and computational data to screen and reduce the number of flight test operating conditions. Despite this long history of icing research, a number of unresolved issues related with the physical phenomena are still remained in the process of icing simulation. Improvement of prediction capability for ice accretion and performance degradation requires understanding of the underlying physical phenomena.

1.2 Effect of Icing on Vehicle Performance and Handling

The most prominent effect of ice formation on lifting surfaces is variation of the lifting characteristic of a wing or rotor. Ice will cause drastic decrease of the maximum lift and even the slop of lift curve with respect to angle of attack because nose shapes of wing sections are essentially sharpened by the usual ice forms or become rough due to icing phenomena. Also, ice can cause premature flow separation downstream of the ice shape giving rise to stall at considerably lower angles of attack. At the same time the drag of wing or rotor blade will increase and result in the change of drag polar. Typical example of performance degradation of wing due to ice accretion is seen in Fig. 1.1.

In fixed wing case, the longitudinal stability behavior is also affected by the ice accretion on wing [1]. Due to the ice formation, the balance obtained from trim condition without ice becomes upset. The aircraft will become mistrimmed in the nose-up direction

as the size of ice grows. This will result in, for example, rapid pitch up during the take-off and require an abnormal push force in order to keep the speed during the climb.

While icing affects fixed wing and rotary wing vehicles alike, rotorcraft are more vulnerable to ice accretion. It is hard to analyze ice accretion on rotor blade and its subsequent effect on helicopter performance in the straightforward manner used for a fixed wing aircraft. The flowfield is highly modified due to ice accretion. This causes reduction of sectional lift coefficient and modification of sectional pitching moment [7, 8, 9]. The most critical effect of rotor blade icing is the dramatic increase of blade profile drag. Ice usually is not formed uniformly on the blade surface. A rough or sometimes jagged structure which causes premature flow separation is created. Due to this, required torque also is increased and can quickly reach the limits of transmission or engine [10, 11]. Another hazardous effect of rotor icing is the deterioration of normal autorotational qualities. It will be difficult to maintain the minimum autorotational RPM in case of power loss [12]. U.S Army conducted a study with Bell UH-1 Huey and found that ice accretion of one-half inch or greater will be accompanied by a 5-6 pound per square inch (psi) torque increase over the no-ice power requirement [12].

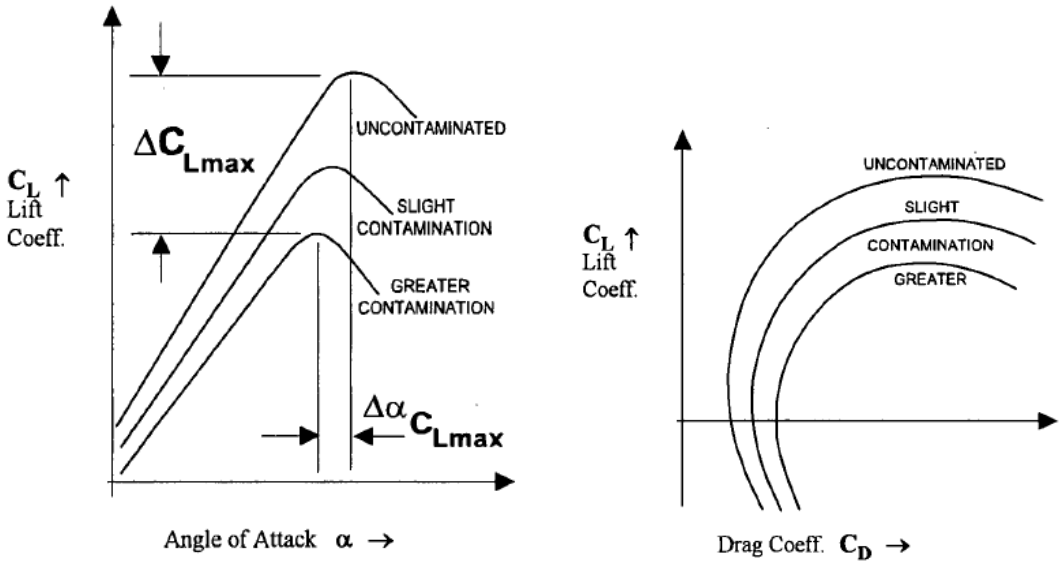

Figure 1.1 Effect of Icing on Lift (left) and Drag (right) [1].

There is an addition issue related to ice shedding. The problem occurs due to the high rotational speed of the rotor. Especially near the rotor blade tip, accreted ice has high centrifugal force which is providing a natural de-icing mechanism. Although this is beneficial for helicopter theoretically, the problematic thing is the asymmetric ice shedding from all blades. This will cause rotor imbalance and subsequent severe vibrations in the fuselage. In addition, shed ice particles have potential risk to the fuselage, engine or empennage.

1.3 Ice Accretion Physics

The AGARD Report 344 [1] and Gent [2] describe the basic physics of ice accretion and the different types of ice. Aircraft icing is defined as flight in cloud at temperatures at or below freezing when supercooled water droplets impinge and freeze on the unprotected areas on which they impact [1]. Various factors such as ambient temperature, speed of body, LWC and size of droplets in the cloud affect the rate and amount of ice accretion on unheated aircraft structures.

The ice accretion can be divided into two distinct aspects. The first part is the rate at which the water is captured by the surface. The amount of water collected is determined by the product of collection efficiency, LWC and the speed at which the body is travelling through the cloud. Collection efficiency is affected by the size and shape of body, angle of attack, water droplet size and airspeed. Ambient temperature and pressure have a limited effect on it.

The rate at which the collected water on the surface of body will freeze to form an ice is the second part of ice accretion. The water droplets striking the forward-facing surfaces freezes either partially or completely as the results of a the heat transfer. The heat transfer includes kinetic heating, convective heat transfer, evaporative cooling, the rate of latent heat of release and a number of small contributions. The impinging water releases the latent heat of fusion. This heat tends to warm the ice and surface. This

warming tendency is counteracted by heat losses normally from convection and evaporation. The convective heat transfer is largely affected by the shape of body, airspeed, roughness of iced surface and ambient temperature difference between the surface and the local air temperature. The evaporative cooling is determined by vapor pressure of the water which depends on temperature and pressure at the surface.

At combinations of low temperature, low airspeed and low LWC, the temperature of the accreted ice remains below freezing temperature and the impinging droplets freeze completely. This type of accretion is called rime ice (Figure 1.2). Rime ice has a streamlined and an opaque milky appearance. The process of this type of ice is relatively simple because the impinging droplets freezes and remain on the surface they strike, that is the freezing fraction is unity. Accurate prediction of droplet trajectories is critical for the simulation of rime ice.

If all of the impinging water do not freeze, that is the freezing fraction is less than unity, the remaining so-called 'runback' water runs aft along the surface and freeze somewhat downstream. This kind of ice accretion is called glaze ice (Figure 1.3). Glaze ice has more complex shape often with large double-horns (2D) or lobster-tail (3D) which may jeopardize the aerodynamic characteristics. Glaze ice is formed at conditions with warm temperature (i.e. close to freezing), high speed and high LWC. At high LWC condition, the rate of convective heat loss is insufficient to remove all the latent heat released so that the freezing fraction becomes less than unity. Due to the complex accretion process, modern ice accretion codes still have difficulty in predicting the glaze ice shapes accurately.

A slushy ride of ice termed 'beak' ice (Figure 1.4) is formed in the tip region of helicopter blades at high speed and warm temperature, close to freezing temperature. The only place where ice can grow is in the suction region on the upper surface of the airfoil close to the leading edge. Cooling due to adiabatic expansion mitigates the effect of kinetic heating.

It is possible for all three types of ice to be present at the same time in case of helicopter rotor blades. There is variation in the local velocity and surface temperature along the radial direction of blade. Rime ice is generally formed at the inboard region. Glaze ice is presented further outboard and beak ice can form in the tip region. Some portion of the blade tip may remain clean due to kinetic heating effect at warmer temperatures. Figure 1.5 shows a typical ice accretion profile on rotor blade.

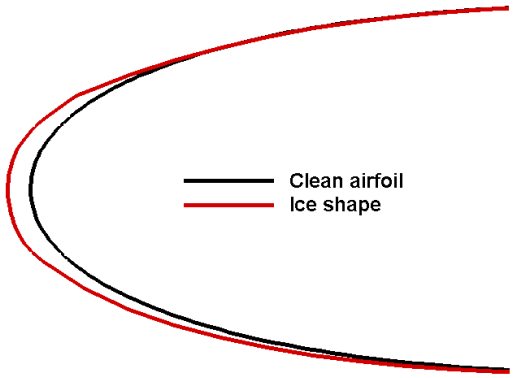

Figure 1.2 Rime Ice.

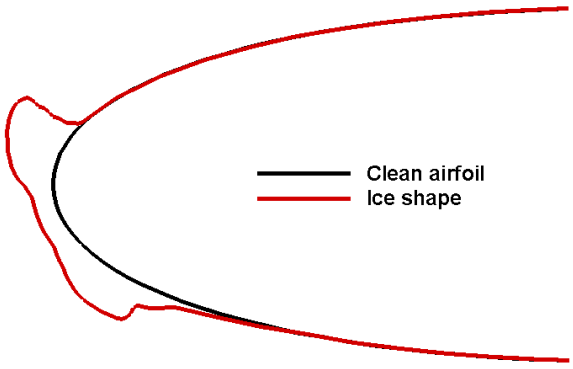

Figure 1.3 Glaze Ice.

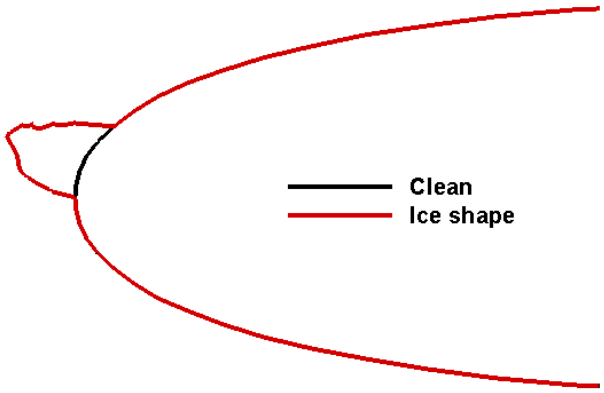

Figure 1.4 Beak Ice.

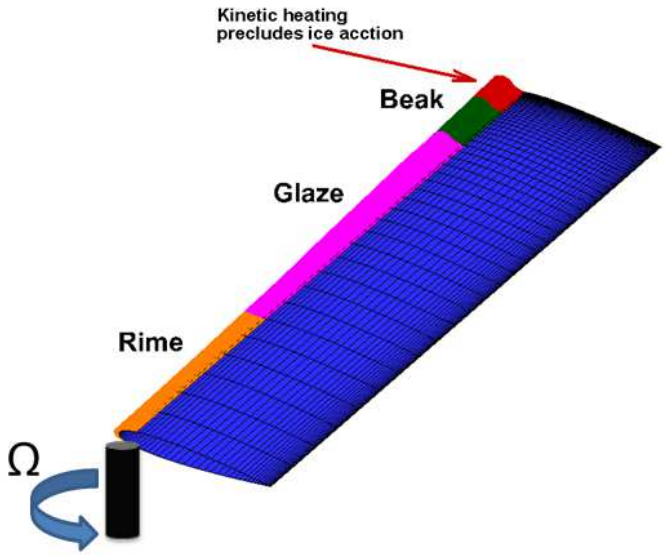

Figure 1.5 Typical Ice Accretion on Rotor Blade.

1.4 Previous Research

1.4.1 Experimental Study

Before the advent of high speed computers, icing research for helicopters was focused on wind tunnel and flight tests. In 1981 and 1983, icing and deicing tests have been conducted with an model rotor of the Eurocopter Super Puma in the SIMA wind tunnel at France [13]. The influence of different parameters such as water droplet size, static temperature and water flux density is investigated. It was found that speed and temperature significantly affect ice shape. Flight tests in icing condition were performed on a UH-1H helicopter in level flight during 1983-84 as part of the joint NASA / Army HIFT (Helicopter Icing Flight Test) program [14]. Considerably different ice shapes from those of the hover case were observed. The reason for this was explained by the unsteadiness of flow field. In 1988, the first model rotor icing tests have been done with the OH-58 Tail Rotor Rig in the NASA Lewis Research Center Icing Research Tunnel (IRT) [15]. It verified the usefulness of the Icing Research Tunnel as a facility for obtaining meaningful data for rotating systems. After that, several wind tunnel tests have been conducted with a heavily instrumented subscale model of a generic helicopter main rotor by NASA at the IRT [16-20]. The effects of temperature, LWC, median droplet diameter, advance ratio, shaft angle, tip Mach number (rotor speed) and weight coefficient are investigated. From 2006 to 2008, the Anti-icing Material International Laboratory (AMIL) in Canada performed sub-scale model rotor icing tests in collaboration with Bell Helicopter Textron to study ice physics, low energy de-icing systems and hydro- or ice-phobic coatings use for small helicopters [21]. Fortin [21] proposed an analysis procedure for ice shedding and showed correlation between prediction and experiment. In 2009, model rotor icing tests in hover have been conducted by the Pennsylvania State University [22]. Prediction of ice shapes and shedding has been done. Brouwers [22] used a similar approach Fortin used for shedding analysis.

1.4.2 Numerical Study

Several ice accretion tools have been developed internationally to predict ice shapes for various conditions on structures to reduce tunnel time and flight test entries. Some of representative ice accretion programs are LEWICE [23], ONERA [24 - 26], FENSAP-ICE [27], CANICE [28,29]. Characteristics of these ice accretion codes are summarized in Table 1.1. Most of icing codes are primarily two-dimensional in nature, although some have been expanded into three dimensions, such as LEWICE 3D, FENSAP-ICE and ONERA 3D. Ice accretion programs may use a 2D or quasi-3D potential flow solver to obtain flowfield or use a high fidelity code such as a Navier-Stokes code to capture viscous and unsteady effects. In order to get information about how much water droplet is captured on surface, Lagrangian or Eulerian approach are used. For thermodynamic analysis of ice accretion process, most ice accretion codes are based on Messinger [5] model.

Table 1.1: Characteristics of Ice Accretion Codes

CODE	Characteristics			
	Boundary Layer	Lam-Turb Transition	Onset / Length	Droplet Trajectory
LEWICE [23]	integral	abrupt	Re_{ks}	Lagrangian
ONERA [24]	integral (Makkonen)	abrupt	Re_{ks}	Lagrangian
ONEAR [25]	differential			Lagrangian
CANICE [28,29]	differential (Cebeci [30])	intermittency (Chen,Thyson [31])	w/o freestream turbulence effect (Michel [32])	Lagrangian
ONERA 3D[20]	integral (Makkonen)			Eulerian
FENSAP-ICE [27]				Eulerian

Current state of the art computational methodologies for modeling aircraft and rotorcraft icing follow the present approach.

1. The external aerodynamics of the clean, un-iced configuration is first modeled.
2. The velocity field from the computations is fed into a Lagrangian particle trajectory analysis, or an Eulerian droplet convection model, to determine the collection efficiency, which a measure of the amount of water that enters the viscous layer close to the surface with a possibility of subsequent freezing.
3. The surface pressure distribution is next used to model the boundary layer growth and compute the surface skin friction distribution. Reynolds analogy is usually invoked to convert the surface skin friction distribution to the surface heat transfer rate.
4. As a last step, a finite volume analysis is done within the viscous layer near the solid surface to solve the water mass balance and energy balance equations, with and without heating within the solid surface underneath.
5. At selected time levels, the resulting ice shape is added to the solid surface to establish an iced configuration.

Steps 1-5 are repeated as often as needed until the total time of ice accretion is reached.

In step 2, there have been two primary approaches for the prediction of surface droplet impingement distributions- Lagrangian and Eulerian methods. Da Silveira et al [33] have conducted an evaluation of these methods and found both methods to be equally effective. LEWICE or LEWICE3D are representative examples of industry-standard icing programs that use a Lagrangian approach to compute droplet trajectories through the air, and have been shown to be highly effective [34,35]. In Lagrangian approaches, computational cost is reduced by performing the simulation of ice accretion only at a few selected strips in the configuration, as opposed to the full 3D simulation where collection efficiency is computed over the entire surface.

In the Eulerian approach, (e.g. FENSAP-ICE [27,36]) the conservation of mass and momentum of the droplets are computed simultaneously with the flow field solution, by solving two additional governing equations for the volume fraction of water and the particle velocities. These equations are solved on the same CFD mesh. The mean flow may be unsteady, and the solid surfaces may be in relative motion. Most Lagrangian approaches, on the other hand, assume or require the flow field to be steady. For this reason, an Eulerian method is more attractive for modeling rotorcraft icing phenomena.

For the ice accretion, most of codes are based on Messinger model [5]. The original Messinger model is based on one dimensional equilibrium energy balance. It was designed to analyze the conditions that govern the equilibrium temperature of an insulated, unheated surface exposed to icing. It is not possible for Messinger model to capture the transient behavior of an ice accretion because the temperature is set to equilibrium value. This results in lesser freezing fraction than the true freezing fraction [37,38]. Another limitation of Messinger model is that conduction through ice and water layers cannot be accounted for due to the isothermal ice and water layers. Myers [39] proposed a one-dimensional mathematical model, extending the original Messinger Model, describing ice growth due to supercooled fluid impacting on a solid surface. The method solves heat equations in the ice and water layers. A first-order ordinary differential equation of phase change or Stefan condition [37] is also solved at the moving ice/water interface. All of the energy terms of the original Messinger model [5] are considered. Another point of Myers' approach is that instead of solving the full, complex system of equations, a much simpler system is solved because the ice growth rate is considerably slower than the heat conduction rate.

In order to completely prevent, or if not possible, at least minimize and control ice formation on the skin of the aircraft, various de-icing equipments have been developed [40]. One of de-icing equipments is electrothermal heating pads [Figure 1-6]. It can be incorporated into the fabric of the composite materials and allow better heating efficiency

and coverage, without harming the composite materials due to its lower power density, coupled with placement flexibility. Although de-icing system using electrothermal heating pads may be on its way to becoming one of the most efficient methods of ice protection, the design and certification of this protection system through experimental testing are expensive and complex. Some numerical approaches have been developed in the past [41 - 45] to model the phenomenon of in-flight de-icing. Stallabrass [46] first developed one and two dimensional models. After that separate numerical techniques are used in this area [47-50]. Due to the complex phenomenon, de-icing simulation requires precise solution of flowfield, collection efficiency, water film thermodynamics, ice accretion, and heat conduction through the multilayered aircraft skin. Unsteady heat conduction and phase change through the ice layer also have to be adequately modeled.

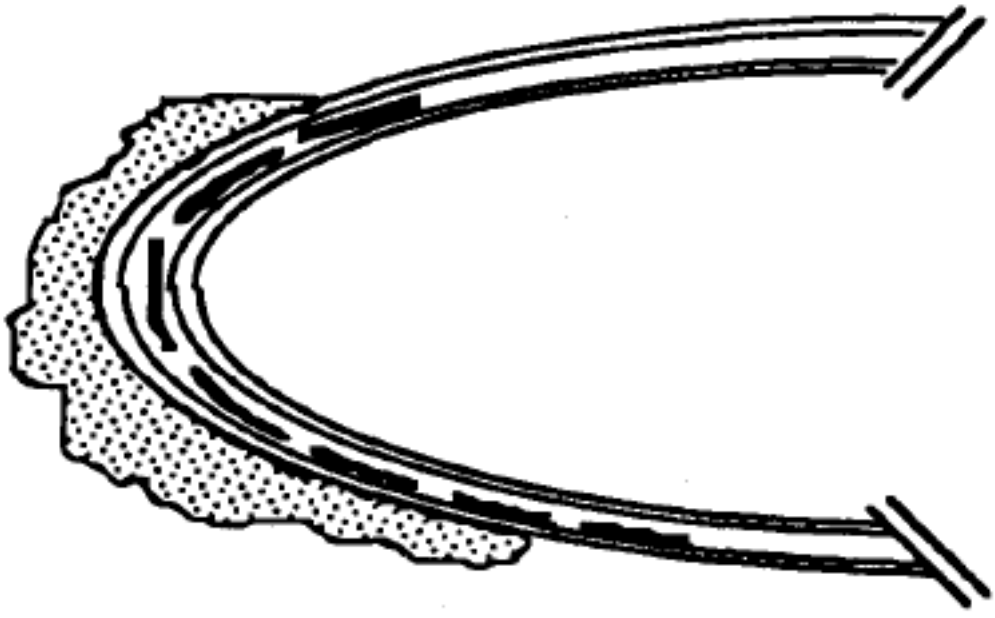

Figure 1.6 Iced Airfoil Equipped with Electrothermal Pads [41].

1.4.3 Studies for Rotorcraft Icing

Despite long history of icing research and several ice accretion modeling tools, rotorcraft icing still remains a challenging problem. Many researchers have developed methodologies that are designed specifically to explore various parts of the rotorcraft icing problem. Flemming [51] performed series of tests with rotorcraft airfoils and formulated 2D airfoil section icing relationships for ice thickness and for changes in aerodynamic force and moment coefficients. The 2D relationships have been incorporated into rotorcraft comprehensive performance prediction codes. Britton [52,53] developed an analytical approach calculating the performance degradation of a helicopter operating in an icing condition. Instead of using an empirical relationship developed by Flemming [51], Interactive Boundary Layer method [54] is used to calculate the aerodynamic coefficients of the iced geometry. Ice shape at each radial location is obtained by LEWICE. Zanazzi [55] did ice accretion simulation and performance prediction of rotor in hover using CFD tools. For the prediction of ice growth, 2D analysis at each radial section base on classical Lagrangian approach and Messinger model is performed. Heat transfer coefficients are obtained by using an integral boundary layer calculation method. Good correlation with experimental ice shape is obtained at blade inboard regions (rime ice). There is deviation at the outboard sections (glaze ice). Bain [56-59], Narducci [60,61] also used similar approach Zanazzi[55] have applied. CFD simulations have been performed to obtain flowfield solution. The velocity field from the CFD computations is fed into a Lagrangian particle trajectory analysis. Ice accretion is done by 2D strip approach.

For rotor blade ice shedding analysis, few numerical simulations are found from literature survey. Scavuzzo et al. [62,63] used finite elements to model ice on a rotating airfoil and subsequently predict the probability of shedding. Bain [59] and Brouwers [22] used a similar approach Fortin used for shedding analysis. The methodology does not use

fracture mechanics. It can predict shedding using the experimentally derived shear stresses as input.

1.5 Motivation and Objectives

CFD based ice accretion simulation has several advantages in terms of safety, efficiency and cost. Scaling is not required. Numerical simulation is reproducible, traceable and upgradeable. Cost for numerical simulation are also continuously decreasing. It is possible to investigate most of situations difficult or not possible to test. Although many studies have been performed for rotorcraft icing problem, improvement of prediction capability for ice accretion and performance degradation are still required. The technical barriers are:

1. Ice accretion modeling is currently being done using 3-D aeromechanics tools coupled to 2-D strip models of ice formation.
   - The models are 2-D, quasi-steady.
   - The models rely on semi-empirical methods for heat transfer from the liquid water droplets to the blade surface.
   - Shedding models qualitatively model the likelihood of shedding using a balance of forces on the ice shape. (centrifugal forces, surface adhesion, and cohesion with neighbor ice elements)
2. The shape of shed ice and the subsequent trajectory are not reliably modeled.

The primary objectives of this study are to:

1. Reduce limitations and empiricism inherent in existing ice accretion, runback-refreeze, and shedding models.
2. Extend the 2-D quasi-steady strip theory analysis to a three-dimensional unsteady approach for the external layers of ice, water, and air as well as the internal airframe structure with embedded heater elements.

3. Validate the improved tools against the baseline LEWICE3D and against NASA and industry supplied icing tunnel and flight test data.

To achieve these goals, the scope of present works are first to replace Lagrangian approach with an 3D unsteady Eulerian approach. The developed water droplet solver is integrated into the existing flow solver. The second work is to reduce empiricism in heat transfer analysis. Most of ice accretion code uses integral boundary layer method to calculate convective heat transfer coefficient by using Reynolds analogy. Empirical equations for skin friction coefficient and heat transfer coefficient are used. Instead of empirical equations for skin friction coefficient, values from high fidelity CFD simulations are used for the prediction of heat transfer coefficient. The third work is to systematically assess the differences between the industry standard ice accretion analyses such as LEWICE and the ice accretion models based on the extended Messinger model. Over the past two decades, Extensions to the classical Messinger model have been proposed by Myers [39] and has been evaluated by Ozgen et al [64]. While these models have the same physical foundation, they differ considerably from each other in the way the boundary layer growth, transition location determination, and surface skin friction are treated. These methods also differ substantially in the way the heat and mass balance equations are modeled. The fourth work is to perform a shedding analysis using ice shapes from the extended Messinger model and compare prediction against past simulations based on LEWICE and icing tunnel test data. The fifth work is to investigate the curvature effect on de-icing simulation. LEWICE uses 2-D strip theory, and Cartesian grids. A fully 3-D heat conduction analysis that acknowledges curvature of the heat elements, and the finite spanwise extent of the heating elements has been developed.

CHAPTER 2

METHODOLOGY

2.1 Icing Model Formulation

Figure 2.1 shows the basic elements of the ice accretion simulation model. The process starts with grid generation and CFD flow analysis for a clean baseline configuration. The droplet solver reads the flow field data and computes the local collection efficiency (β) on the surface. This information is fed into the ice accretion codes which subsequently calculates the resulting ice shape that evolves over a period of time. The grid generator is next invoked to generate a new volume grid around the iced configuration, for use in the CFD solver for an updated flow filed. These modules are coupled to each other using a PYTHON script, and exchange the required data using industry-standard flow filed and grid format (PLOT3D).

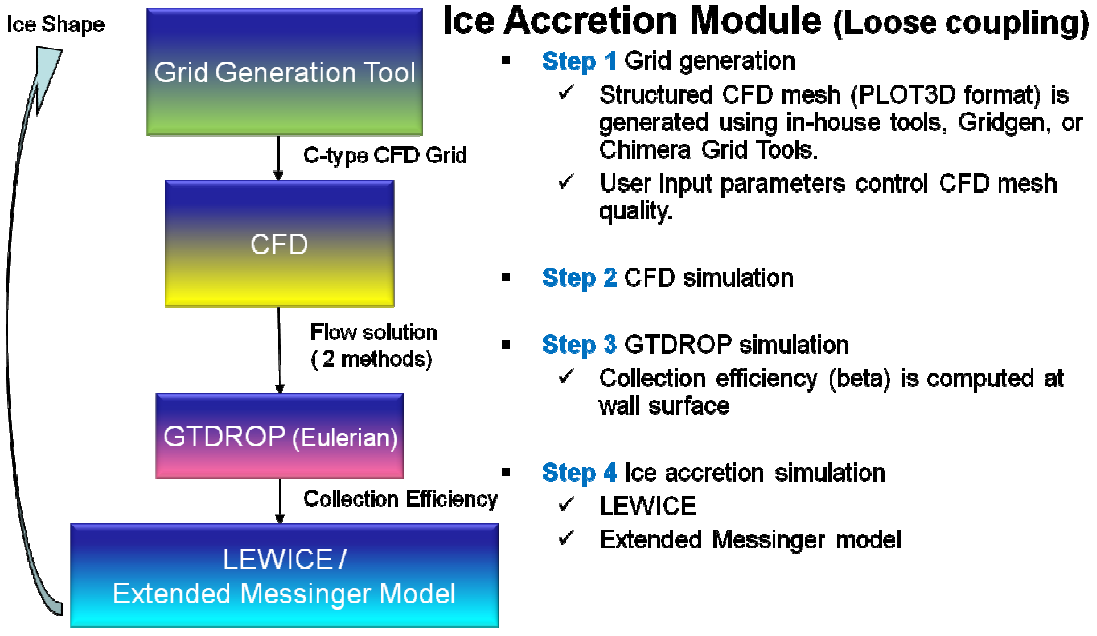

Figure 2.1 Overview of the Ice Accretion Analysis.

2.2 CFD Solver

2.2.1 GENCAS

GENCAS (Generic Numerical Compressible Airflow Solver) [65, 66] is a Navier-Stokes equation solver for generic compressible airflow. 2D or 3D structured multi-block grid can be used. Roe's FDS and AUSMPW+ upwind schemes are available for Euler flux computation. 1^{st} or 2^{nd} order implicit LUSGS with Newton sub-iteration, or $2^{nd}/4^{th}$ order explicit Runge-Kutta schemes are available for time marching. For higher order accuracy, 3^{rd} order MUSCL, 5^{th} order and 7^{th} order WENO cell interface reconstruction methods can be selected as a user input. Various available turbulence models include one equation Spalart-Allmaras (SA) and SA-DES models, and two equation Wilcox's κ-ω, standard κ-ε, Menter's κ-ω/κ-ε BSL, Menter's κ-ω SST (DES), KES, and HRKES models.

A hybrid Navier-Stokes/Free wake method is also available as a user option. In this method, vicinity of a blade is modeled by Navier-Stokes equation while far-field wake is modeled by free wake. This enables user to make grid much easier and to get solution faster. For a detailed description of the numerical formulation of GENCAS, the reader is referred to the papers written by Min et al [65, 66].

GENCAS provides flow field data as a Tecplot or plot3d format, forces and moments corresponding to vectors defined by user, wake geometry at every certain time steps, and sectional normal force and moments as a function of time. Hub forces, moments, thrust, power and torque are provided as a function of time as well (Tecplot format).

2.2.2 GT-Hybrid

GT-Hybrid [67,68] is a finite volume based three-dimensional unsteady viscous compressible flow solver. The flow is modeled by first principles using the Navier-Stokes Methodology. The Navier-Stokes equations are solved in the transformed body-fitted coordinate system using a time-accurate, finite volume scheme. A third-order spatially accurate Roe scheme is used for computing the inviscid fluxes and second order central differencing scheme is used for viscous terms. The Navier-Stokes equations are integrated in time by means of an approximate LU-SGS implicit time marching scheme. The flow is assumed to be turbulent everywhere, and hence no transition model is currently used. The solver accepts a user defined table of blade geometric and elastic deformations and deforms the computational grid. The temporal change in computational cell volume is accounted for, by explicitly satisfying the Geometric Conservation Law (GCL). The near wake region is captured inherently in the Navier-Stokes analysis.

The influence of the other blades and of the trailing vorticity in the far field wake are accounted for, by modeling them as a collection of piece-wise linear bound and trailing vortex elements. The use of such a hybrid Navier-Stokes/vortex modeling method allows for an accurate and economical modeling of viscous features near the blades, and an accurate "non-diffusive" modeling of the trailing wake in the far field.

The vortex model is based on a Lagrangian wake approach where a collection of vortex elements are shed from the rotor blade trailing edge and are convected downstream. The strength of the vortex elements is based on the radial gradient of bound circulation and the number of wake trailers chosen by the user. In case of a single trailer coming off the blade tip, the vortex strength is assumed to be peak bound circulation at the instance the vortex segment is generated. The vortices are propagated in time at a local velocity, calculated as the induced velocity due to all vortex filaments plus the free-stream velocity. The induced velocities due to the free wake structure are also calculated

at the N-S computational domain outer surface and are applied as inflow boundary condition. This allows the vortices to reenter the computational domain.

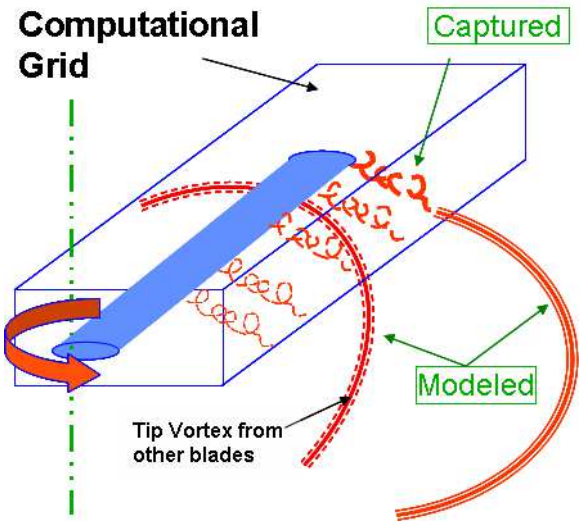

Figure 2.2: A Schematic View of the Hybrid Method.

Figure 2.2 shows a schematic of the Hybrid method employed in GT-Hybrid, depicting the Navier-Stokes domain around the blade-region, the wake captured inside the near-blade Navier-Stokes domain and part of the wake which is modeled as a Lagrangian free wake.

The influence of the trailed vortices from the wake model on the blade aerodynamics is computed by appropriately specifying the vortex-induced velocities at the far field boundary of the Navier-Stokes domain, neglecting the contribution of the elements within the CFD volume grid trailed immediately from the blade.

GT-Hybrid currently has the capability to use advanced turbulence models such as SA-DES and KES to compute the eddy viscosity. Although various turbulence models are available in the GT-Hybrid solver, SA-DES model was mainly used for rotor application for computational efficiency and its ability to accurately predict massively separated flows encountered in maneuvering flight characterized by dynamic stall cycles.

2.3 Droplet Solver

In order to compute the droplet flowfield properties at the same nodes of the discrete domain where the flow variables of air are known, an Eulerian approach is used in the present study. In this method, the average water droplet properties within a control volume are solved instead of tracking individual particles. This physical approach has several advantages over the Lagrangian approach. These include improved quality of the solution, the ability to model unsteady flows over bodies in relative motion, and the automated treatment of shadow zones (no impingement) for probes or detector placing [27]. The interaction between the air particles and the droplets occurs through a drag force exerted by the mean flow on the particles. The presence of the droplet flow field is not felt by the mean flowfield solver, and the droplets are treated as a passive scalar field. When the air flow is steady, the CFD analysis may be computed a priori and used in the droplet solver.

Table 2.1: Comparison between Lagrangian Method and Eunerian Approach for the Prediction of Droplet Trajectory

Approach	Characteristics
Lagrangian	- LEWICE or LEWICE3D (representative examples of industry-standard icing programs) - Computing droplet trajectories through the air - Problems for the separated flow and shadow zone - Not suited for dynamic analysis typical to rotorcraft because the locations where droplets are released need to be specified
Eulerian	- FENSAP-ICE (representative solver) - Two additional governing equations for the volume fraction of water and the particle velocities are solved simultaneously with the flow field solutions. - These equations are solved on the same CFD mesh. - The flowfield may be unsteady, and the solid surfaces may be in relative motion. Most Lagrangian approaches, on the other hand, assume or require the flow field to be steady. - Eulerian method is more attractive for modeling of rotorcraft icing phenomena

In the derivation of governing equations for air-droplet flows, the following assumptions are made [24]:

- The droplets have a spherical shape and do not undergo any deformation or breaking.
- There is no collision, or coalescence between droplets.
- There is no exchange of heat and mass between the droplets and the surrounding air.
- The effect of mean flow mixing effects on the droplet is neglected.
- Drag, gravity and buoyancy due to density differences are the only forces acting on the droplets.

The first two assumptions are based on the fact that the size of icing droplets is 1-100 μm range and droplet flow is considered dilute with a volume fraction around 10^{-6}. Although the gravity and buoyancy forces are three orders lower in magnitude than drag force in typical flight conditions, these forces are kept in the model because their effects could be significant in the simulation of de-icing fluid contamination by rain and snow during ground operation.

Governing Equations

In in-flight icing conditions, air and water droplets are mixed on length scales smaller than the one which we want to resolve. The phases can be treated as continuous fluids and all phases coexist throughout the flow domain. The portion of volume occupied by water droplets is given by the volume fraction. Conservation equations for mass and momentum can be solved for each phase. A PDE form of the governing equations for the conservation of mass and momentum of the droplets in Cartesian coordinate system are written as follows:

$$\frac{\partial Q}{\partial t} + \frac{\partial E_j}{\partial x_j} = H \tag{2.1}$$

where Q is the droplet variable vector, E_j is the droplet flux vector, and H is the source vector.

$$Q = \begin{bmatrix} \alpha \\ u_i \end{bmatrix} \tag{2.2}$$

$$\mathrm{E_j} = \begin{bmatrix} \alpha u_j \\ u_i u_j \end{bmatrix} \tag{2.3}$$

$$\mathrm{H} = \begin{bmatrix} 0 \\ \frac{C_D Re_d}{24K}(u_a - u_i) + \left(1 - \frac{\rho_a}{\rho}\right)\frac{1}{Fr^2} g_i \end{bmatrix} \tag{2.4}$$

Here, α is defined as the non-dimensionalized volume fraction of water; u_i, the non-dimensionalized velocity of droplets; u_a, non-dimensionalized velocity of air; ρ, the density of water; ρ_a, the density of air; g_i, gravity vector; $F_r = U_\infty / \sqrt{Lg}$ is the Froude number; U_∞, the speed of air at freestream; L, the characteristic length (typically the airfoil chord length); $K = \rho d^2 U_\infty / 18 L\mu$, an inertia parameter; μ, the dynamic viscosity of air.

The first term on the right-hand-side of the momentum equation accounts for the drag acting on the droplet or particle based on low-Reynolds number, or Stokes flow, behavior for spheres [69]. The droplets Reynolds number ($\mathrm{Re_d}$) is defined based on the slip velocity between the air and droplet and the droplet diameter. The drag coefficient is

$$\begin{aligned} C_D &= \frac{24}{Re_d}(1 + 0.15 Re_d^{0.678}) \qquad && Re_d \leq 1000 \\ C_D &= 0.4 && Re_d > 1000 \end{aligned} \tag{2.5}$$

with,

$$Re_d = \frac{\rho_a d U_\infty |u_a - u_i|}{\mu}$$

The governing equations in the Cartesian coordinate system $(\mathrm{t}, \mathrm{x}, \mathrm{y}, \mathrm{z})$ are transformed to a curvilinear coordinate system $(\mathrm{t}, \xi, \eta, \zeta)$ using the link between them.

$$\xi = \xi(x, y, z, t)$$

$$\eta = \eta(x, y, z, t) \tag{2.6}$$

$$\zeta = \zeta(x, y, z, t)$$

After the transformation procedure, the governing equation, Eqn. (2.1), is re-written in the curvilinear coordinate system as Eqn. ((2.7).

$$\frac{\partial \bar{Q}}{\partial t} + U\frac{\partial \bar{Q}}{\partial \xi} + V\frac{\partial \bar{Q}}{\partial \eta} + W\frac{\partial \bar{Q}}{\partial \zeta} = H \tag{2.7}$$

$$\bar{Q} = \frac{1}{J}\begin{Bmatrix} \alpha \\ u \\ v \\ w \end{Bmatrix} \tag{2.8}$$

where J is the Jacobian of the transformation, and U, V, W are the contravariant velocity components along the ξ, η, and ζ coordinate direction.

$$U = \xi_t + \xi_x u + \xi_y v + \xi_z w$$

$$V = \eta_t + \eta_x u + \eta_y v + \eta_z w \tag{2.9}$$

$$W = \zeta_t + \zeta_x u + \zeta_y v + \zeta_z w$$

The metrics are defined as:

$$\xi_t = -x_t\xi_x - y_t\xi_y - z_t\xi_z$$

$$\eta_t = -x_t\eta_x - y_t\eta_y - z_t\eta_z \tag{2.10}$$

$$\zeta_t = -x_t\zeta_x - y_t\zeta_y - z_t\zeta_z$$

$$\xi_x = J(y_\eta z_\zeta - y_\zeta z_\eta);\ \xi_y = J(x_\zeta z_\eta - x_\eta z_\zeta);\ \xi_z = J(x_\eta y_\zeta - x_\zeta y_\eta)$$

$$\eta_x = J(y_\zeta z_\xi - y_\xi z_\zeta);\ \eta_y = J(x_\xi z_\zeta - x_\zeta z_\xi);\ \eta_z = J(x_\zeta y_\xi - x_\xi y_\zeta)$$

$$\zeta_x = J(y_\xi z_\eta - y_\eta z_\xi);\ \zeta_y = J(x_\eta z_\xi - x_\xi z_\eta);\ \zeta_z = J(x_\xi y_\eta - x_\eta y_\xi)$$

And the Jacobian of the coordinate transformation is defined as follows:

$$J = \frac{\partial(\xi, \eta, \zeta, t)}{\partial(x, y, z, t)} = \frac{1}{x_\xi(y_\eta z_\zeta - y_\zeta z_\eta) - x_\eta(y_\xi z_\zeta - y_\zeta z_\xi) + x_\zeta(y_\xi z_\eta - y_\eta z_\xi)}$$

Discretization

A first order upwind scheme is employed for computing the mass and momentum flux at the faces of the control volume. The convection velocities are defined such that only one will have a value dependent on the direction of the flow.

$$U^+ = \frac{(U + |U|)}{2}$$
$$U^- = \frac{(U - |U|)}{2} \qquad (2.11)$$

Subsequently,

$$U\frac{\partial \mathrm{u}}{\partial \xi} = U^+(\mathrm{u_i} - \mathrm{u_{i-1}}) + U^-(\mathrm{u_{i+1}} - \mathrm{u_i}) \qquad (2.12)$$
$$= -U^+ u_{i-1} + (U^+ - U^-)u_i + U^- u_{i+1}$$

Time Marching

In an implicit formulation with first order backward differencing in time and using the central difference operator, δ, the governing equations can be written as the matrix form:

$$\left[I + \Delta t\left(U\delta_\xi + V\delta_\eta + W\delta_\zeta\right)\right]\Delta Q^{n+1} = (RHS)^n \tag{2.13}$$

$$(RHS)^n = -\Delta t\left(U\delta_\xi + V\delta_\eta + W\delta_\zeta\right)Q^n + H \tag{2.14}$$

Equation (2.13) is a matrix system, which is computationally very expensive to invert. In this study, the matrix inside the bracket on the left-hand side is approximately factored using a Lower-Upper Symmetric Gauss-Seidel (LU-SGS) implicit method. The matrix is the sum L+D+U, where each of the element matrices L, D, and U are readily invertible. Equation (2.13) is expressed as:

$$(L + D + U)\Delta Q^{n+1} = (RHS)^n \tag{2.15}$$

Where L is a lower block triangular matrix with null matrices on the diagonal, D is a block diagonal matrix and U is an upper block triangular matrix with null matrices on the diagonal. For the case of non-singular matrix D, Eqn. (2.15) is re-written as:

$$D(D^{-1}L + I + D^{-1}U)\Delta Q^{n+1} = (RHS)^n \tag{2.16}$$

Using LU-factorization, Eqn. (2.16) may be approximated as:

$$D(I + D^{-1}L)(I + D^{-1}U)\Delta Q^{n+1} = (RHS)^n \tag{2.17}$$

Or

$$(D + L)D^{-1}(D + U)\Delta Q^{n+1} = (RHS)^n \tag{2.18}$$

where:

$$(D + L) = -\Delta t(U^+ + V^+ + W^+)$$

$$D = I + \Delta t[(U^+ - U^-) + (V^+ - VB^-) + (W^+ - W^-)] \tag{2.19}$$

$$(D + U) = \Delta t(U^- + V^- + W^-)$$

The set of matrices can be solved in the process such that:

$$(D + L)X = (RHS)^n$$

$$D^{-1}Y = X \tag{2.20}$$

$$(D + U)\Delta Q^{n+1} = Y$$

The matrices on the left-hand side of Eqn. (2.20) have either lower, diagonal, or upper part only with all others zero. Thus, inversion of each matrix is easily accomplished by backward or forward substitution. Once ΔQ^{n+1} is obtained, the new Q^{n+1} is computed from $Q^{n+1} = Q^n + \Delta Q^{n+1}$. Mean flow quantities are lagged by one time step compared to particle velocity and volume fraction.

Boundary Conditions

The freestream values of droplet velocity and volume fraction are imposed as boundary conditions at the far field. Prescribing the correct boundary conditions for the droplets at the wall is not straight-forward. The droplet velocity cannot be simply set to zero on the walls. A switching boundary condition [26] is applied. Volume fraction and velocity of droplets are extrapolated from the computed flux entering the control volumes adjacent to the solid. A lower bound of volume fraction and zero velocity are imposed on flux exiting the flowfield, and collecting on the walls.

$$\begin{aligned} &\alpha_w = \alpha_{w-1} \; and \; u_{i,w} = u_{i,w-1} \qquad Incoming \; droplet \; fluxes \\ &\alpha_w = f_\alpha \; and \; u_{i,w} = 0 \qquad Droplet \; fluxe \; exiting \; the \; wall \end{aligned} \tag{2.21}$$

A common way of comparing droplet impingement rate at various flight conditions is through the collection efficiency(β). This quantity characterizes the configuration's ability to capture incoming water and is defined as the local mass flux of water onto the airfoil surface normalized by the freestream liquid water content and the freestream velocity.

$$\beta = \frac{\alpha \rho_w u_i}{(LWC) U_\infty} \frac{A_i}{|A|} \tag{2.22}$$

where, A_i is the local area normal; LWC, Liquid water content (Fig. 2.3).

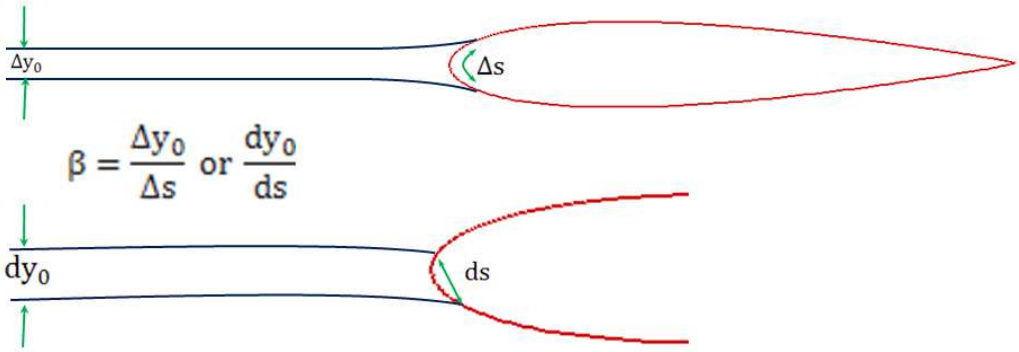

Figure 2.3: Definition of Collection Efficiency.

Computational prediction for large droplet case and found to show a considerably higher collection efficiency distribution and the peak value is greater than the measurement [70]. A plausible reason for this over prediction is droplet splashing and breakup [70]. The effect of droplet splashing is considered by using a model proposed in Ref. 23. Splashing causes a reduction in collection efficiency. The mass faction of water lost due to bouncing (N_b) is first computed.

$$N_b = 0.2\left[1 - exp\left(-0.85\left(\sqrt{K_{tn}}\right)\right)\right] \tag{2.23}$$

where

$$K_{tn} = 0.859\left(\frac{\rho_w}{LWC}\right)^{0.125}\sqrt{K} \tag{2.24}$$

$$K = \frac{\mu_w}{\rho_w \sigma d}\left(\frac{\rho_w |u_a - u_i| d}{\mu_w}\right)^{1.25} \tag{2.25}$$

Here, σ is surface tension between air and water. Finally the collection efficiency is computed as:

$$\beta' = \beta(1 - N_b) \tag{2.26}$$

2.4 Ice Accretion Solver

2.4.1 LEWICE

LEWICE [23] ,developed by the NASA Glenn Research Center, has been used by literally hundreds of users in the aeronautics community for predicting ice shapes, collections efficiencies, and anti-icing heat requirements. LEWICE consists of four major modules. The first module is flowfield calculation using a panel method, developed by Hess and Smith [71]. The second module is particle trajectory and impingement calculation using a Lagrangian approach by Frost et al [72]. Thermodynamic and ice growth calculation is third module. An integral boundary layer method is used to determine the skin friction and local convective heat transfer coefficient. Finally, Messinger model [5] is for ice accretion thermodynamic analysis. LEWICE also has capability for de-icing and anti-icing analysis.

2.4.2 Extended Messinger Model

Calculation of Convective Heat Transfer Coefficients

One of important factors in the ice accretion process is convective heat transfer coefficients. In the present study, an Integral Boundary Layer Method is used to predict the heat transfer coefficients. This method gives fairly accurate laminar and turbulent boundary layer properties. The transition from laminar to turbulent flow is predicted based on the roughness Reynolds number. The roughness Reynolds number is defined as:

$$Re_k = \frac{\rho U_k k_s}{\mu} \tag{2.27}$$

where k_s is the roughness height and U_k is the local velocity at the roughness height from the following expression [64]:

$$\frac{U_k}{U_e} = 2\frac{k_s}{\delta} - 2\left(\frac{k_s}{\delta}\right)^3 + \left(\frac{k_s}{\delta}\right)^4 + \frac{1}{6}\frac{\delta^2}{\nu_a}\frac{dU_e}{ds}\frac{k_s}{\delta}\left(1 - \frac{k_s}{\delta}\right)^3 \tag{2.28}$$

where U_e is the velocity outside the boundary layer at the roughness location and s is the surface wrap distance from stagnation point. The roughness height is calculated by [73]:

$$k_s = \left(\frac{4\sigma_w \mu_w}{\rho_w F \tau}\right)^{\frac{1}{3}} \tag{2.29}$$

where σ_w , ρ_w and μ_w are the surface tension, density and viscosity of water. F is the fraction of the airfoil surface which is wetted by water droplets. τ is the local surface shear stress. The boundary layer thickness (δ) is calculated by [74]:

$$\delta = \frac{315}{37}\theta \tag{2.30}$$

where θ is the laminar momentum thickness. The current study employs Thwaites' method [75] to calculate laminar momentum thickness. Thwaites' method is a combined method of analysis and experiments. The accuracy of this method is within 3% or so for favorable pressure gradients, and 10% for adverse pressure gradients but perhaps slightly worse near boundary-layer separation. In Thwaites' method, the laminar momentum thickness is calculated by:

$$\frac{\theta^2}{\nu} = \frac{0.45}{U_e^6}\int_0^s U_e^5 \, ds \tag{2.31}$$

Transition location is determined by Von Doenhoff criterion (Re_k =600). For laminar flow ($Re_k \leq 600$), the laminar heat transfer coefficient is calculated by [23]:

$$h = \frac{2\mathrm{k}}{\delta_\mathrm{T}} \tag{2.32}$$

where k is thermal conductivity of air, δ_T is thermal boundary thickness as given by the equations [23]:

$$\left(\frac{\delta_T}{c}\right)^2 \frac{U_\infty c}{\nu} = \frac{46.72}{\left(\frac{U}{U_\infty}\right)^{2.87}} \int_0^{\frac{s}{c}} \left(\frac{U}{U_\infty}\right)^{1.87} d\left(\frac{s}{c}\right) \tag{2.33}$$

where c is reference chord length, U is velocity at a given surface location, ν is kinematic viscosity of air, U_∞ is freestream velocity.

For turbulent flow ($Re_k > 600$), the method of Kays and Crawford [76] is used to calculate turbulent heat transfer coefficient. The turbulent convective heat transfer coefficient is obtained from:

$$h = \mathrm{St}\, \rho\, U_e C_p \tag{2.34}$$

where C_p is the specific heat of air. The Stanton number (St) is calculated from:

$$\mathrm{St} = \frac{\frac{C_f}{2}}{\mathrm{Pr_t} + \sqrt{\frac{C_f}{2}\frac{1}{\mathrm{St_k}}}} \tag{2.35}$$

where Pr_t is turbulent Prandtl number. The roughness Stanton number ($\mathrm{St_k}$) is calculated from:

$$\mathrm{St_k} = 1.92\, \mathrm{Re_k^{-0.45}}\, \mathrm{Pr^{-0.8}} \tag{2.36}$$

where Pr is laminar Prandtl number. In this study, skin friction coefficient from CFD simulation is used instead of using empirical skin friction equation.

The boundary-layer analysis begins from the stagnation point and proceed downstream using the marching technique for the upper and lower surfaces of the airfoil. The transition location is fixed at the streamwise location where $\mathrm{Re_k}$ =600.

Problem Formulation

Figure 2.4 shows typical ice accretion situation. An ice layer (B(t)) stays on the top of a solid substrate. In case of glaze ice, a water layer (h(t)) will cover the ice layer. The temperature of each layer is denoted by $T(z,t)$ and $\theta(z,t)$, respectively.

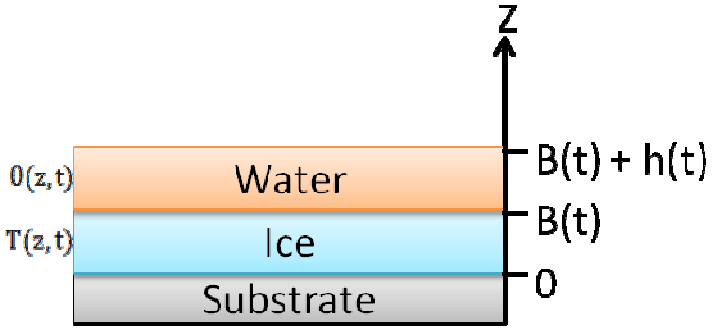

Figure 2.4: Schematic of the Ice and Water System.

The Stefan problem is governed by four equations: heat equations in the ice and water, a mass balance, and a phase change or Stefan condition at the ice/water interface:

$$\frac{\partial T}{\partial t} = \frac{k_i}{\rho_i C_{pi}} \frac{\partial^2 T}{\partial z^2} \tag{2.37}$$

$$\frac{\partial \theta}{\partial t} = \frac{k_w}{\rho_w C_{pw}} \frac{\partial^2 \theta}{\partial z^2} \tag{2.38}$$

$$\rho_i \frac{\partial B}{\partial t} + \rho_w \frac{\partial h}{\partial t} = (LWC)\beta V_\infty + \dot{m}_{in} - \dot{m}_{e,s} \tag{2.39}$$

$$\rho_i L_F \frac{\partial B}{\partial t} = k_i \frac{\partial T}{\partial z} - k_w \frac{\partial \theta}{\partial z} \tag{2.40}$$

where k_i and k_w are thermal conductivity of ice and water. C_{pi} and C_{pw} are specific heat of ice and water. B and h are the thicknesses of ice and water layers. In Eq. (2.39), the quantities, $(LWC)\beta V_\infty$, $\dot{m}_{in}$ and $\dot{m}_{e,s}$ are the impinging, runback and evaporating (or sublimating) water mass flow rates for a control volume respectively. In Eq. (2.40), ρ_i

and L_F are density of ice and latent heat of solidification of water. The ice density, ρ_i , in Eq. (2.39) and (2.40) can take different values depending on whether rime or glaze ice forms. In the current work, only two different values, ρ_r and ρ_g are used.

Initial and Boundary Conditions

Extended Messinger Model [39,64] is based on the standard method of phase change or the Stefan condition [37], similar to the Messinger [5] energy balance in the form of a differential equation. The difference with the original Messinger model is that extended Messinger model requires knowledge of the temperature gradients in each layer. Hence the heat equations in the ice and water layer are analytically solved. To solve the Stefan problem boundary and initial conditions are specified from the following assumptions:

1. Ice is in perfect thermal contact with the airfoil surface, which has high conductivity and a thermal mass much greater than that of the ice accretion:

$$T(0,t) = T_S \tag{2.41}$$

2. The temperature is continuous at the ice and water interface and is set to the freezing temperature:

$$T(B,t) = \theta(B,t) = T_S \tag{2.42}$$

3. A standard radiation boundary condition with an added heat flux is applied at the air and water interface [77]. It states that the heat flux at the surface is determined by convection (Q_c), radiation (Q_r), latent heat release (Q_l), cooling by incoming droplets (Q_d), heat brought in by runback water (Q_{in}), evaporation (Q_e) or sublimation (Q_s), aerodynamic heating (Q_a) and kinetic energy of incoming droplets (Q_k) (see Appendix A):

$$\text{Glaze ice}: \quad -k_w \frac{\partial \theta}{\partial z} = (Q_c + Q_e + Q_d + Q_r) - (Q_a + Q_k + Q_{in}) \quad \text{at z = B + h} \tag{2.43}$$

Rime ice : $-k_i \frac{\partial T}{\partial z} = (Q_c + Q_s + Q_d + Q_r) - (Q_a + Q_k + Q_{in} + Q_l)$ at z = B + h (2.44)

4. Airfoil surface is initially clean:

$$B = h = 0, t=0 \quad (2.45)$$

5. The physical properties of the ice and water do not vary with temperature. However, the ice density is allowed to take two distinct values, depending on whether rime or glaze ice forms. It is assumed that the transition between them occurs instantaneously.
6. The phase change occurs at a single freezing temperature (273.15 K).

These conditions are sufficient to calculate the temperature distribution and thicknesses of ice and water layers. Note that all terms of the original Messinger model have now appeared, either in the Stefan or in the boundary conditions.

Ice Growth : Rime Ice

Ice growth for rime ice is trivial. The thickness of rime ice can be calculated from the mass balance, Eq. (2.39), with h set to zero:

$$B = \left(\frac{(LWC)\beta V_\infty + \dot{m}_{in} - \dot{m}_s}{\rho_r} \right) t \quad (2.46)$$

Eq. (2.37) can be converted from a PDE into ODE by taking only the leading order term [39]. This produces what is termed the quasi-steady problem since time only appears through the moving boundary conditions. This physically means that the timescale for ice growth is much smaller than that for conduction through the ice. The leading-order problem is then expressed as:

$$\frac{\partial^2 T}{\partial z^2} = 0 \quad (2.47)$$

When the ice thickness is less than 2.4 cm, the series solution of Eq. (2.47) will be valid [39]. The temperature distribution inside the rime ice layer can be obtained by integrating Eq. (2.47) twice and applying Eq. (2.41) and Eq.(2.44).

$$T(z) = T_s + \frac{(Q_a + Q_k + Q_{in} + Q_l) - (Q_c + Q_s + Q_d + Q_r)}{k_i} z \tag{2.48}$$

Ice Growth : Glaze Ice

With a same approach (leading-order problem) for rime ice case, the heat equations can be simplified to quasi-steady forms:

$$\frac{\partial^2 T}{\partial z^2} = 0, \qquad \frac{\partial^2 \theta}{\partial z^2} = 0 \tag{2.49}$$

If ice and water layer thicknesses are less than 2.4 cm and 3 mm (which is the case for most aircraft icing condition) [39], after integrating Eq. (2.49) twice and employing the conditions (2.41) and (2.42), the temperature in the ice is:

$$T(z) = T_s + \frac{T_f - T_s}{B} z \tag{2.50}$$

The temperature distribution in the water becomes;

$$\theta(z) = T_f + \frac{(Q_a + Q_k + Q_{in}) - (Q_c + Q_e + Q_d + Q_r)}{k_w} (z - B) \tag{2.51}$$

Unlike rime ice case, the calculation of glaze ice thickness requires knowledge of the temperature profile. The problem is coupled; the temperatures given by Eq. (2.50) and (2.51) are function of the ice and water heights, which in turn depend on the temperature through Eq. (2.40).

In order to solve the coupled problem, integration of the mass conservation equation, Eq. (2.39) is done. This yields an expression for the water height, *h*, as a function of *B* and *t*:

$$h = \left(\frac{(LWC)\beta V_\infty + \dot{m}_{in} - \dot{m}_e}{\rho_w}\right)(t - t_g) - \frac{\rho_g}{\rho_w}(B - B_g) \tag{2.52}$$

where B_g is the ice thickness at which glaze ice first appears and t_g is the time at which this happens.

The next step is differentiating Eq. (2.50) and (2.51) to get the temperature gradients. When these temperature gradients with Eq. (2.52) are substituted into the phase

change condition in Eq. (2.40), a first order nonlinear ordinary differential equation for the ice thickness is obtained:

$$\rho_g L_F \frac{\partial B}{\partial t} = \frac{k_i(T_f - T_s)}{B} + k_w \frac{(Q_c + Q_e + Q_d + Q_r) - (Q_a + Q_k + Q_{in})}{k_w + (Q_c + Q_e + Q_d + Q_r)} \quad (2.53)$$

In order to calculate ice thickness for the glaze ice, Eq. (2.53) is integrated numerically, using a following 4th order Runge-Kutta method.

The Eq. (2.53) may be expressed as a simplified form:

$$\begin{cases} B' = f(t, B) \\ B(t_0) = B_0 \end{cases}$$

Then the following formula:

$$\begin{aligned} w_0 &= B_0 \\ k_1 &= \Delta t\, f(t_i, w_i) \\ k_2 &= \Delta t\, f\left(t_i + \frac{\Delta t}{2}, w_i + \frac{k_1}{2}\right) \\ k_3 &= \Delta t\, f\left(t_i + \frac{\Delta t}{2}, w_i + \frac{k_2}{2}\right) \\ k_4 &= \Delta t\, f(t_i + \Delta t, w_i + k_3) \\ w_{i+1} &= w_i + \frac{1}{6}(k_1 + 2k_2 + 2k_3 + k_4) \end{aligned}$$

computes an approximate solution, that is $w_i \approx B(t_i)$.

During the ice accretion, thicknesses of ice and water layer and growth rate have to be continuous for a smooth transition from the rime ice to glaze ice. To calculate when this transition occurs, the ice growth rate from Eq. (2.39) is substituted into the phase change condition (Eq. (2.40)) to give:

$$B_g = \frac{k_i(T_f - T_s)}{L_F((LWC)\beta V_\infty + \dot{m}_{in} - \dot{m}_{sub}) + (Q_a + Q_k + Q_{in}) - (Q_c + Q_e + Q_d + Q_r)} \quad (2.54)$$

The time when the glaze ice first appear is calculated by comparison with Eq. (2.46):

$$t_g = \left(\frac{\rho_r}{(LWC)\beta V_\infty + \dot{m}_{in} - \dot{m}_{sub}}\right) B_g \quad (2.55)$$

Eq. (2.55) shows how the ice thickness at which glaze ice will first appear depends on the ambient conditions. It is found that it allows positive, negative, and even infinite values for B_g. These may be interpreted as:

- $0 < B_g < \infty$: Eq. (2.54) indicates the ice thickness when glaze ice first appears. Consequently, Eq. (2.55) shows the time at which this happens.
- An infinite or $0 > B_g$: This indicates the glaze ice will not appear. There are mainly two reasons for this.
  - ✓ Numerator ($T_f - T_s < 0$) : This means that the substrate is too warm for ice to grow.
  - ✓ The denominator of Eq. (2.54) is less than zero indicating that there is insufficient energy in the system to produce liquid water and pure rime ice is produced.

Freezing fractions and runback water

The freezing fraction for a given control volume is defined as the ratio of the amount of water which solidifies to the amount of water that impinges on the control volume plus the water entering the panel as runback water.

$$Rime\ Ice: FF = \frac{\rho_r B}{((LWC)\beta V_\infty + \dot{m}_{in})t} \tag{2.56}$$

$$Glaze\ Ice: FF = \frac{\rho_r B_g + \rho_g (B - B_g)}{((LWC)\beta V_\infty + \dot{m}_{in})t} \tag{2.57}$$

Runback water mass flow rate is:

$$\dot{m}_{out} = (1 - FF)((LWC)\beta V_\infty + \dot{m}_{in}) - \dot{m}_e \tag{2.58}$$

This runback water ($\dot{m}_{out}$) becomes $\dot{m}_{in}$ for the neighboring downstream control volume.

Evaporating or sublimating mass is [64];

$$\dot{m}_{e,s} = \frac{0.7}{C_{pa}} h_c \left(\frac{p_{v,sur} - p_{v,\infty}}{p_\infty} \right) \tag{2.59}$$

where $p_{v,sur}$ and $p_{v,\infty}$ are the vapor pressure at the ice or water surface and the ambient air. These are calculated from [64]:

$$p_v = 3386 \left(0.0039 + 6.8096 \times 10^{-6}\, \overline{T}^2 + 3.5579 \times 10^{-7}\, \overline{T}^3 \right) \tag{2.60}$$

$$\overline{T} = 72 + 1.8(T - 273.15) \tag{2.61}$$

An in-house ice code is developed based on formulations of the Extended Messinger Model. Figure 2.5 shows overall flowchart.

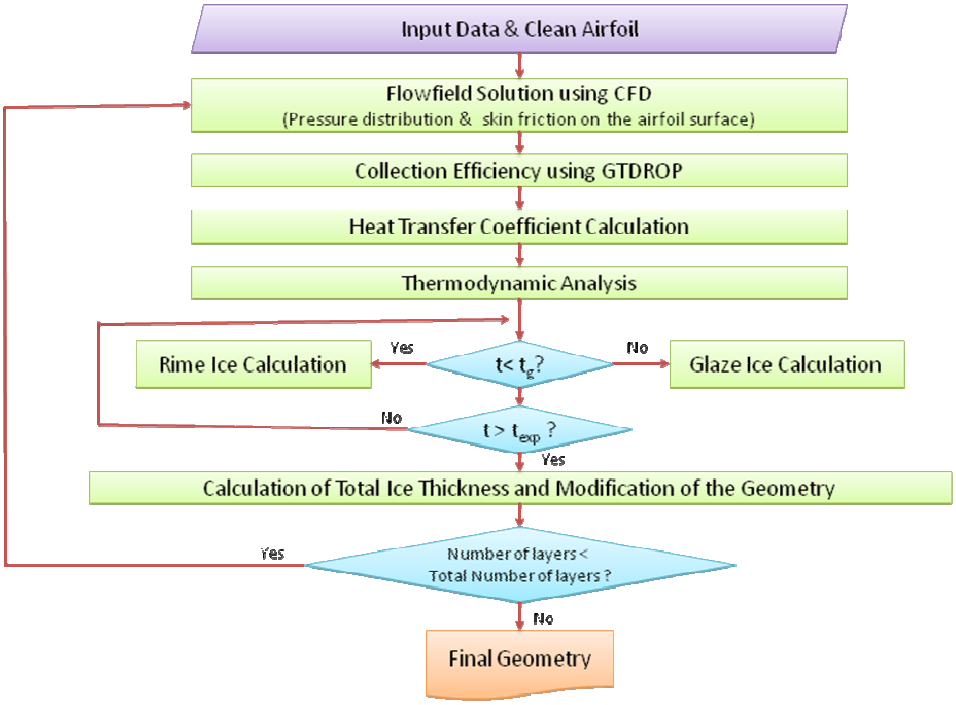

Figure 2.5: Flowchart of the Ice Accretion Code Based on Extended Messinger Model.

CHAPTER 3

VALIDATION AND FEASIBILITY STUDIES

Several numerical simulations have been performed to validate the ability of the codes to capture key flow features related to rotor and ice accretion. The selected cases include 2-D airfoil under attached flows, 2-D airfoil undergoing dynamic stall, 3-D finite wing, and 3-D helicopter rotors. A simulated ice (SimIce) airfoil also has been simulated and compared with wind tunnel test data.

3.1 Validation of CFD Solver

3.1.1 2-D Airfoil Case

2-D steady and unsteady airfoil simulations are done by GENCAS with the clean and simulated iced (SimIce) airfoils. Computational results are compared against experimental data [78] and simulation results from OVERFLOW [79]. All CFD simulations are done for the airspeed of 150 knots; the dynamic conditions have a frequency of 2.8 Hz with a SC2110 airfoil with a modular leading edge that allowed clean and simulated ice measurements to be made. Solutions are computed with resolution to capture the leading-edge suction peak and vortices traveling along the upper surface. Figure 3.1 and 3.2 show O-type 2-D CFD mesh used for simulations. The grid is clustered to capture the boundary layer. For all computations, a fully turbulent boundary layer is assumed. This particular element of the wind tunnel model was inherently rough in contrast to the smooth fiberglass leading edge of the clean airfoil. For solutions presented in this paper, the Roe upwind, third order accurate scheme with the Spalart-Allmaras turbulence model is used. For OVERFLOW simulations, same options are used except transition location for clean airfoil. In the OVERFLOW calculations for clean airfoil a transition to turbulence is enforced at 3% x/c.

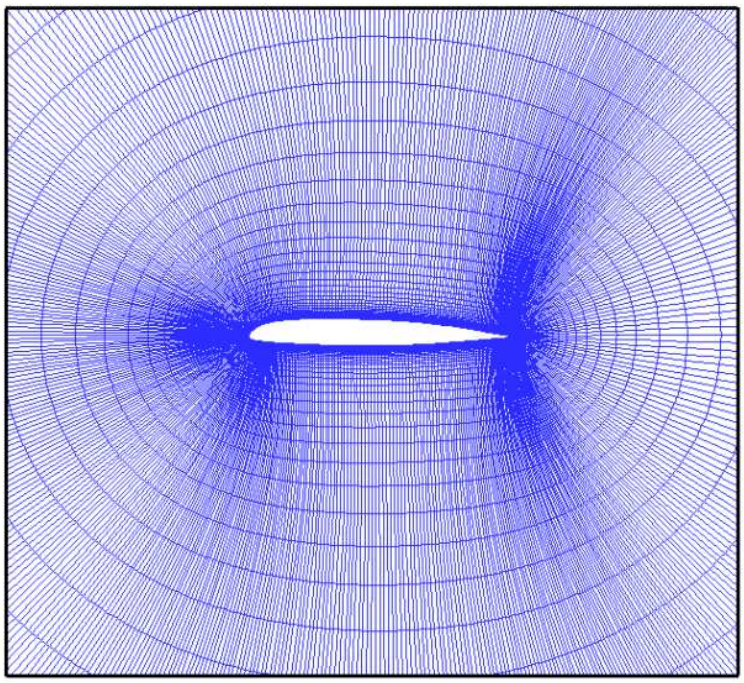

Figure 3.1: 2-D Grid for Clean Airfoil [497 x 65].

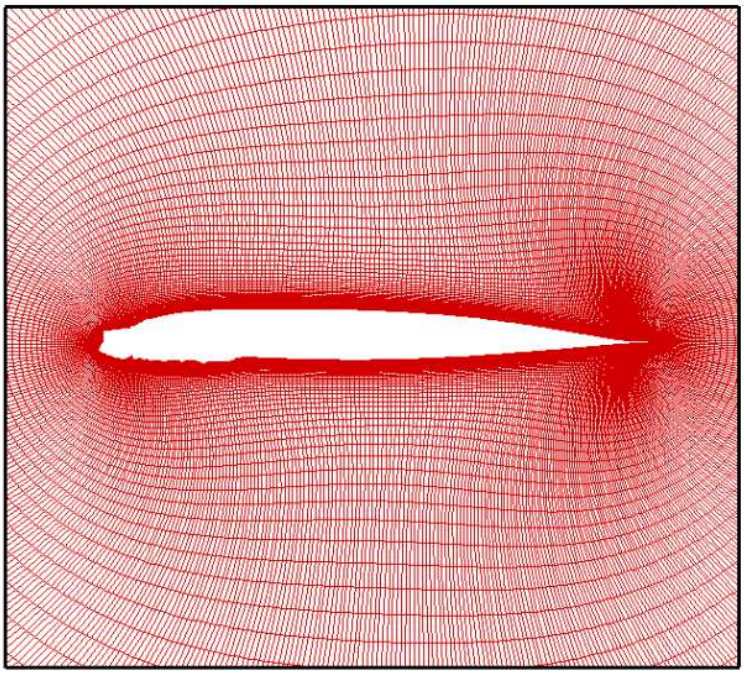

Figure 3.2: 2-D Grid for SimIce Airfoil [553 x 121].

Steady 2-D Airfoil

The static lift performance for the clean airfoil and the SimIce airfoil is shown in Figure 3.3. Below stall the computational results agree well with the experimental measurements; however at high angles of attack the results differ between themselves and the measurements. The experiment suggests a gentle stall of the clean airfoil as indicated by the small change in lift curves slope after 8°. OVERFLOW over-predicts C_{Lmax} and an abrupt stall at 15°. In contrast GENCAS under-predicts C_{Lmax}.

The static lift characteristics for the SimIce shape also proved challenging for 2D CFD. While agreement is very good for attached flow, both codes are under-predicting C_{Lmax}. Despite the complex ice shape, there is closer agreement among analysis and experiment for the SimIce geometry than the clean. The clean airfoil is likely more vulnerable to discrepancies caused by laminar-to-turbulence boundary layer transition because the shape is smoother. The SimIce, being rough, is likely to be fully turbulent. No attempt to predict boundary layer transition was made for either airfoil shape.

The static pitching moment performance for the clean airfoil and SimIce airfoil is shown in Figure 3.4. Both solvers show similar trends with a slightly negative (nose-down) pitching moment for the clean airfoil with varying angle of attack. Both solvers show a similar increasing pitching moment trend with angle of attack until stall for the SimIce.

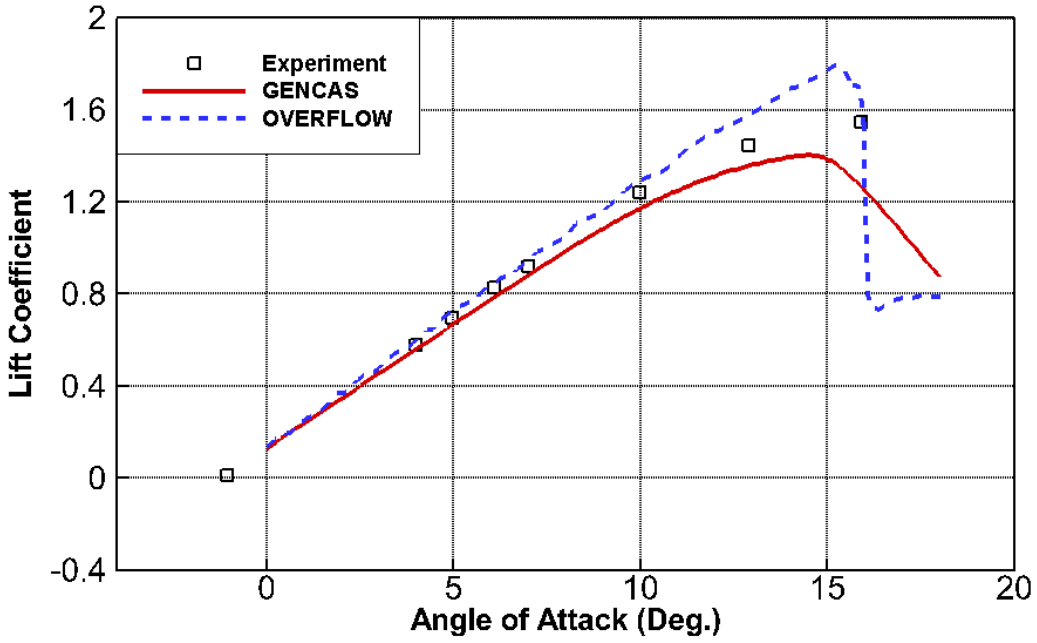

a) Clean Airfoil

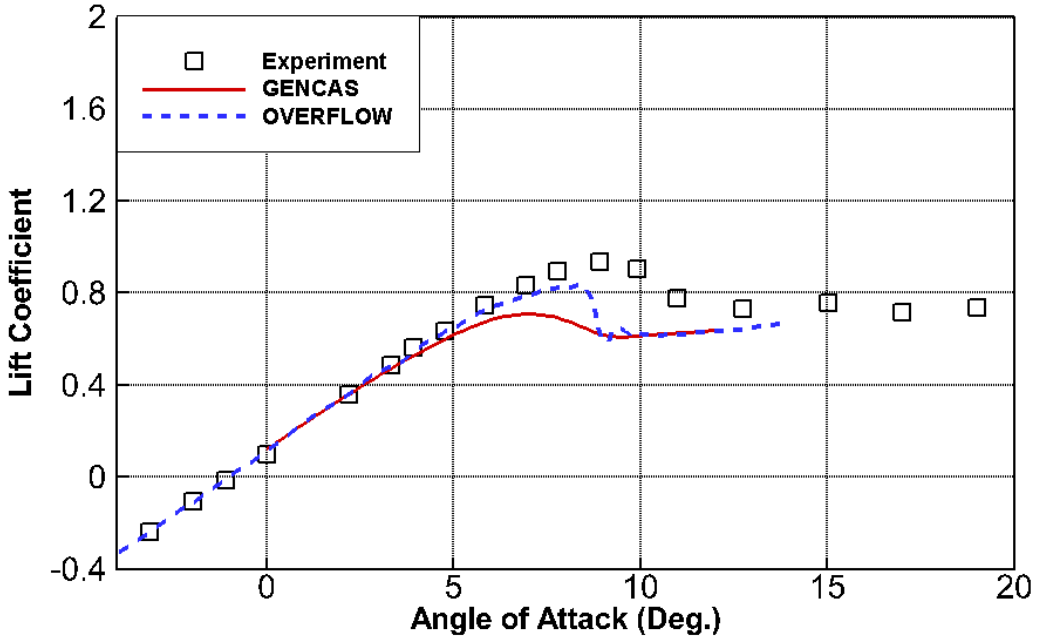

b) SimIce

Figure 3.3: Comparison of Static $C_{l.}$

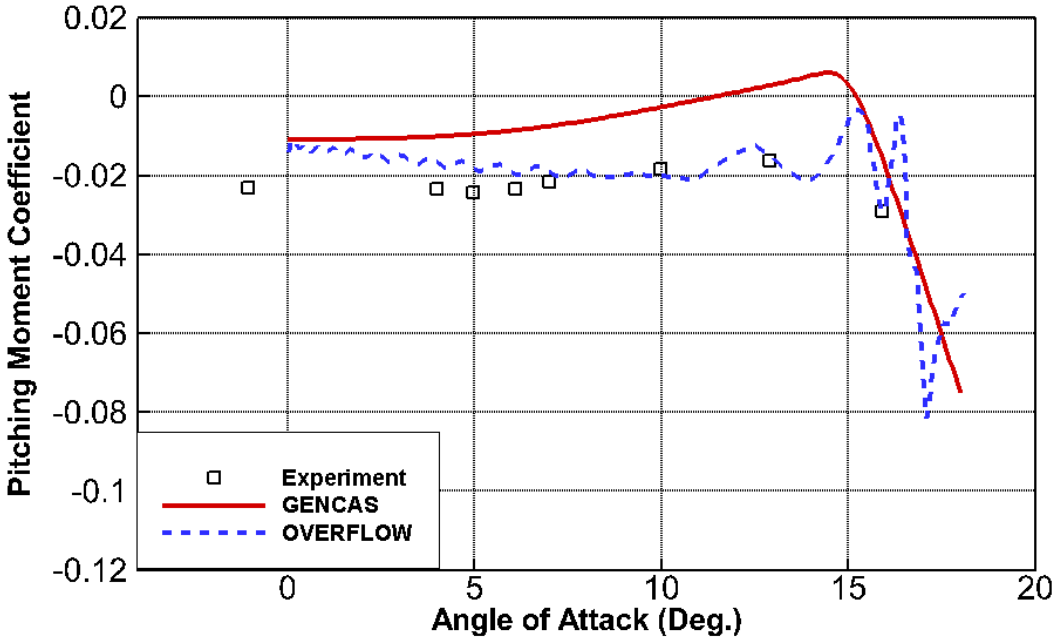

a) Clean Airfoil

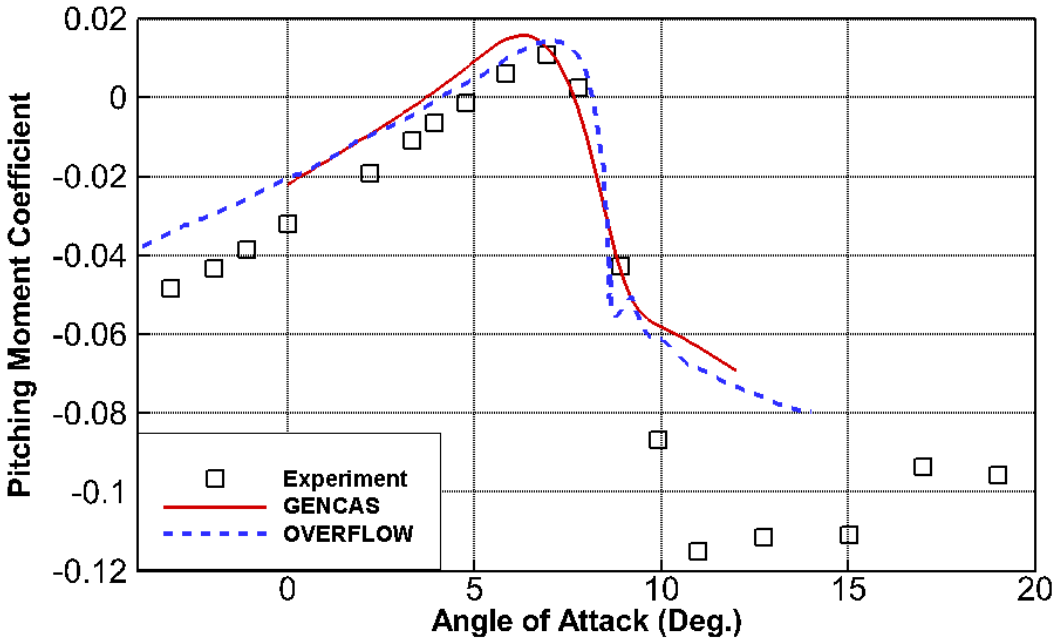

b) SimIce

Figure 3.4: Comparison of Static Cm.

2-D Airfoil undergoing Dynamic stall

Dynamic performance for a clean and SimIce airfoil pitching about the quarter chord ±3 degrees from a mean angle of attack of 5 degrees is presented in Figure 3.5 and Figure 3.6. As indicated in the figures, the clean airfoil does not experience stall and performance is easier to predict. Although the shape of predicted pitching moment hysteresis is similar with experiment, the negative pitching moment is slightly less when compared with experiment. At this condition, the SimIce shape experiences light stall. GENCAS does a nice job capturing the lift hysteresis characteristics, just slightly under-predicting C_{Lmax} but capturing the recovery of lift during the downstroke. Current CFD prediction shwos a gentler moment stall and a more benign nosedown pitching moment at the peak of the oscillation.

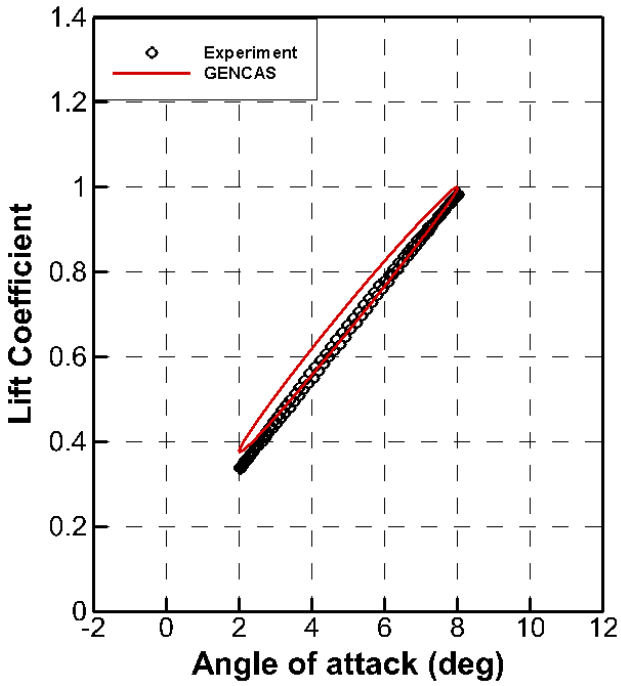

a) Clean Airfoil

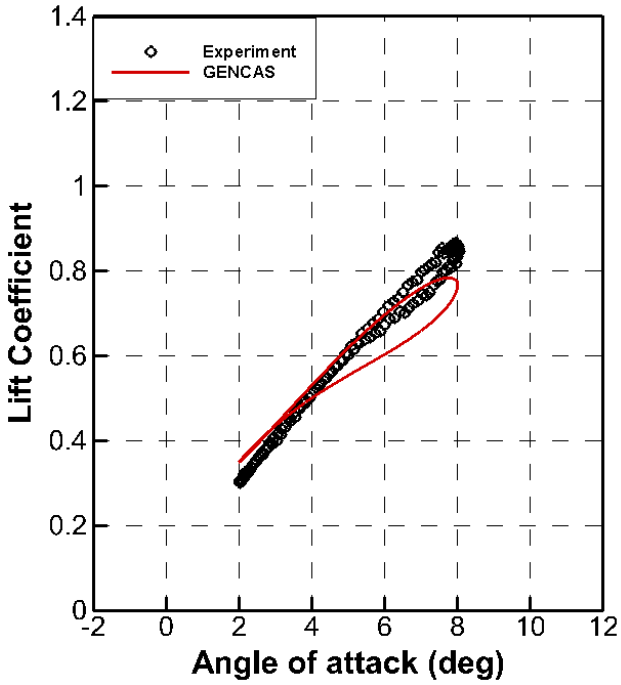

b) SimIce

Figure 3.5: Comparison of C_l, $\alpha = 5° \pm 3°$, f = 2,8Hz, 150 knots.

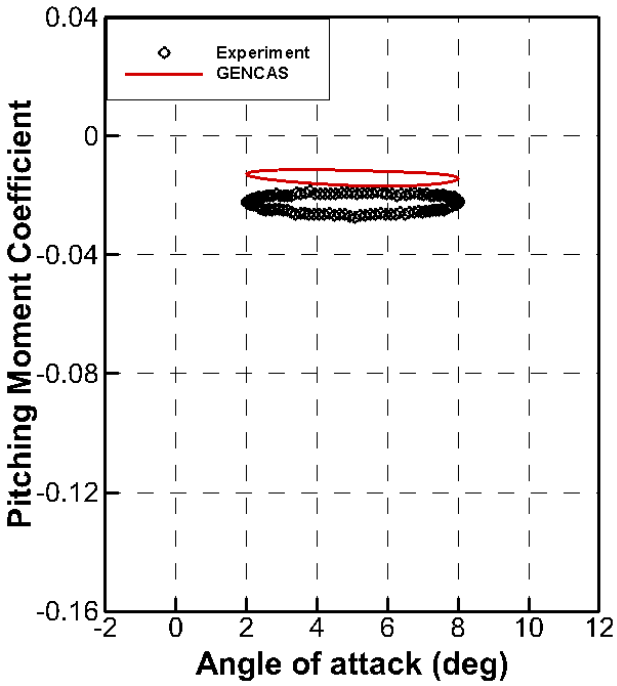

a) Clean Airfoil

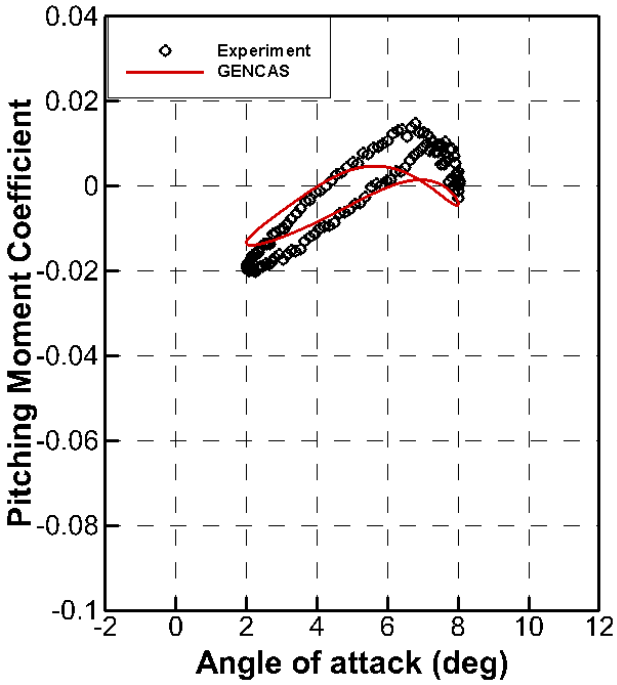

b) SimIce

Figure 3.6: Comparison of C_m, $\alpha = 5° \pm 3°$, f = 2,8Hz, 150 knots.

An oscillating clean and SimIce airfoil were simulated and compared with another CFD simulation and measured data. Dynamic performance of these airfoil pitching about the quarter chord ±6 degrees from a mean angle of attack of 5 degrees is presented in Figure 3.7 and Figure 3.8. As indicated in the figures, the clean airfoil does not experience stall and performance is easier to predict. Pitching moment performance behaves similarly for both flow solvers where the negative pitching moment seen in the calculations is slightly less when compared with experiment. At this condition, the SimIce shape experiences mild stall. GENCAS does a nice job capturing the lift hysteresis characteristics, just slightly under-predicting C_{Lmax} but capturing the recovery of lift during the downstroke. OVERFLOW does a reasonable job until the onset of stall, then like the static cases predicts more abrupt stall than what is experimentally observed. Despite this, OVERFLOW does very well predicting moment stall, then over-predicts the nose-down moment at the peak of the oscillation before capturing the recovery on the down stroke. GENCAS is predicting a gentler moment stall and a more benign nosedown pitching moment at the peak of the oscillation.

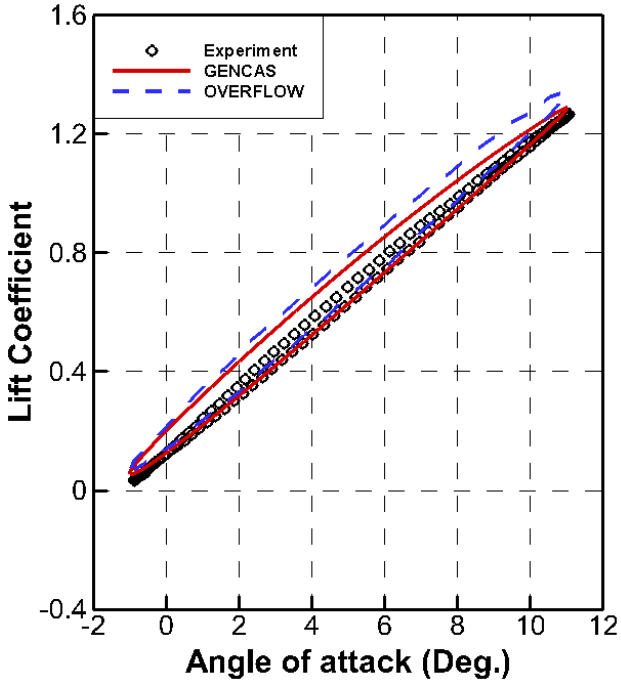

a) Clean Airfoil

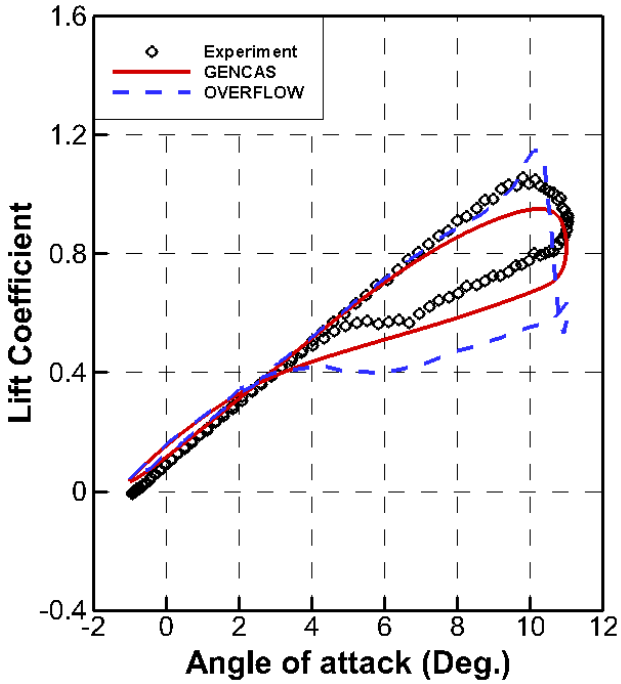

b) SimIce

Figure 3.7: Comparison of C_l, $\alpha = 5° \pm 6°$, f = 2,8Hz, 150 knots.

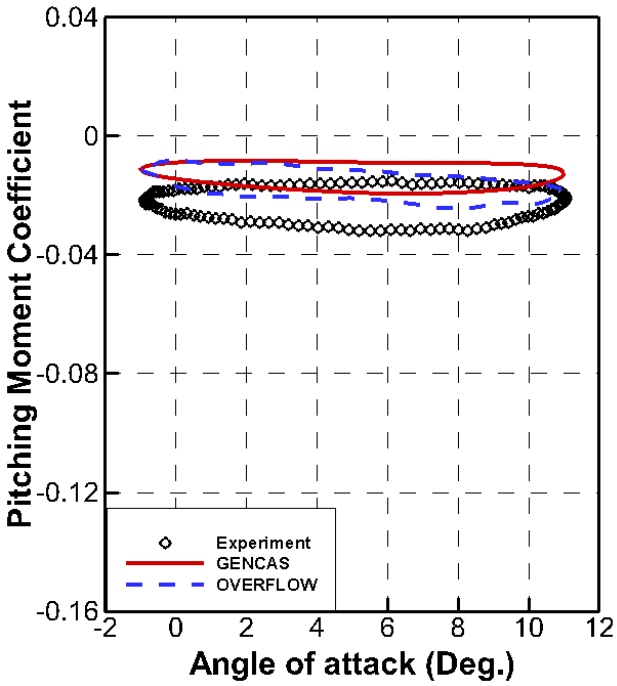

a) Clean Airfoil

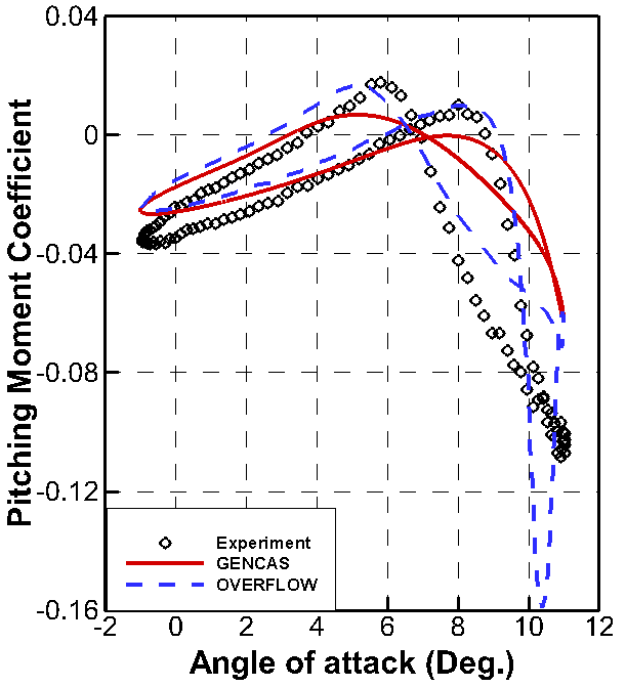

b) SimIce

Figure 3.8: Comparison of C_m, $\alpha = 5° \pm 6°$, f = 2,8Hz, 150 knots.

A deeper stall condition was examined with the airfoil oscillating in the same manner as previously discussed but pitching about a mean angle of attack of 10 degrees. Numerical simulation and experimental measurements for lift and pitching moment are presented in Figures 3.9 and 3.10. Mild stall is experimentally observed for the clean ice shape as indicated by the open hysteresis lift loop. Fully turbulent calculations by GENCAS and OVERFLOW do not predict this characteristic. When laminar conditions are enforces over the first 3% of the airfoil the lift curve begins to open though OVERFLOW still misses the characteristic observed in the experiment. As in the previous dynamic case, GENCAS does a better job than OVERFLOW in capturing the degraded lift performance of the SimIce shape, though it struggles with the pitching moment. OVERFLOW predicts the pitching moment stall well, but struggles post stall.

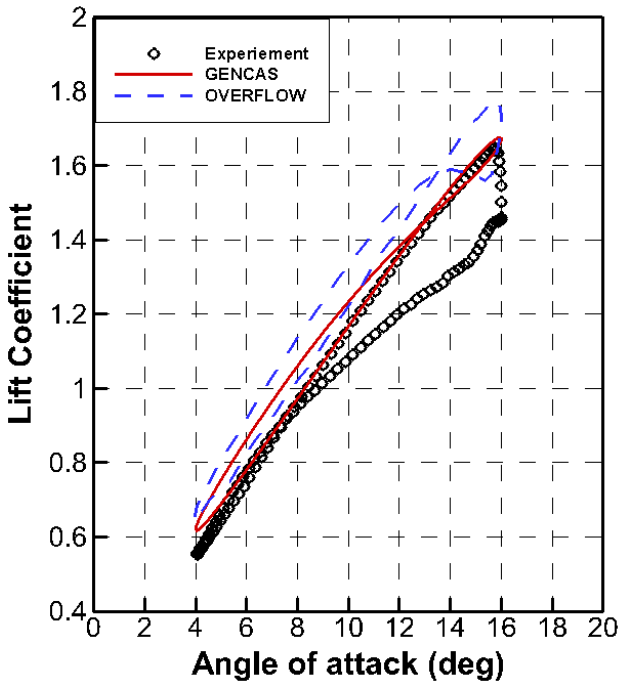

a) Clean Airfoil

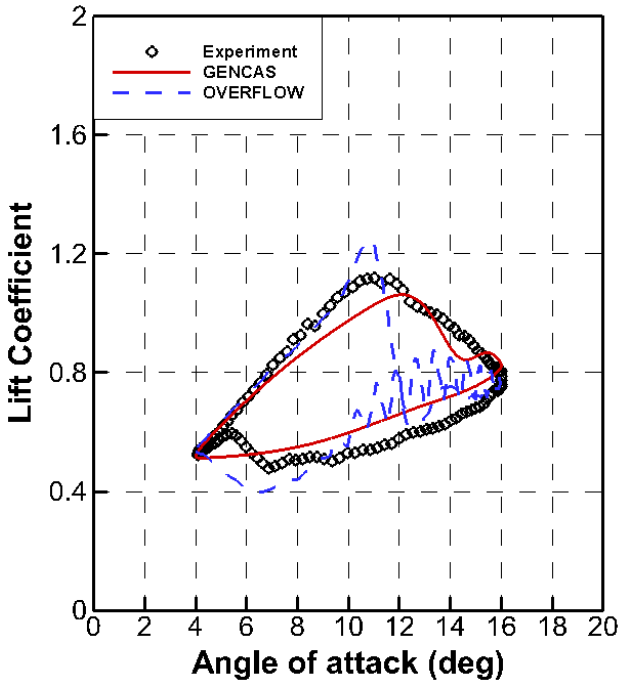

b) SimIce

Figure 3.9: Comparison of C_l, $\alpha = 10° \pm 6°$, f = 2,8Hz, 150 knots.

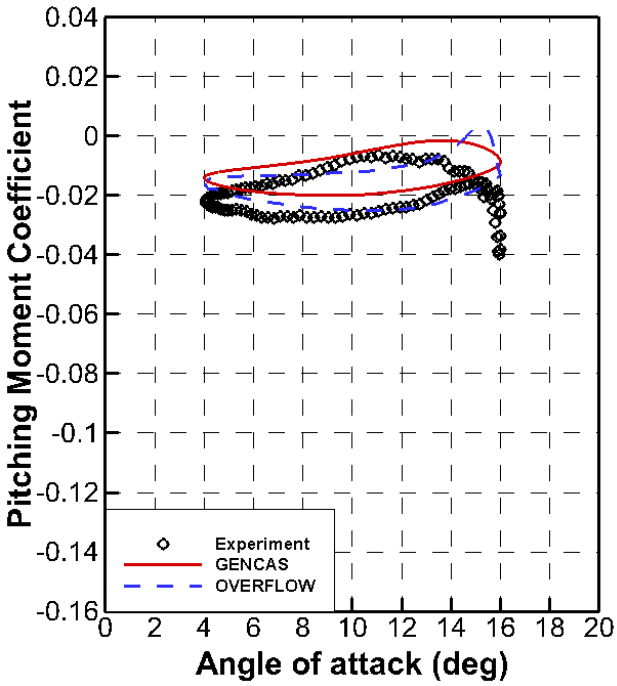

a) Clean Airfoil

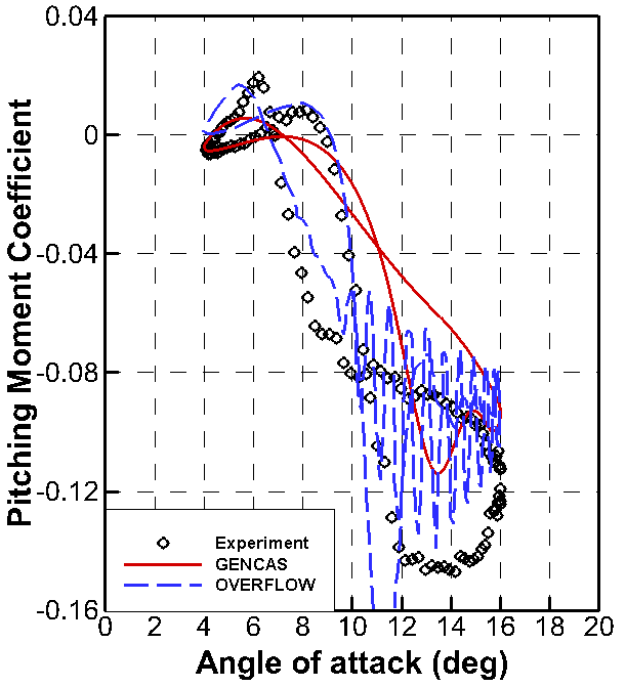

b) SimIce

Figure 3.10: Comparison of C_m, $\alpha = 10° \pm 6°$, f = 2,8Hz, 150 knots.

3.1.2 3-D Rotor Blade Case

3-D CFD simulations for helicopter rotor blades in hover and forward flight are done by GT-Hybrid. Computational results are compared against experimental data and simulation results from other CFD codes.

Rotor in Hover

CFD simulations for the S-76 rotor with swept tapered tip in hover have been conducted for a collective sweep of 2 to 12 degrees by increments of 2 degree. The S-76 blades are 1/4.71 scale and possess a -10° linear twist and a solidity of .0704. The blades have a radius of 1.423m (56.04 in.), a chord of .0787m (3.1 in.) and use the SC1095 and SCI094 R8 airfoils. The flight condition at a nominal tip Mach number of 0.65 was chosen for comparison. The tip Reynolds number based on chord length is 1.332 Million. The effect of aeroelastic deformation was not considered in this study.

Two different CFD grids are used to investigate the effect of grid density on hover performance. Figure 3.11 shows 3-D CFD grids used for simulations. A refined C-H grid has 291 points in the wrap-around direction, 98 radial grid points on the blade, and 45 points in the normal direction. A coarse C-H grid with 131 points in the wrap-around direction, 70 radial grid points on the blade, and 45 points in the normal direction was additionally generated using an in-house grid generator. For solutions presented in this paper, the Roe upwind, third order accurate scheme with the Spalart-Allmaras Detached Eddy Simulation (SA-DES) turbulence model is used. Figure 3.12 shows the effect of grid density on hover performance. Marginal difference is seen in prediction of thrust coefficient. The predicted torque starts to deviate as the collective pitch angle increases. The fine mesh predicted lower torque coefficients which are close to measurements. Both grids predicted a C_T/σ value of 0.09 at a collective of 9.5 deg. At this collective, tip vortex descent rate and contraction rate between two grids are compared in Figure 3.13. Tip vortex descent rates are almost same and there is difference for the contraction rate after 180 degrees of vortex age.

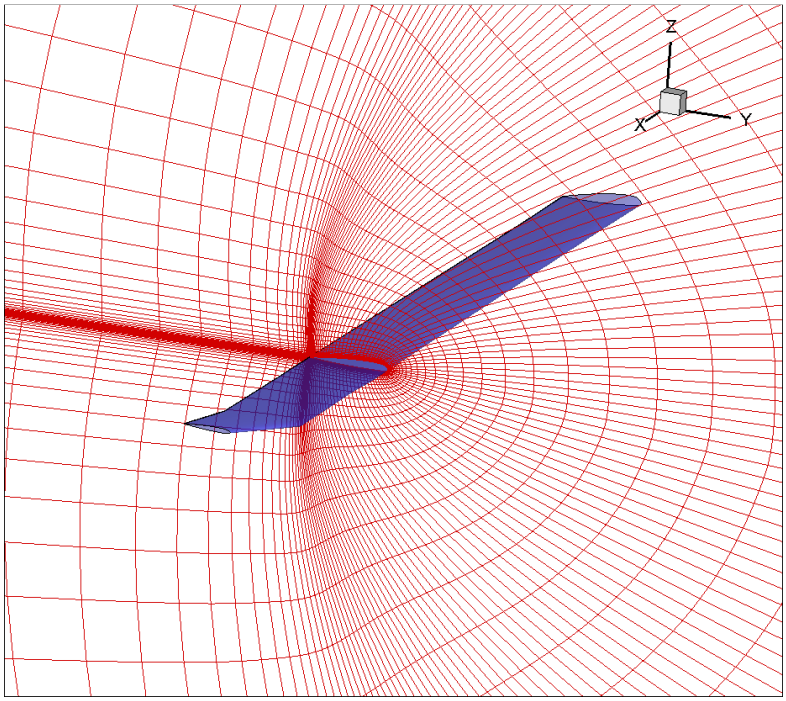

a) Coarse Grid (131 x 70 x 45)

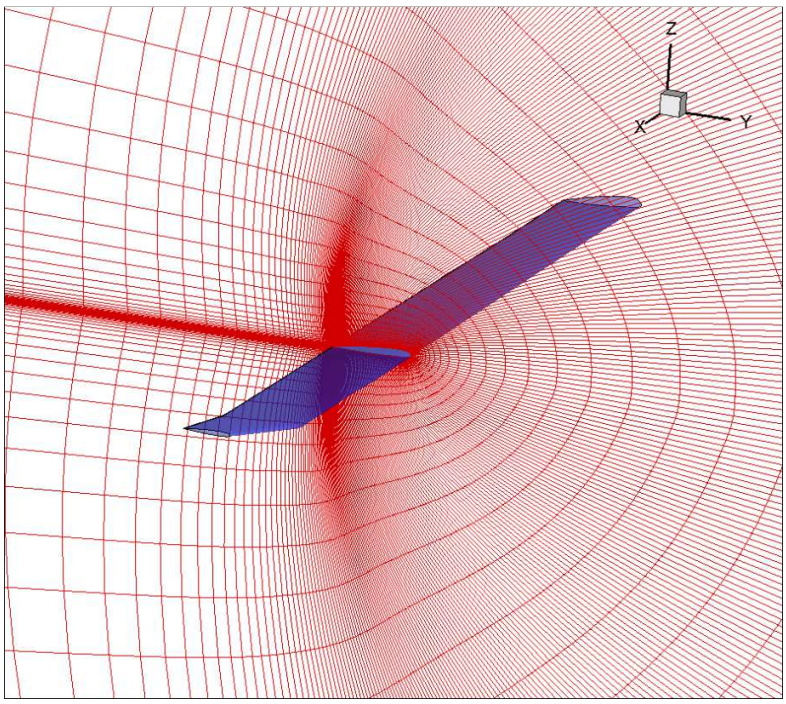

b) Fin Grid (291 x 98 x 45)

Figure 3.11: S-76 Rotor Blade Grid System.

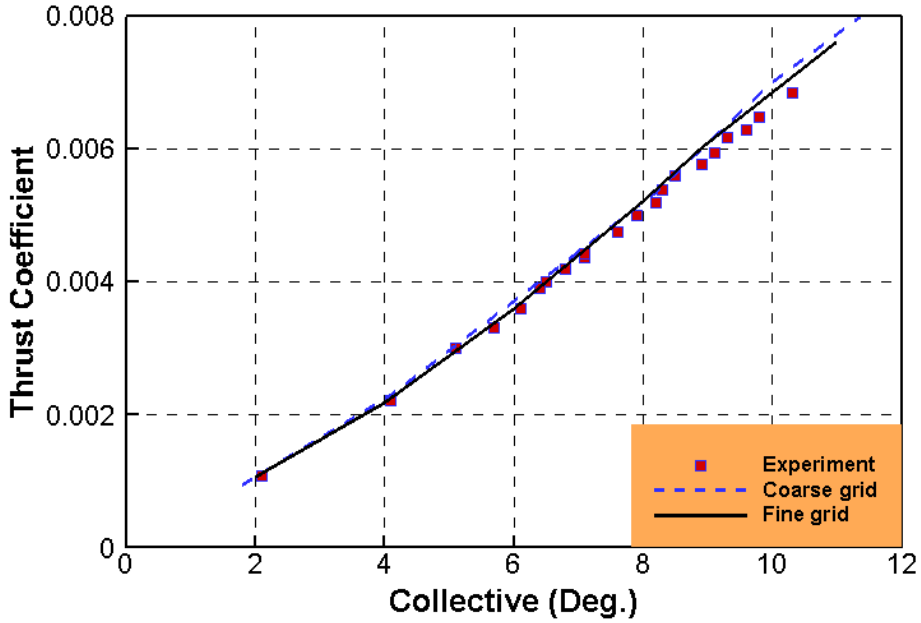

a) Thrust Coefficient vs Collective Pitch Angle

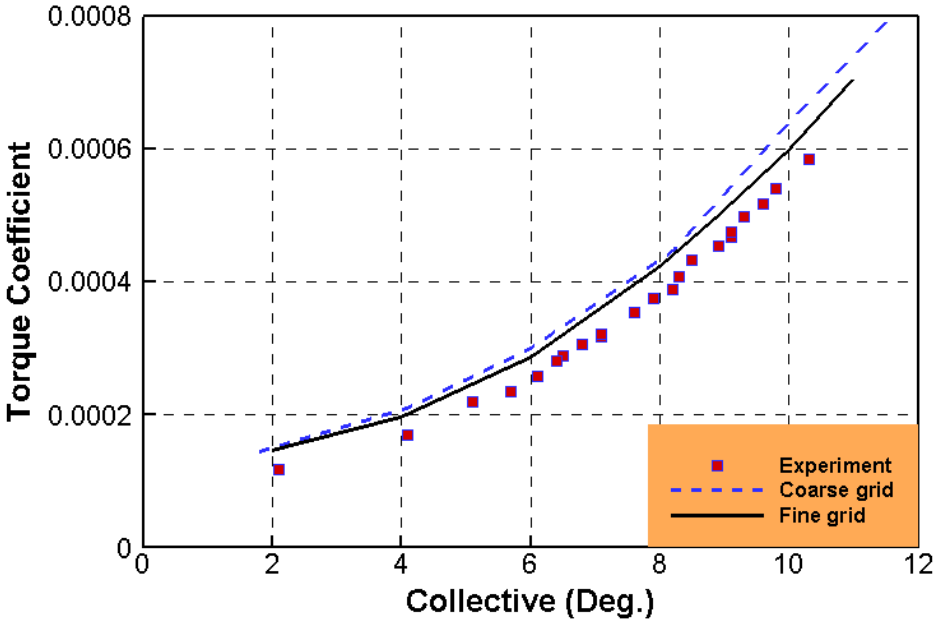

b) Torque Coefficient vs Collective Pitch Angle

Figure 3.12: Effect of Grid Density on Hover Performance Characteristics.

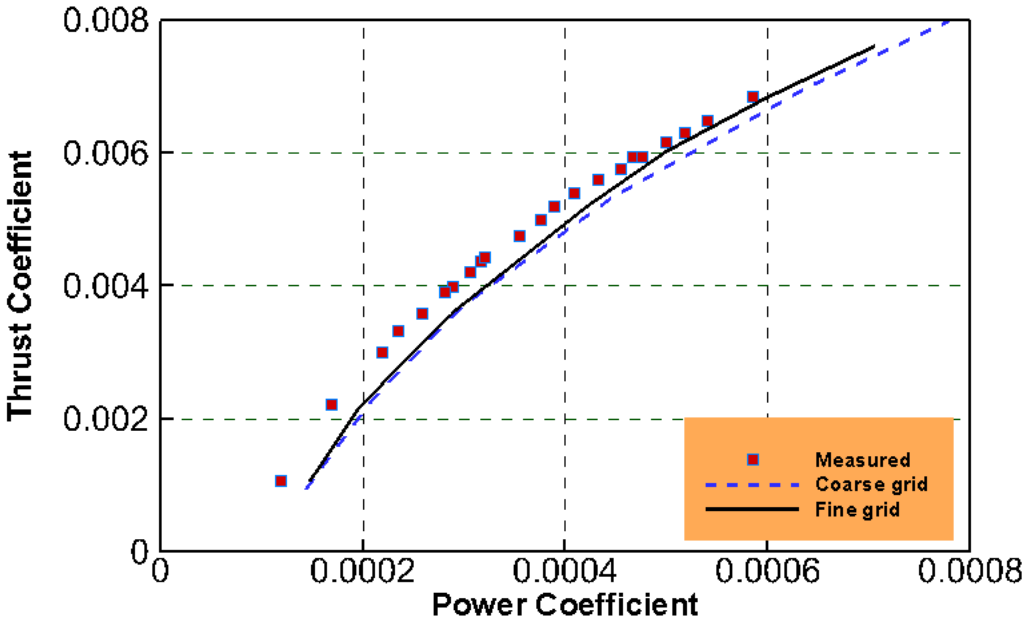

c) Thrust Coefficient vs Power Coefficient

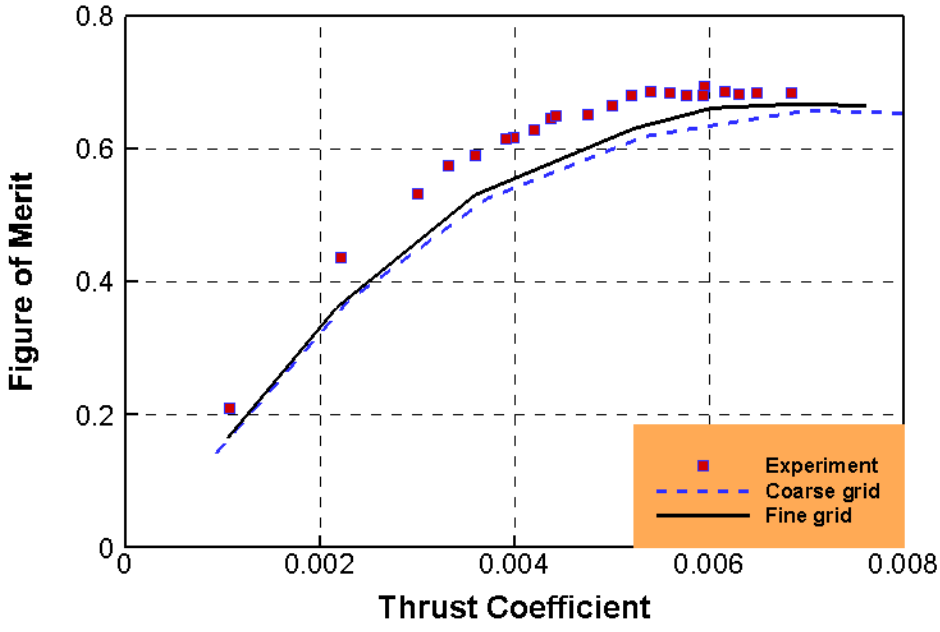

d) Figure of Merit vs Thrust Coefficient

Figure 3.12: Effect of Grid Density on Hover Performance Characteristics.

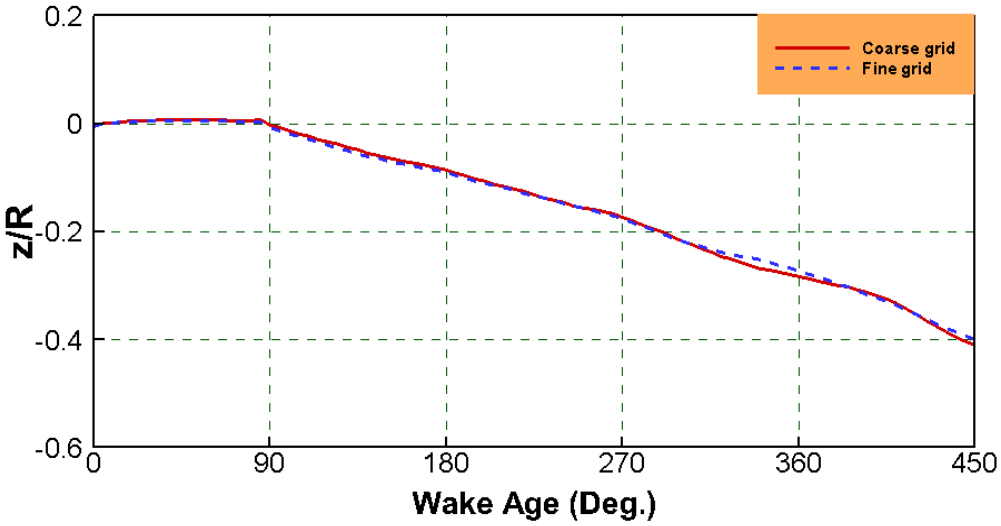

a) Tip Vortex Descent Rate

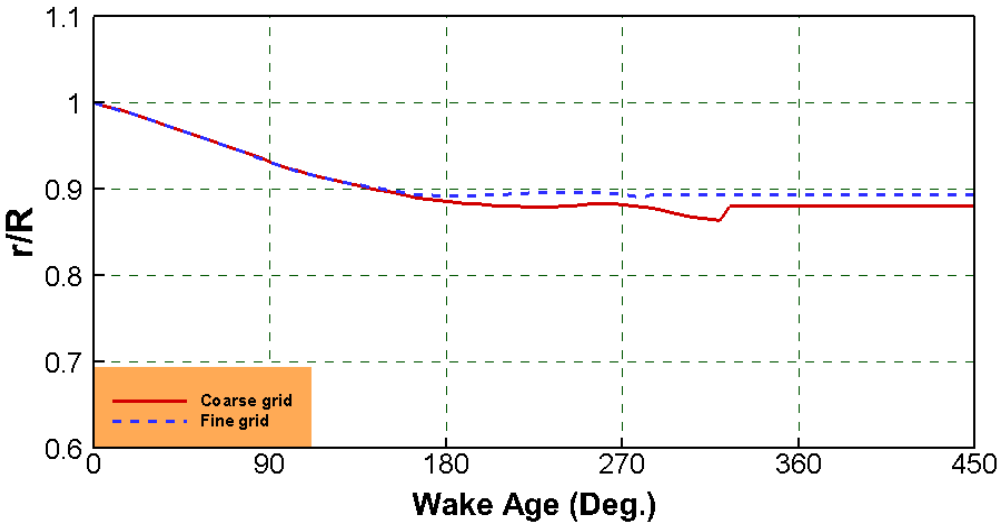

b) Tip Vortex Contraction Rate

Figure 3.13: Comparison of Tip Vortex Trajectory.

Comparison of GT-Hybrid results with several other Navier-Stokes simulations [80] are also shown in Figure 3.14. For the variation of C_T with the collective pitch, it is seen that all the computed data are in good agreement with each other. At higher pitch settings, GT-Hybrid has a tendency to slightly over predict the thrust coefficient. For the variation of torque coefficient with pitch, it must be noted that there has been no attempt

to use comparable grids or identical turbulence models. The methodologies have other differences with each other such as structured vs. unstructured, single block vs. overset, central vs. upwind, etc. Keeping these differences in mind, it is seen that OVERFLOW and GT-Hybrid tend to over predict the torque coefficient. The other analyses (Helios, OVERTURNS simulations done at University of Maryland, and the simulations done at KAIST) gave very favorable agreement with test data.

In vehicle performance, the thrust vs torque curve is of particular interest. The data shown in Figure 3.14 have been plotted as CT vs CQ plot. In this case, OVERTURNS and U2NCLE gave the best correlation with test data. All other simulations, including GT-Hybrid, tended to over predict the torque coefficient for a given thrust setting. This tendency to over predict the power (or torque) for a given level of thrust leads to an under prediction of the figure of merit in most of the calculations including GT-Hybrid. It is seen that only the OVERTURNS and U^2NCLE gave satisfactory results for Figure of Merit.

The hover performance is strongly influenced by rotor inflow, which in turn is influenced by the tip vortex trajectory. Figure 3.15 shows the tip vortex descent rate and contraction rate as a function of vortex age. There are no test data available. OVERTURNS and U2NCLE gave a slightly larger descent rate than the other methodologies. The present GT-Hybrid method uses a free vortex (Lagrangian) method in the near field with a far field trajectory model based on fitting the behavior at a specified wake age while all the other methods use a vortex capturing (Eulerian) method. As a result, good correlation between the present method and others could only be achieved for the first revolution, 360 degrees of vortex age, when the vortex is coherent with a very small vortex core radius. At higher vortex age, factors such as numerical diffusion, grid density, etc begin to cause deviations among the various methods. It was also observed that the GT-Hybrid methodology significantly underestimated the tip vortex contraction rate at higher wake ages, compared to other methods.

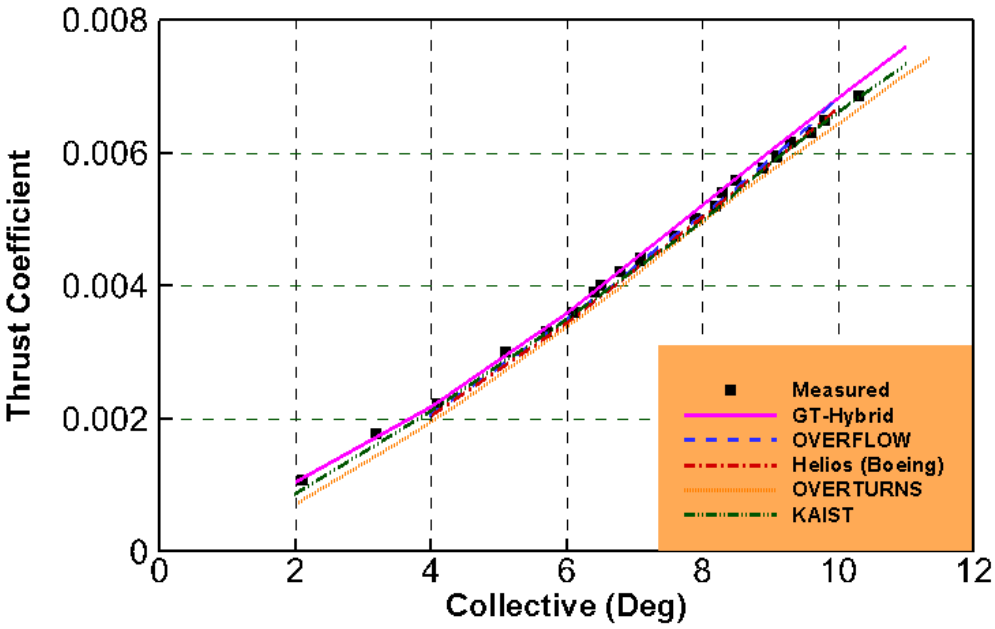

a) Thrust Coefficient vs Collective Pitch Angle

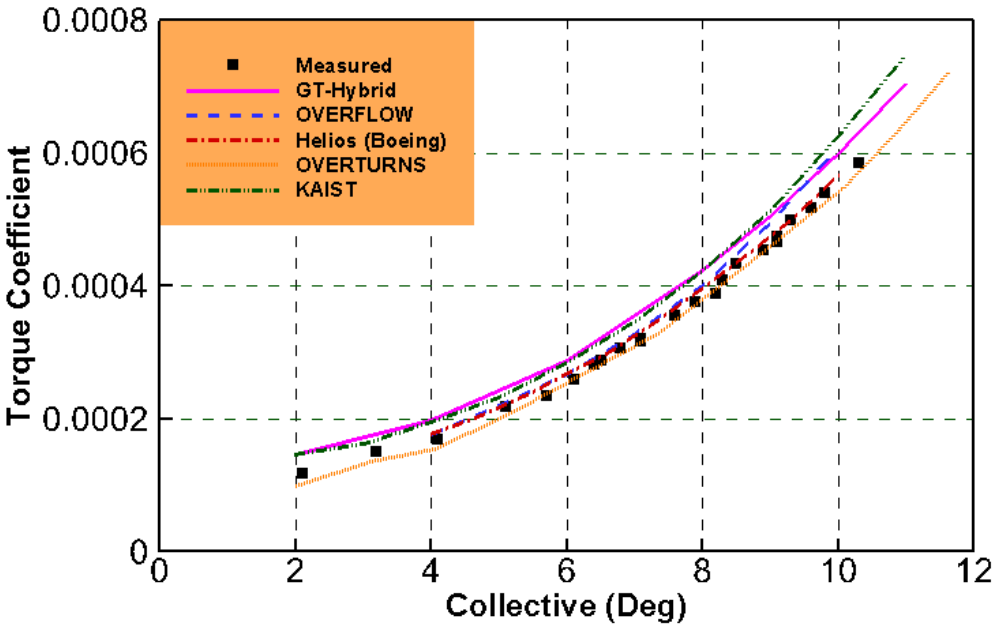

b) Torque Coefficient vs Collective Pitch Angle

Figure 3.14: Hover Performance Characteristics.

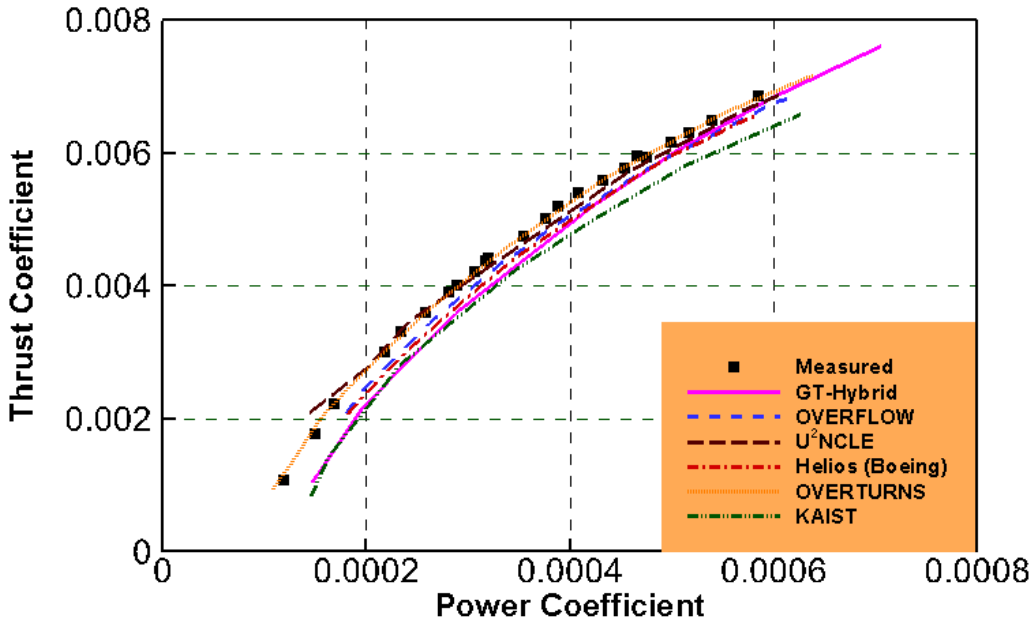

c) Thrust Coefficient vs Power Coefficient

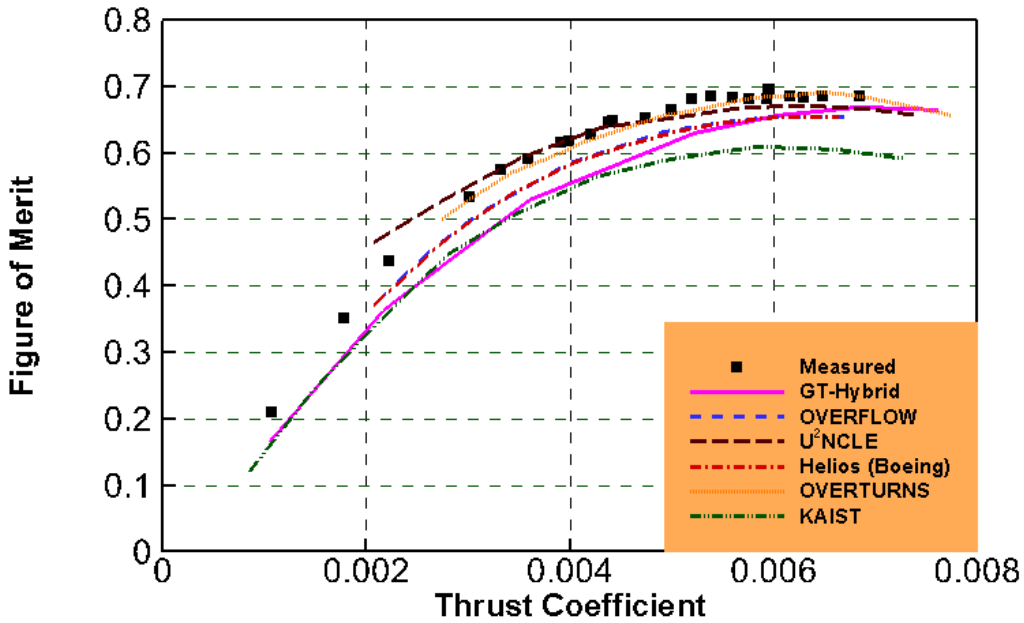

d) Figure of Merit vs Thrust Coefficient

Figure 3.14: Hover Performance Characteristics.

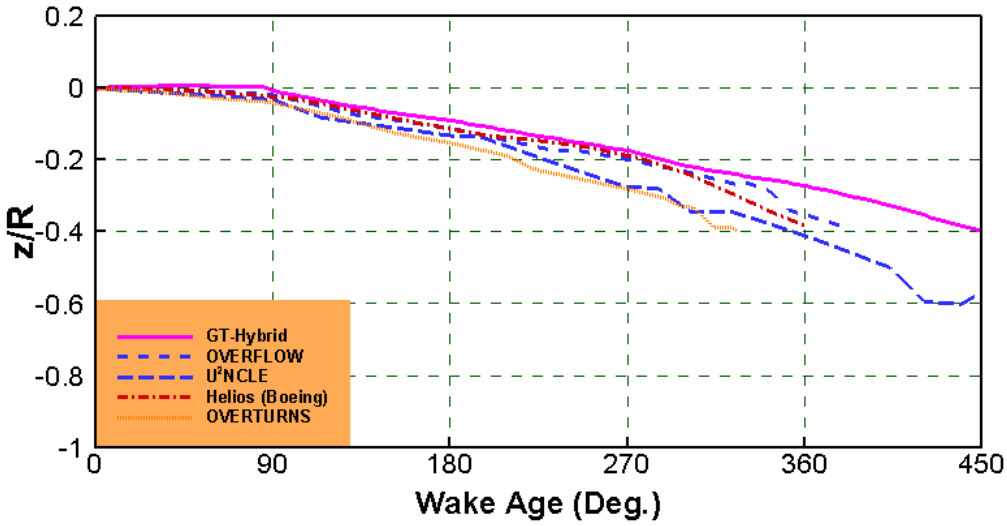

a) Tip Vortex Descent Rate

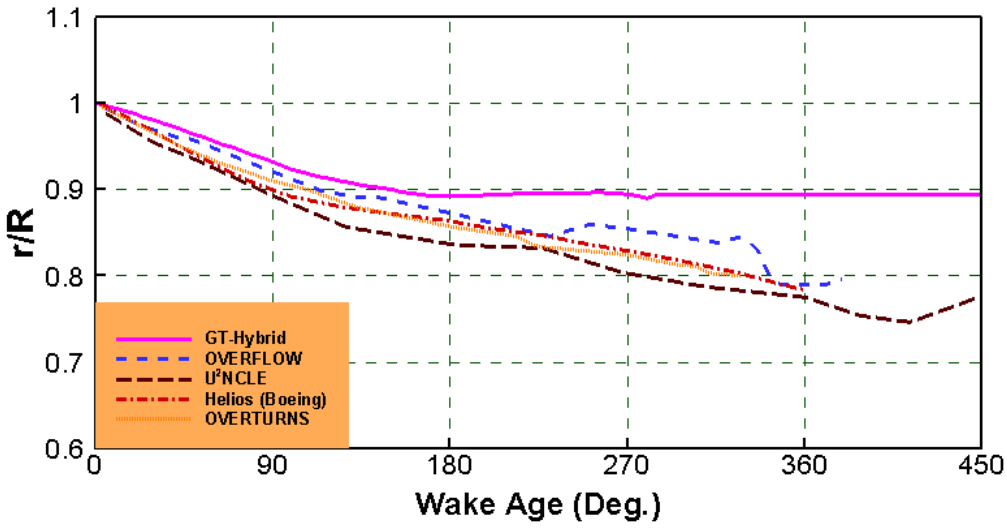

b) Tip Vortex Contraction Rate

Figure 3.15: Comparison of Tip Vortex Trajectory.

Rotor in Forward Flight

The next validation study of GT-Hybrid was performed for an AH-1G rotor in forward flight. The flight tests for AH-1G were performed at NASA Ames Research Center [81]. The rotor is a two-bladed rectangular-planform teetering rotor. The blade has a linear twist of -10 degrees from root to tip. The aspect ratio is 9.8. The flight condition chosen has an advance ratio 0.19, hover tip Mach number of 0.65, a Reynolds number of 9.73×10^6 and a thrust coefficient equal to 0.00464. The resolution in the azimuthal direction is 7200 per revolution, which corresponds to the azimuth angle increment of 0.05°. The measured blade first harmonics are presented in Table 3.1. These first harmonic values of flapping angle and control settings are used in current simulation. The precone and shaft tilt angles were set to zero during the computation.

A C-H grid with 131 points in the wrap-around direction, 70 radial grid points on the blade, and 45 points in the normal direction was generated using an in-house grid generator. Figure 3.16 shows a 3-D blade mesh for AH-1G rotor. For solutions presented in this paper, the Roe upwind, third order accurate scheme with the Spalart-Allmaras Detached Eddy Simulation (SA-DES) turbulence model is used. Due to the lack of trim procedure during the CFD run, the thrust coefficient from GT-Hybrid is under-predicted.

Figure 3.17 shows the surface pressure distributions at 60% and 91% span for different azimuth angles. The present results also compared with another CFD results [82]. For the 60% span, the suction peak at advancing side is slightly under-predicted. For the 91% span, the computed suction peak at advancing side is lower than the measurements. This under estimation of suction peak is also seen in Ref. 82. The computed pressure distributions on the retreating side are compared well with the flight test data

Figure 3.18 shows the sectional thrust variation at 60% and 91% of span. The present results are compared with flight test data and results of others [82]. The variations in loads in the present computations seem similar to those found in flight tests near 90

and 270 degree azimuth angles. Although various significant effects such as the influence of the fuselage, the hub, and the blade elastic deformations are not considered, the overall thrust distributions agree fairly well with flight test data.

Table 3.1: Blade Harmonics for AH-1G Rotor

	Experiment
C_T	0.00464
θ_0 (Deg.)	6.0
θ_{1c} (Deg.)	1.7
θ_{1s} (Deg.)	-5.5
β_{1s} (Deg.)	-0.15
β_{1c} (Deg.)	2.13

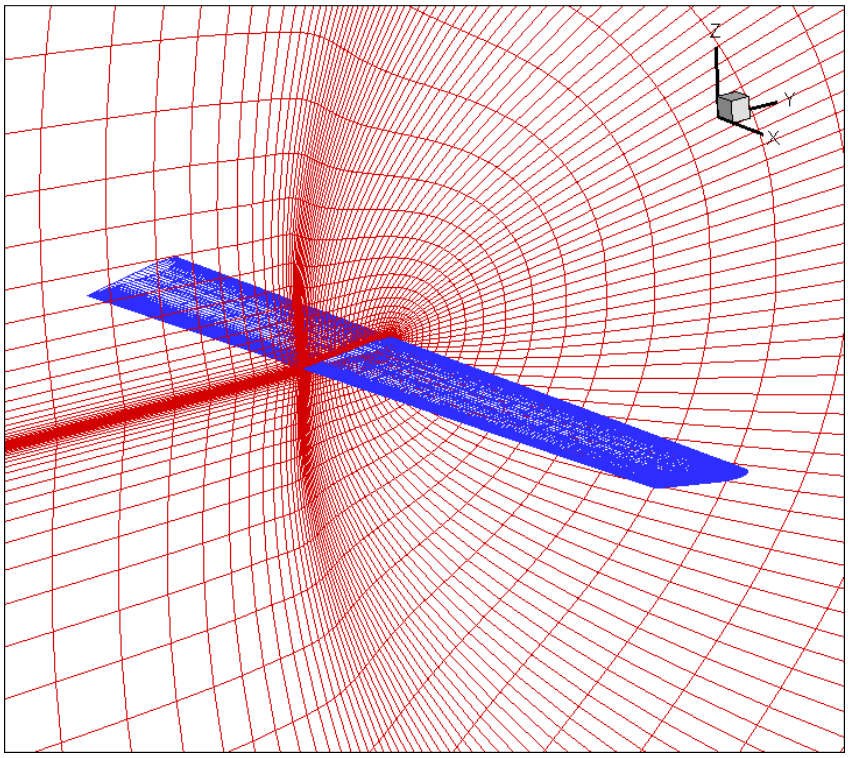

Figure 3.16: AH-1G Rotor Blade Grid System.

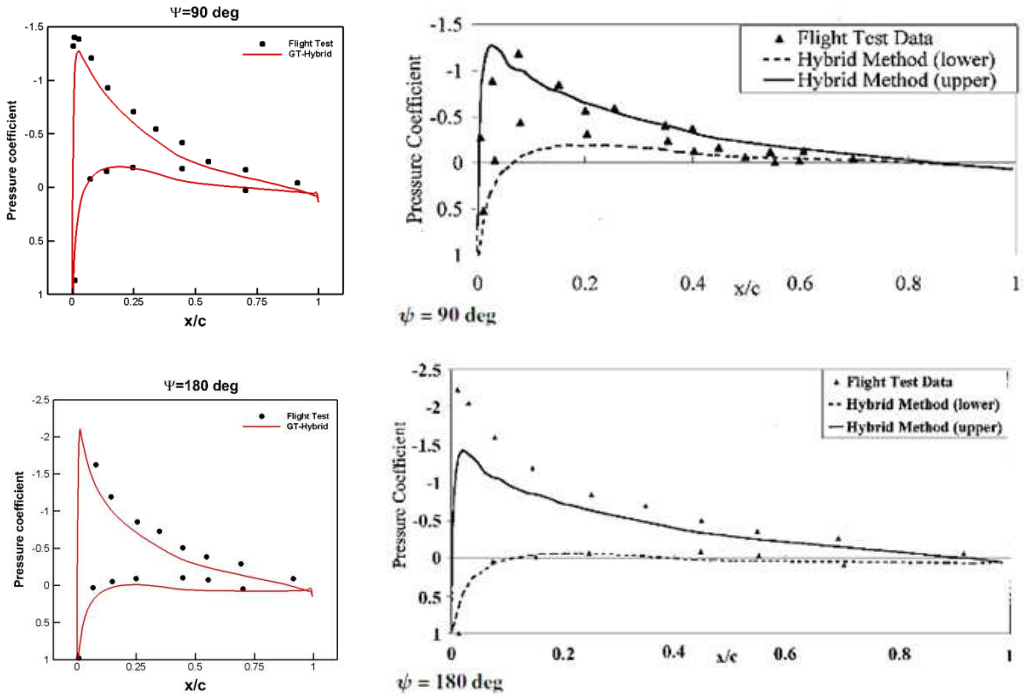

a) 60% Span (Left : Present, Right : Ref. [82])

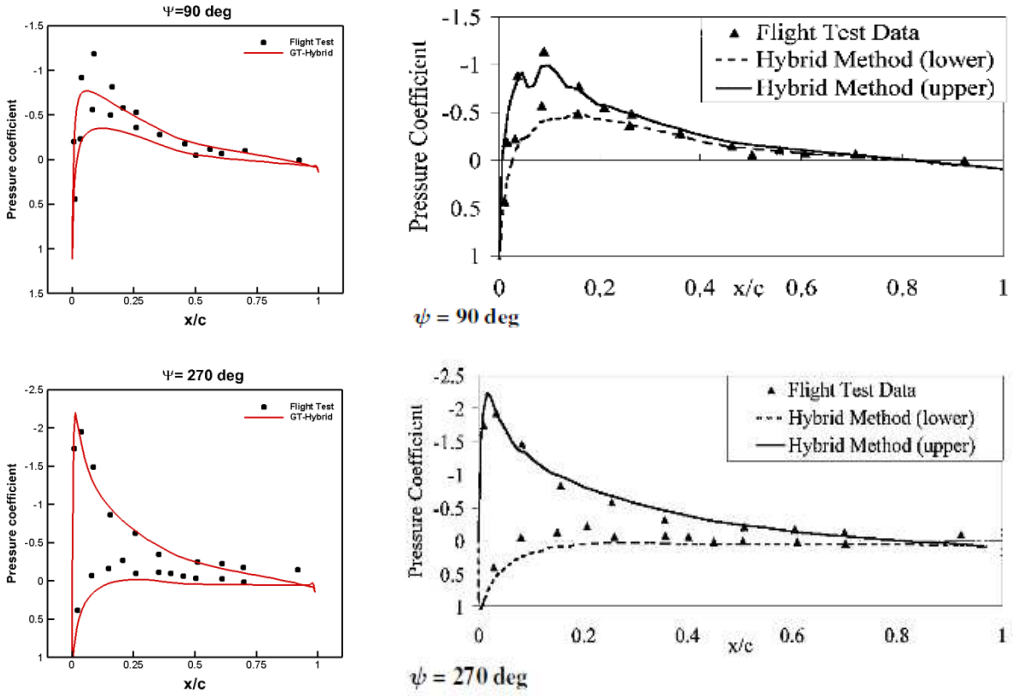

b) 91% Span (Left : Present, Right : Ref. [82])

Figure 3.17: Surface Pressure Distributions.

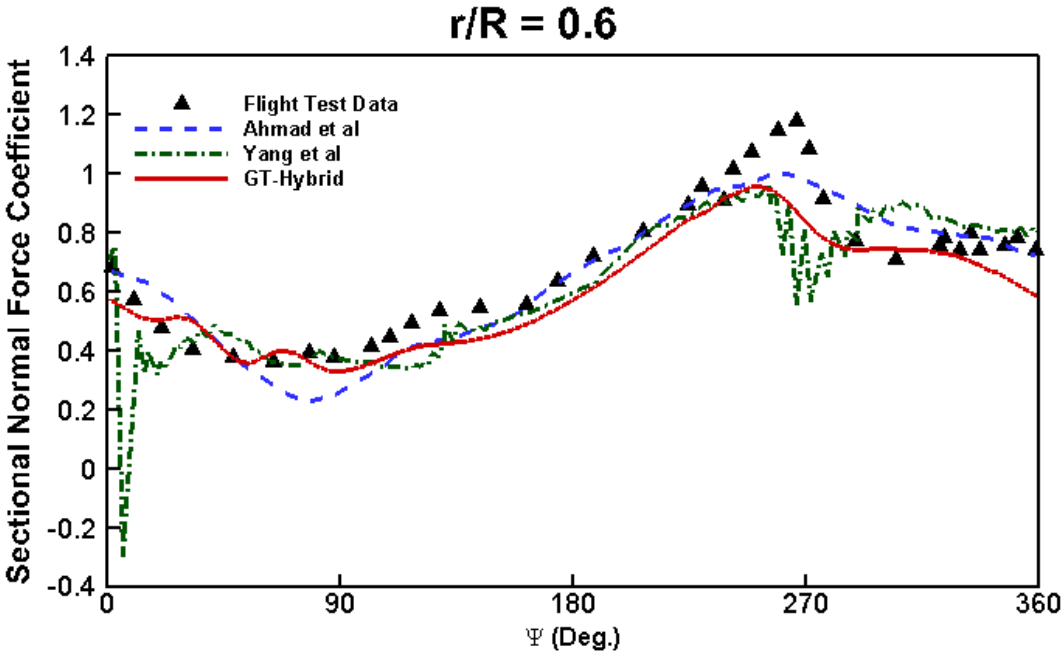

a) 60% Span

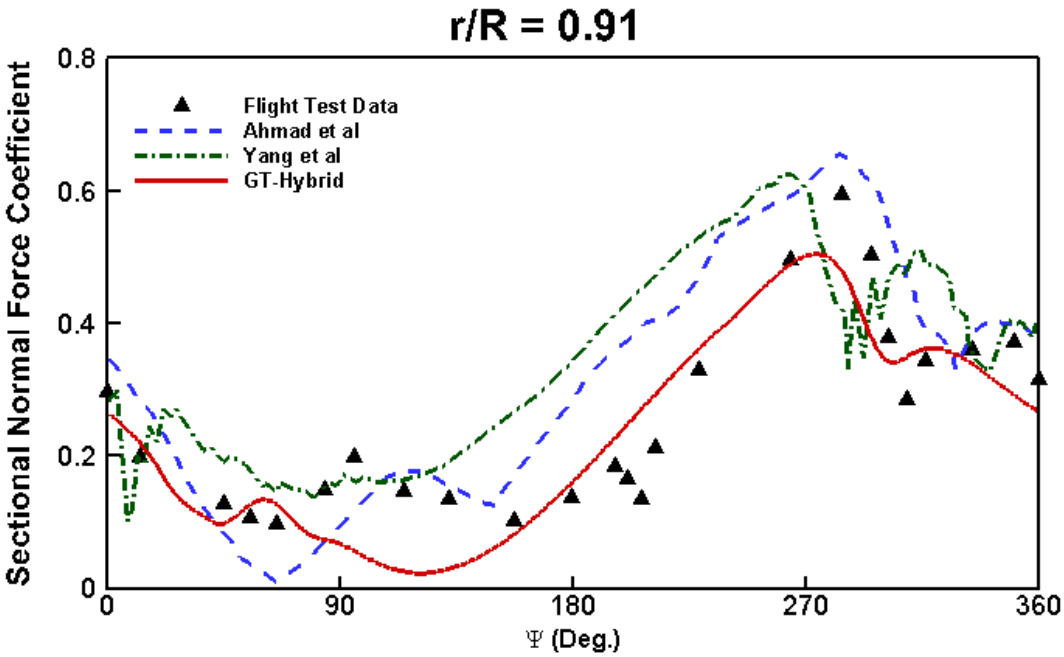

b) 91% Span

Figure 3.18: Comparison of Sectional Thrust for the AH-1G Rotor.

3.2 Validation of Water Droplet Solver

In this section, a number of calculations are presented to demonstrate the capabilities of the present Eulerian approach. Comparisons with industry-standard Lagrangian approaches found in LEWICE are also shown.

3.2.1 2-D Airfoil Case

Steady 2-D Airfoil

As a firs validation case, collection efficiency predictions have been done for NACA0012 airfoil, at three different angles of attack. The simulations are performed at a 0.31 free-stream Mach number with a constant droplet diameter of 20μm and an airfoil chord of 0.5334 m. The mean flow field is obtained from GENCAS. In the CFD simulation, Roe scheme with a 3rd order MUSCL reconstruction is used for flux calculations. A first order implicit LU-SGS scheme is used for marching in time. Spalart-Allmaras (SA) is used as the turbulence model. Figure 3.19 shows 2-D CFD mesh used for simulations.

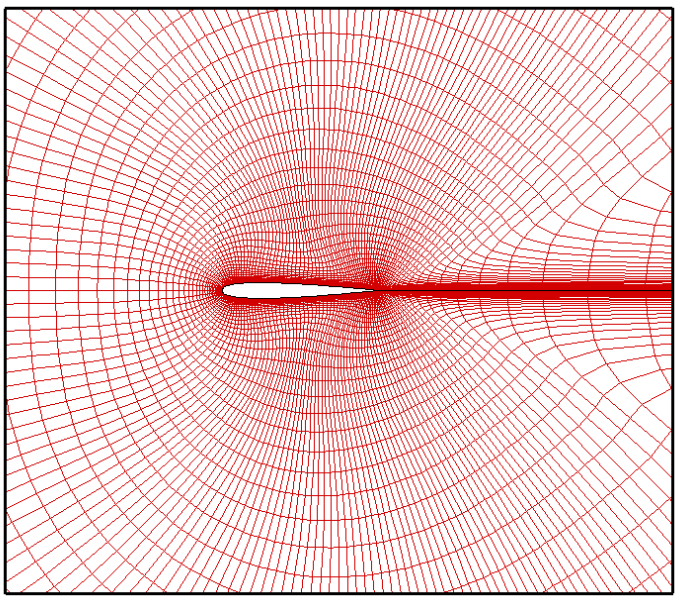

Figure 3.19: 2-D Grid for NACA0012 Airfoil [193 x 80].

Figure 3.20 shows a comparison of the collection efficiency from the present Eulerian simulations with the LEWICE Lagrangian results [83]. In general, the present results are in good agreement with LEWICE, providing confidence in the present method. It is found that the deviation between the two approaches grows with increased angles of attack. Similar discrepancies have been reported by Kinzel et al. [83] and Beaugendre et al. [84] in their comparisons between FENCAP-ICE and LEWICE. For the 4 deg. of angle of attack, the results from LEWICE are obtained at corrected angle of attack (3.5 deg.).

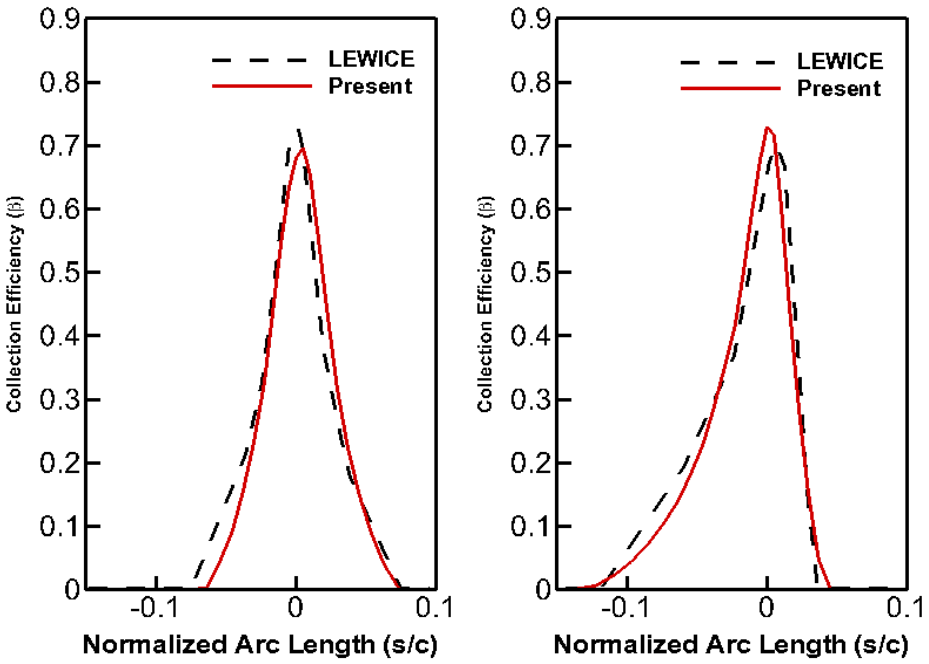

a) 0 deg. AoA

b) 4 deg. AoA

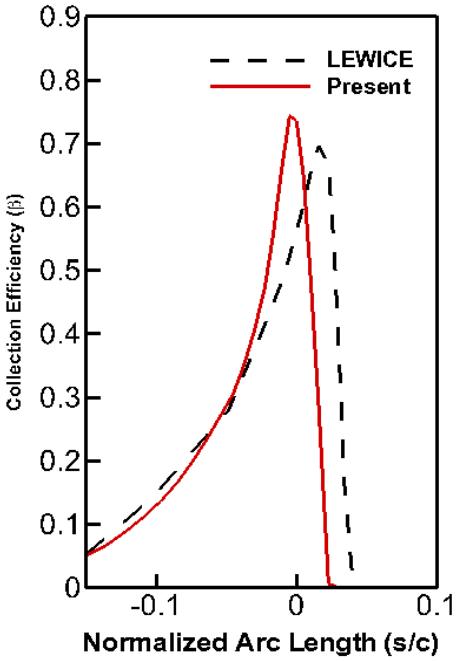

c) 8 deg. AoA

Figure 3.20: Comparison of Predicted versus LEWICE Collection Efficiencies for a NACA0012 Airfoil. (Wall Corrections have not been used in the simulations)

Next, the collection efficiency simulations are reported for the MS317 airfoil. This configuration was chosen because of the availability of collection efficiency and pressure distributions data at various mean flow conditions, collected over 1997 and 1999 [70]. GENCAS is used to obtain flowfield data. In the CFD simulation, Roe scheme with a 3rd order MUSCL reconstruction is used for flux calculations. 1st order implicit LUSGS scheme is used for marching in time. Spalart-Allmaras (SA) is used as a turbulence model. Figure 3.21 shows 2-D CFD mesh used for simulations. The predicted pressure distributions are compared with experimental data in Figure 3.22. Predicted pressure distributions at the bottom surface are in good agreement with experiment. Some differences between the computed and measure pressure distributions are observed near the trailing edge, but this is expected to play on a minor role in the collection efficiency near the leading edge. The effect of first cell distance from airfoil surface is examined. Marginal difference is seen among results.

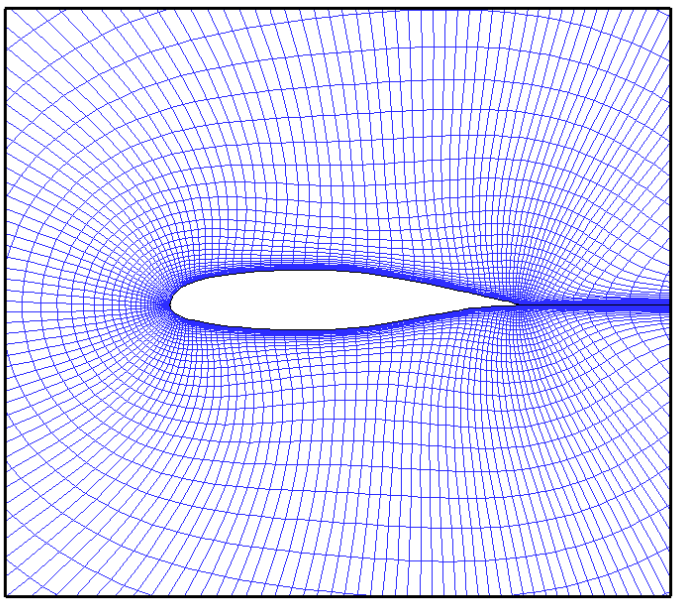

Figure 3.21: 2-D Grid for MS317 Airfoil [193 x 65].

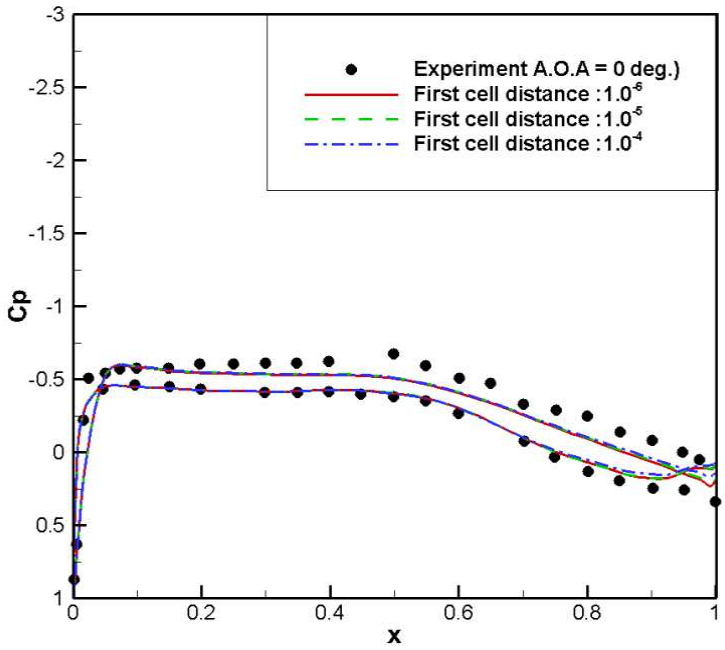

Figure 3.22: Comparison of Pressure Distribution for MS317 Airfoil.

The effect of median volumetric diameter (MVD) on collection efficiency is investigated. The icing test conditions are given in Table 3.2. The effect of first cell distance normalized by chord length was also investigated because the droplet solver updated the values at boundary by using the values of first inner cell. It is found that the collection efficiency is relatively insensitive to the normal height of the first row of cells over the wall. It is expected that the deviation in the flowfield between present simulation and the test data would only have a negligible effect on the collection efficiency distribution around the leading edge. In the experiment, collection efficiency was measured for 0 and 8 degree of angle of attack and MVDs of 11.5, 21, and 92μm.

Table 3.2: Test Conditions for MS317 Airfoil

Parameter	Value
Chord (m)	0.914
U_∞ (m/sec)	78.66
Re (Million)	4.83
AOA (Degree)	0 / 8
MVD (μm)	11.5 / 21.0 / 92.0

Figure 3.23 and 3.24 present the comparison of local impingement efficiency distributions between present prediction and measurement according to different value of MVD at 0° and 8°. The x-axis (surface distance) is normalized by airfoil chord length. The positive values correspond to the lower surface of the airfoil. The peak value of collection efficiency increases with MVD size. For an angle of attack of 0°, the laser system shows higher impingement efficiency values near the region of maximum impingement efficiency. In Ref. 70, the reason for this discrepancy is explained. It was attributed to a small level of dye penetration into the blotter. In the present simulation, the impingement limits are under-predicted except for the 92 μm case for which the predicted collection efficiency is considerably higher and the peak value is greater than the measurement. A similar over-prediction is seen in the results from LEWICE in Ref. 70. Possible reasons for these large differences between simulation and experiment was investigated in Ref. 70. One of the cited reasons was the errors associated with measuring MVD for the 92-94 μm cases. Another plausible reason is droplet splashing and breakup.

Additional studies were performed for this test condition and it was found that droplet splashing and breakup occurs near the airfoil leading edge region. For the high angle of attack case, the location of peak value of collection efficiency was shifted downstream on the lower surface of the airfoil. Simulation results are shifted to the left with respect to the experimental data, if the angle of attack is not corrected for wall effects.

The effect of first cell distance on collection efficiency is investigated in Figure 3.23-b). Marginal difference in collection efficiency is observed. The effect of droplet splashing is investigated in Figures 3.23-c) and 3.24-c). An improvement in the prediction is seen when the collection efficiency is modified to account for splashing.

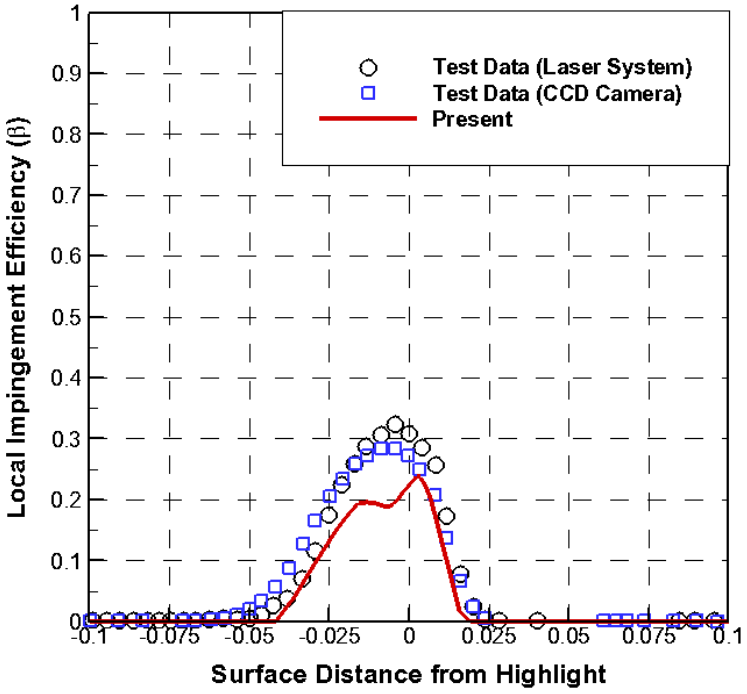

a) MVD = 11.5

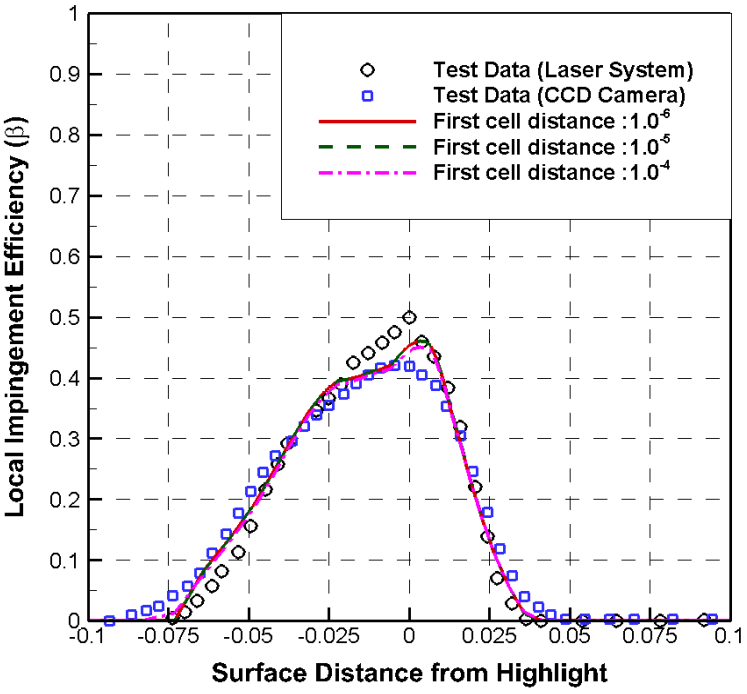

b) MVD = 21

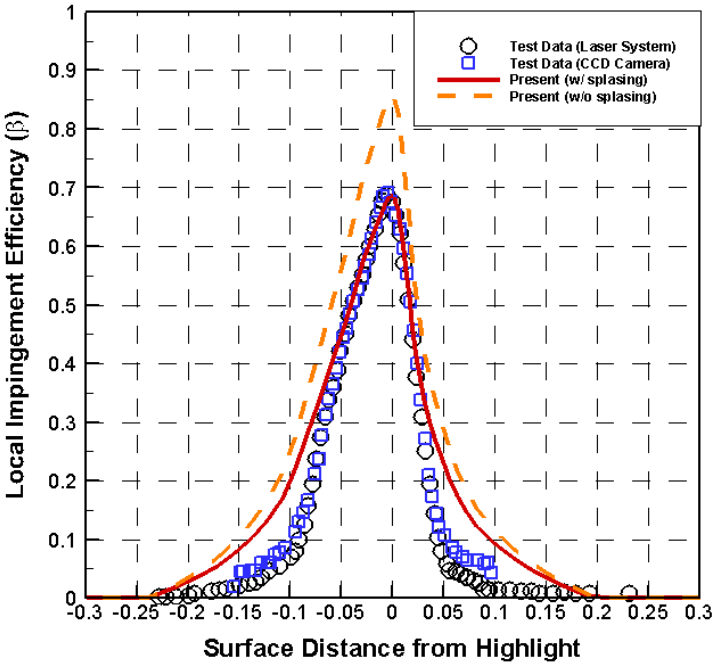

c) MVD = 92

Figure 3.23: Comparison of Collection Efficiency for MS317 airfoil at Zero Angle of Attack.

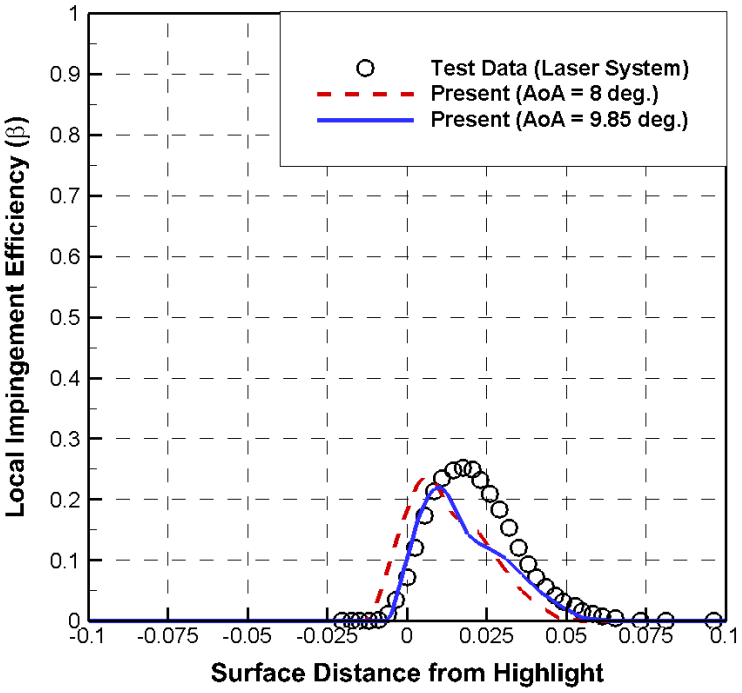

a) MVD = 11.5

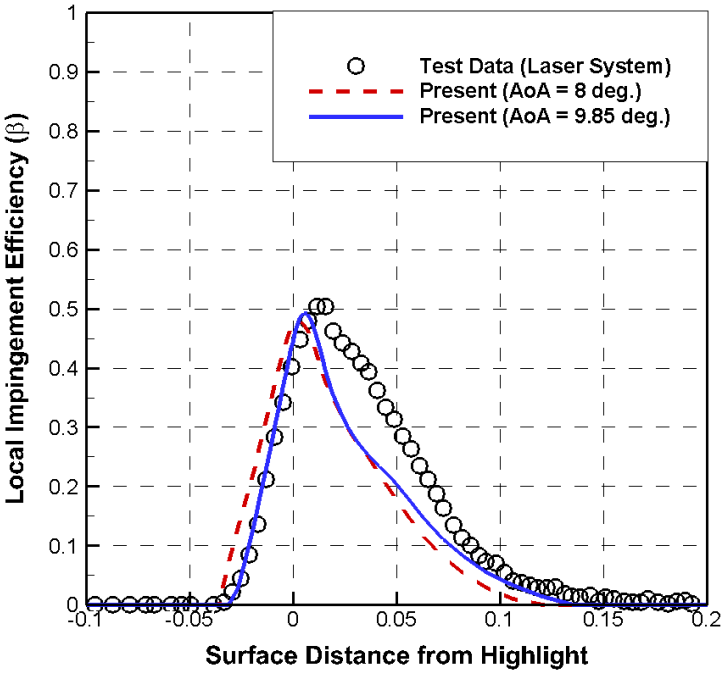

b) MVD = 21

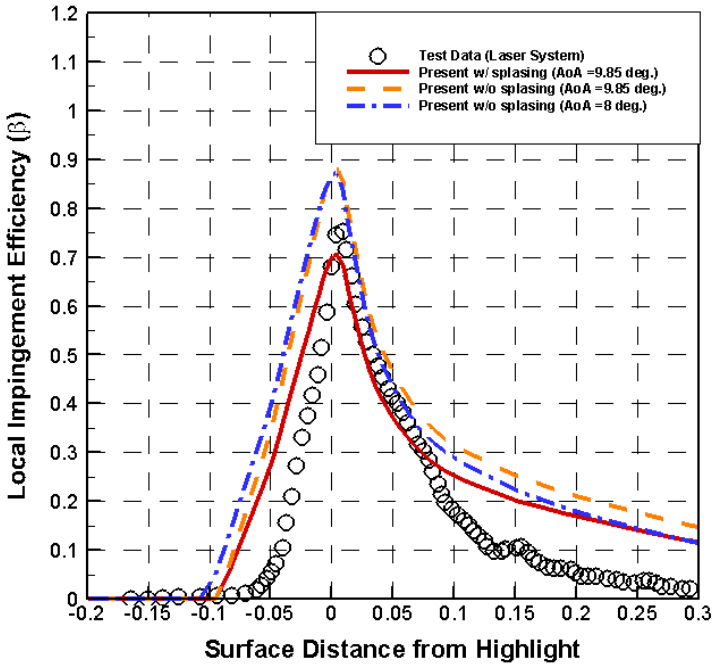

c) MVD = 92

Figure 3.24: Comparison of Collection Efficiency for MS317 airfoil at 8 Degrees Angle of Attack.

Oscillating 2-D Airfoil

Collection efficiency calculations have been performed for an oscillating SC2110 airfoil and comparisons with LEWICE have been made. The airfoil has a chord length of 0.381m, and operates at a freestream Mach number of 0.4208. Unsteady flowfield data for each angle of attack were obtained using a version of OVERFLOW. Figure 3.25 shows O-type 2-D CFD mesh used for simulations.

The simulations employ a nominal MVD size of 22 μm. The collection efficiency is computed for -1, -0.75, 0.15, 5, 8.53 and 11 degrees of angle of attack. Comparisons of collection efficiency between the present simulation and LEWICE for oscillating SC2110 airfoil are presented in Figure 3.26 at several angles of attack. The present Eulerian approach shows a spatial distribution of collection efficiency similar to LEWICE. The peak values from the two approaches are in reasonable agreement. It is found that the present Eulerian simulation shows a wider surface region with significant collection of water droplets compared to the Lagrangian simulation.

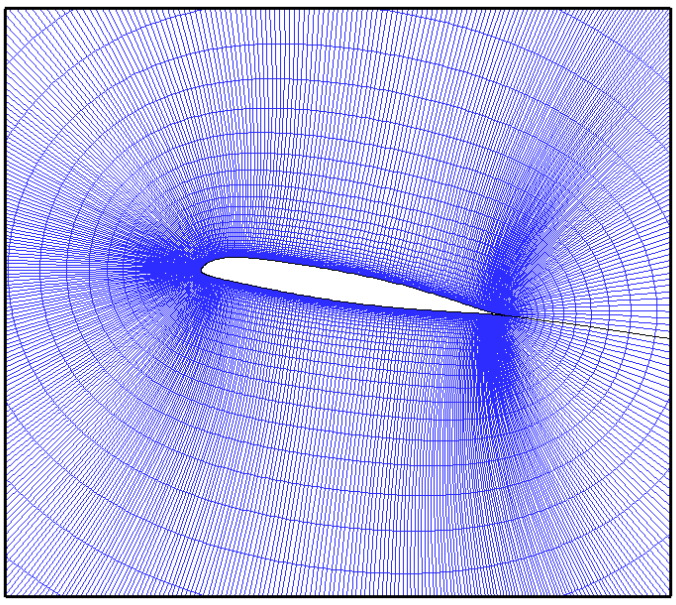

Figure 3.25: 2-D Grid for SC2110 Airfoil [497 x 65].

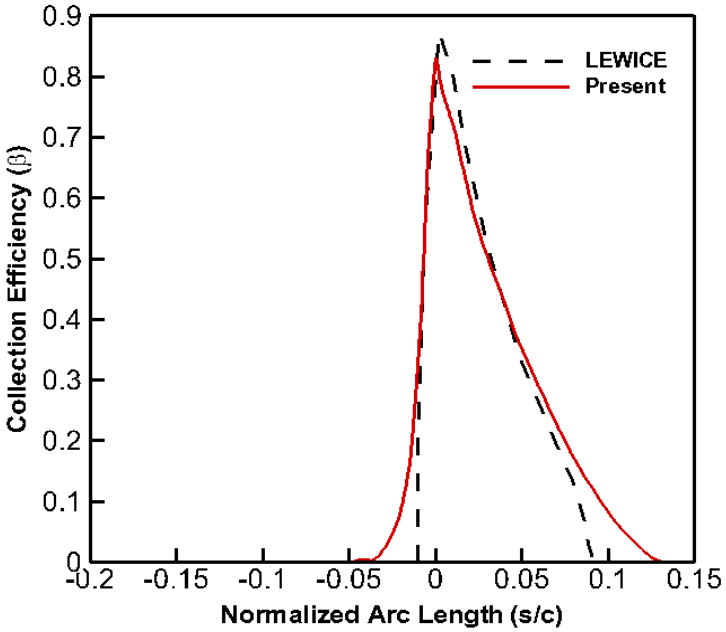

a) AoA = -1 deg.

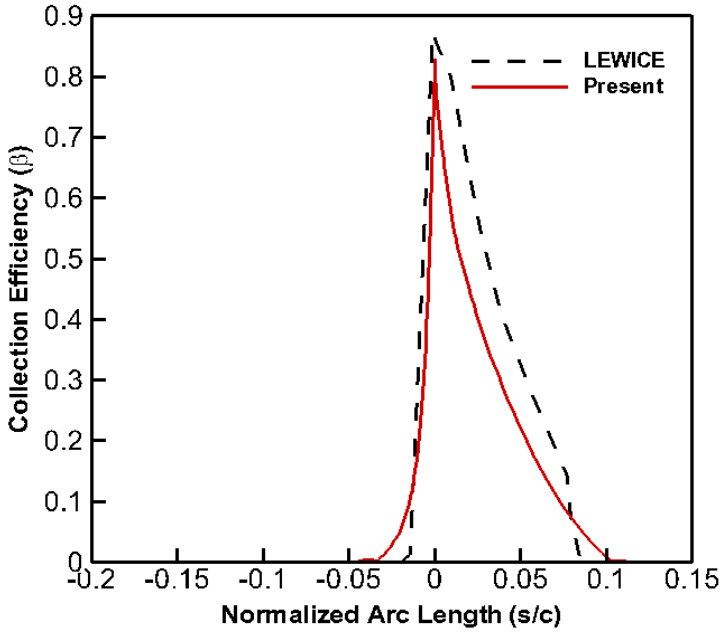

b) AoA = -0.71 deg.

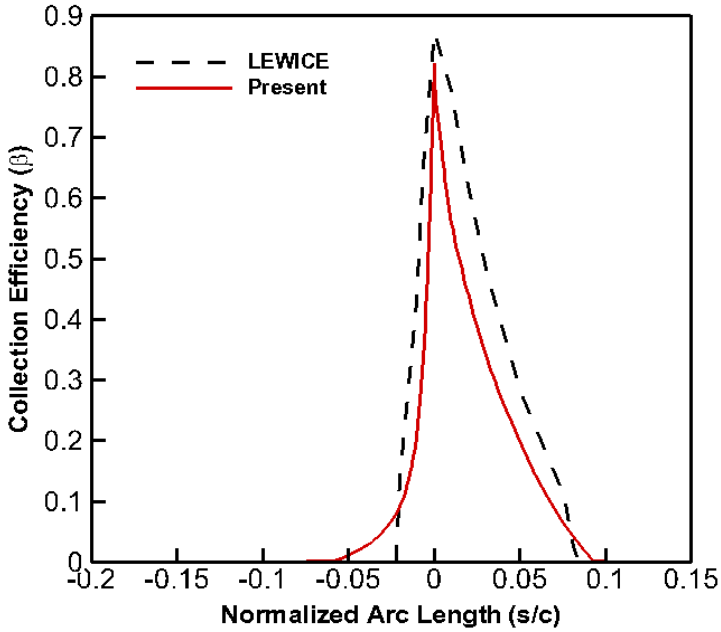

c) AoA = 0.15 deg.

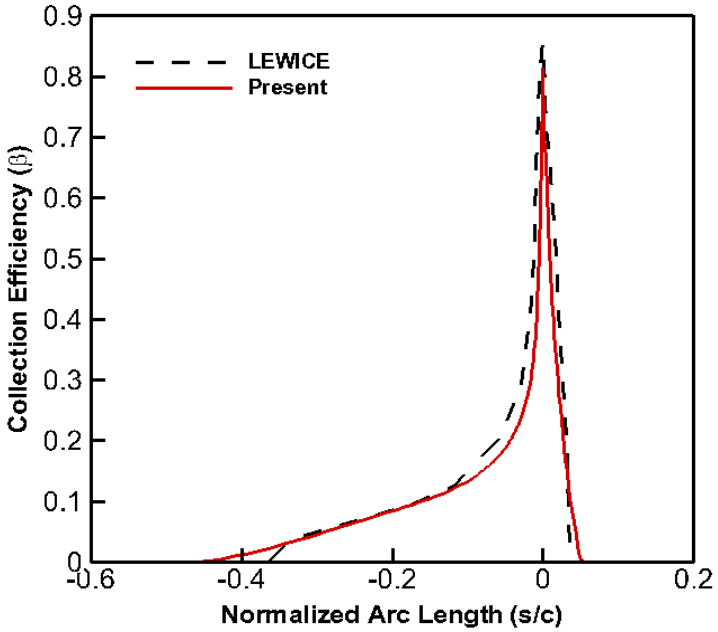

d) AoA = 5 deg.

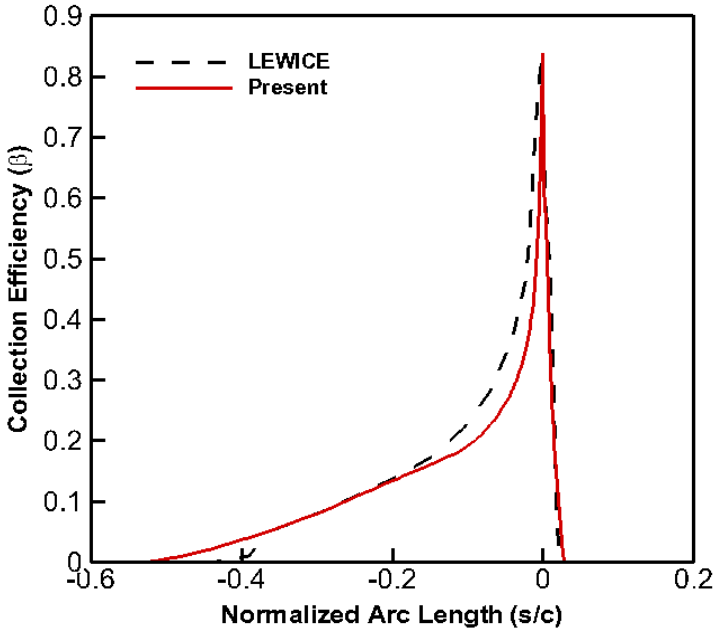

e) AoA = 8.53 deg.

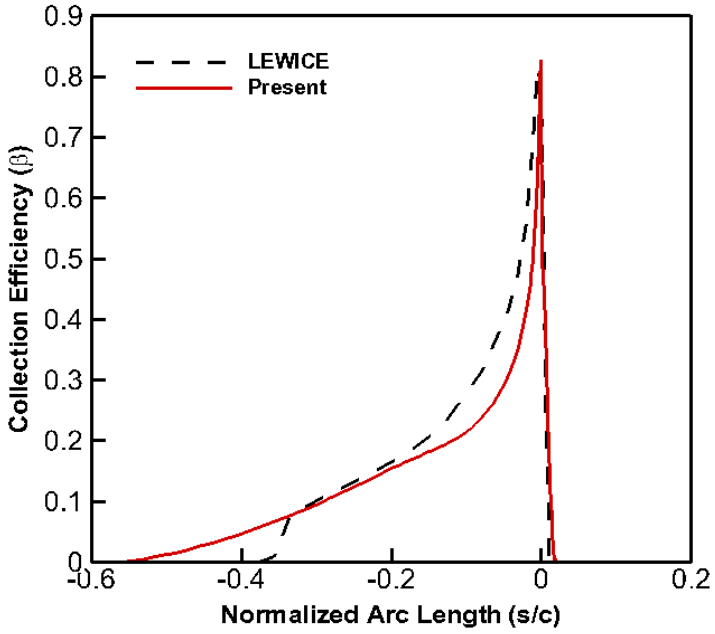

f) AoA = 11 deg.

Figure 3.26: Comparison of Collection Efficiency for an Oscillating SC2110 Airfoil.

3.2.2 3-D Wing case

In an effort to assess the suitability of the present approach for 3-D configurations, collection efficiency simulations have been done for a swept tail made of NACA64A008 sections. This configuration was chosen because of the availability of collection and pressure distributions data at various mean flow conditions, collected over 1997 and 1999 [70]. GENCAS is used to obtain flowfield data. In the CFD simulation, Roe scheme with a 3rd order MUSCL reconstruction is used for flux calculations. 1st order implicit LUSGS scheme is used for marching in time. Spalart-Allmaras (SA) is used as a turbulence model. Figure 3.23 shows 3-D CFD mesh used for simulations. It is a C-H grid with 385 points in the wrap-around direction, 84 points in the spanwise direction, and 69 points in the normal direction. The icing test conditions are given in Table 3.3. The predicted pressure distributions are compared with experimental data in Figure 3.28 and are in good agreement with experiment.

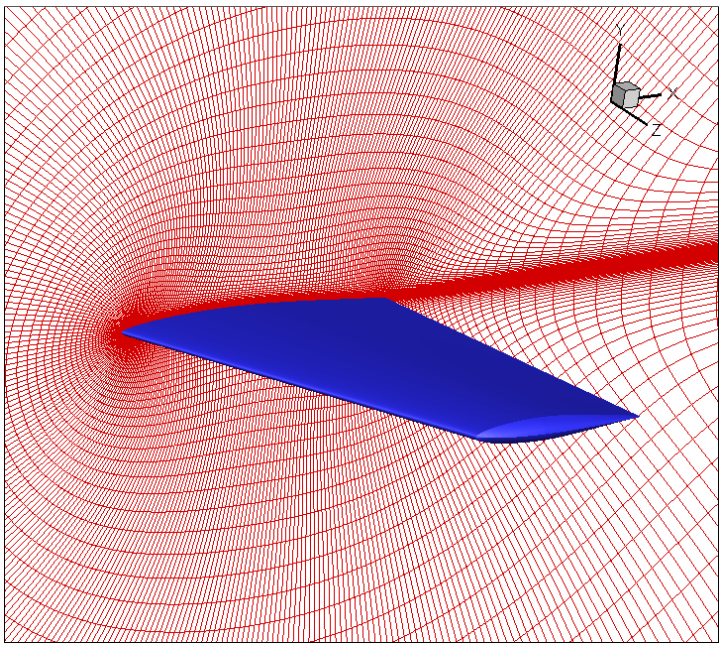

Figure 3.27: 3-D Grid for NACA64A008 Swept Tail Wing [385 x 84 x 69].

Table 3.3: Test Conditions for NACA64A008 Swept Tail

Parameter	Value
U_∞ (m/sec)	78.66
Re (Million)	5.03
AOA (Degree)	0 / 6
MVD (μm)	11.5 / 21.0

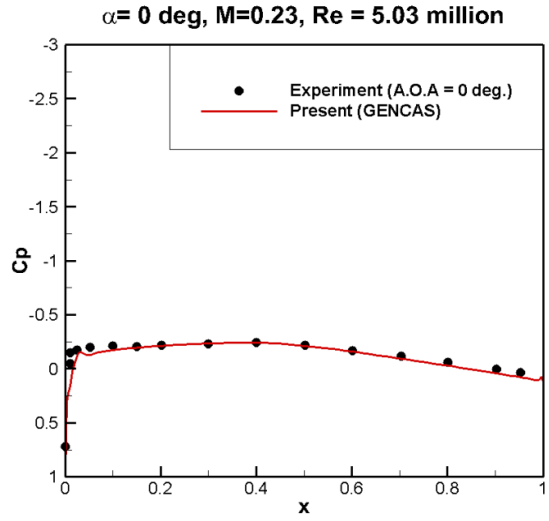

a) AoA = 0 deg.

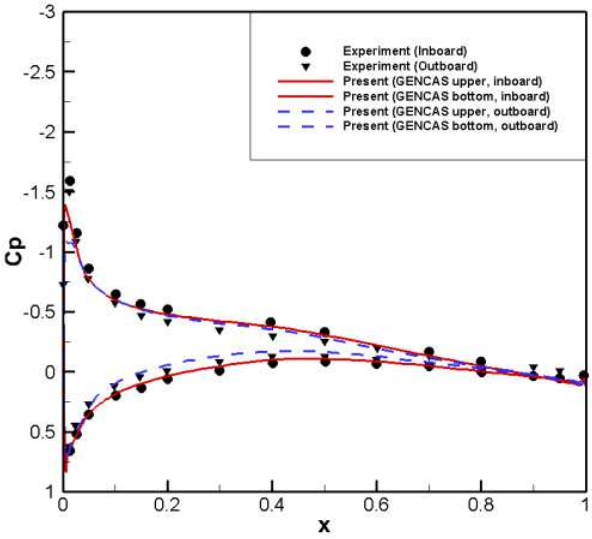

b) AoA = 6 deg.

Figure 3.28: Comparison of Pressure Distribution for NACA64A008 Swept Tail Section.

Figure 3.29 and 3.30 present the comparison of local impingement efficiency distributions between present prediction and measurement according to different value of MVD at 0° and 6°. The x-axis (surface distance) is normalized by airfoil chord length. The positive values correspond to the lower surface of the tail section. The peak value of collection efficiency is found to increase with MVD size. For an angle of attack of 0°, the peak values of collection efficiency are under-predicted. One of reason for this may be due to the first order scheme applied for the convection term of governing equations. High order approximation may improve this. For the high angle of attack case, the location of peak value of collection efficiency was shifted downstream on the lower surface of the airfoil. Simulation results are shifted to the left with respect to the experimental data.

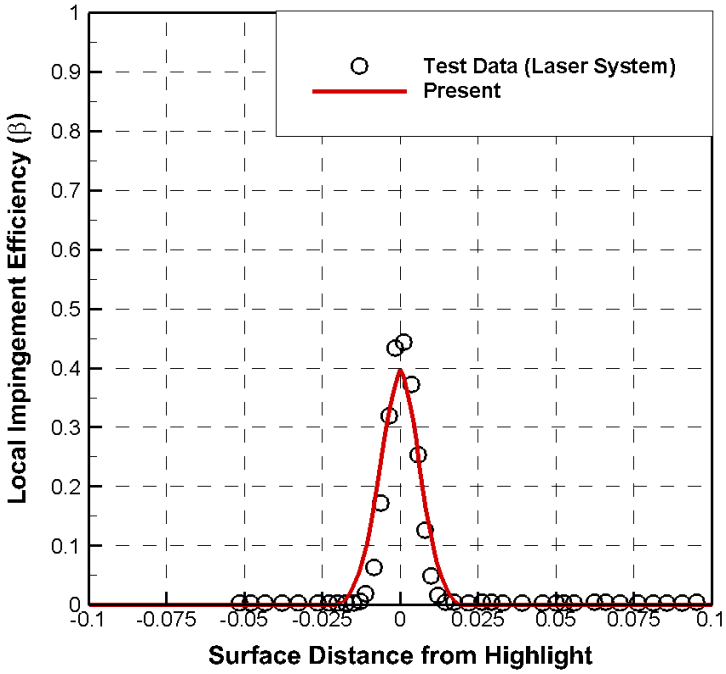

a) MVD=11.5

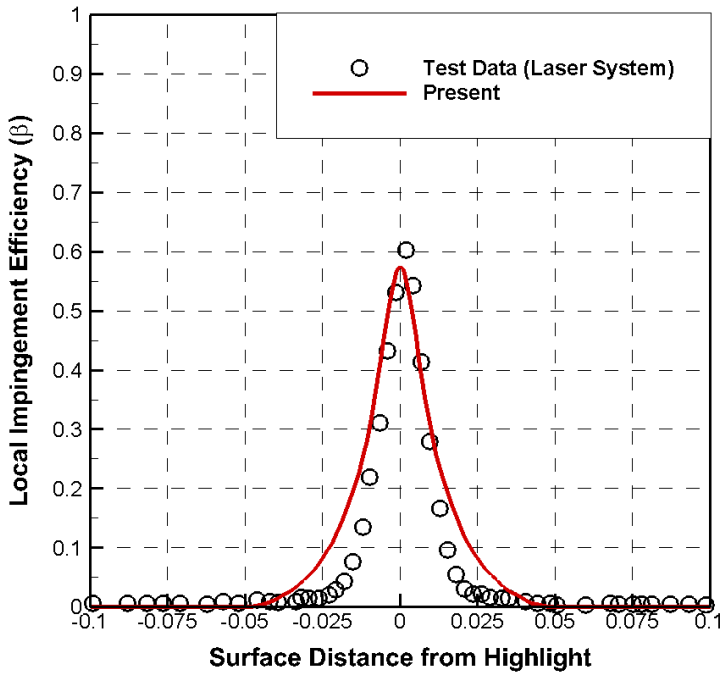

b) MVD=21

Figure 3.29: Comparison of Collection efficiency for NACA64A008 Swept Tail Section at Zero Degrees Angle of Attack.

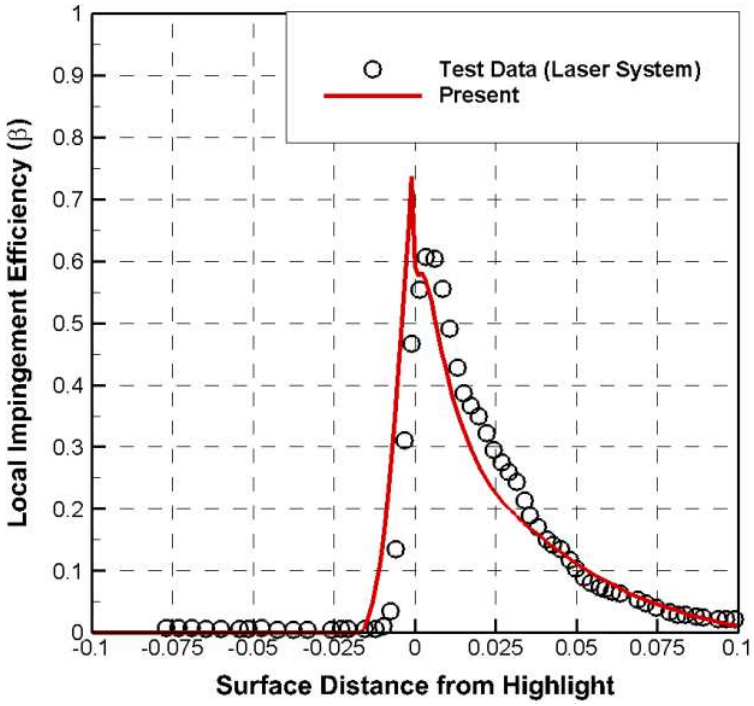

Figure 3.30: Comparison of Collection efficiency for NACA64A008 Swept Tail Section at 6 Degrees Angle of Attack (MVD=21).

3.3 Validation of Ice Accretion Module

In this section, a number of ice accretion simulations are presented to demonstrate the capabilities of developed ice accretion module. Comparisons with industry-standard Lagrangian approaches found in LEWICE are also shown.

3.3.1 Rime Ice

NASA27

In order to validate the ice accretion module, simulation results are compared with experimental ice shape [85] over a NACA0012 airfoil. A specific condition called NASA27 has been modeled using the present suite of tools. Table 3.4 shows the flow conditions, closer to rime ice conditions. GENCAS is used to obtain flow field data. In the CFD simulation, Roe scheme with a 3rd order MUSCL reconstruction is used for flux calculations. A temporally first order implicit LUSGS scheme is used for marching in time. Spalart-Allmaras (SA) is used to compute eddy viscosity distributions. A structured C-type mesh (397 x 101) is used.

During the ice accretion phase of the simulation, a multi-step approach is used with a time step of 120.0 sec. Figure 3.31 shows the computed ice shape. LEWICE means a stand-alone mode simulation. Simulation with the Extended Messinger model uses data from CFD simulation and Eulerian droplet simulation in order to calculate ice growth. While LEWICE shows under-prediction of the maximum ice thickness, Extended Messinger model over-predicted ice thickness near leading edge.

Table 3.4: Test Conditions for NASA27

Parameter	Value
Air speed (m/sec)	58.1
Angle of Attack (Deg.)	4.0
LWC (g/m^3)	1.3
MVD (μm)	20
Temperature (K)	245.35
Time (min)	6
Chord (m)	0.53

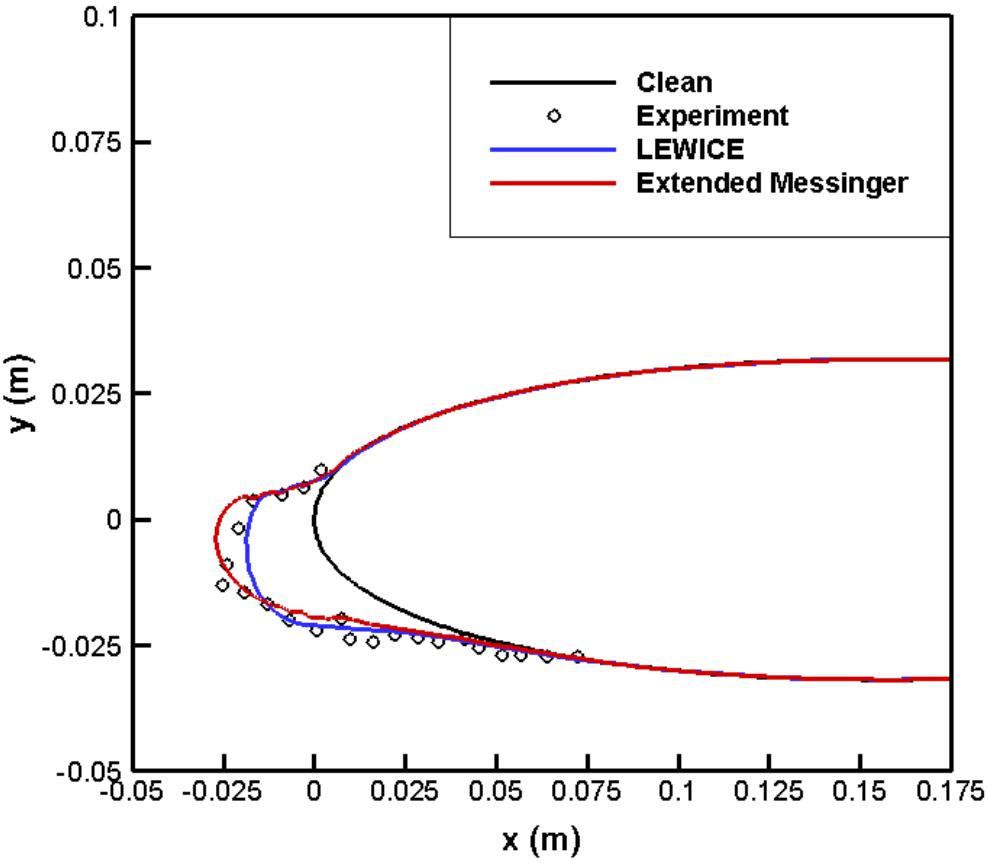

Figure 3.31: Predicted Ice Shape for NACA0012 (NASA27).

Run404

As a second validation, ice accretion simulations have been done for a specific condition called Run404. Present results are compared to numerical results obtained with LEWICE and experimental results [86]. Table 3.5 shows the flow conditions, closer to rime ice conditions. GENCAS is used to obtain flow field data. In the CFD simulation, sane solver options used in NASA27case are used.. A structured C-type mesh (483 x 121) is used.

During the ice accretion phase of the simulation, a multi-step approach is used with a time step of 60.0 sec. Figure 3.32 shows the computed ice shape. Three different simulations are performed. LEWICE means a stand-alone mode simulation (case 1). The other two cases use data from CFD simulation and Eulerian droplet simulation in order to calculate ice growth. LEWICE (case 2) and ice accretion code using the extended Messinger model (case 3) are used. Case 1 shows lower ice thickness on the upper part of the airfoil. Case 2 and 3 predict almost identical limits of impact and match the experiments on the suction side of the airfoil. Ice thickness,however, are under-predicted by both codes on the pressure side of the airfoil. Case 1 and 2 match the experiment near leading edge. While case 3 predicted ice thickness on the upper part of the airfoil fairly well, ice thickness near leading edge is over-predicted.

Table 3.5: Test Conditions for Run404

Parameter	Value
Air speed (m/sec)	102.8
Angle of Attack (Deg.)	3.2
LWC (g/m^3)	0.55
MVD (μm)	20
Temperature (K)	256.49
Time (min)	7
Chord (in)	21

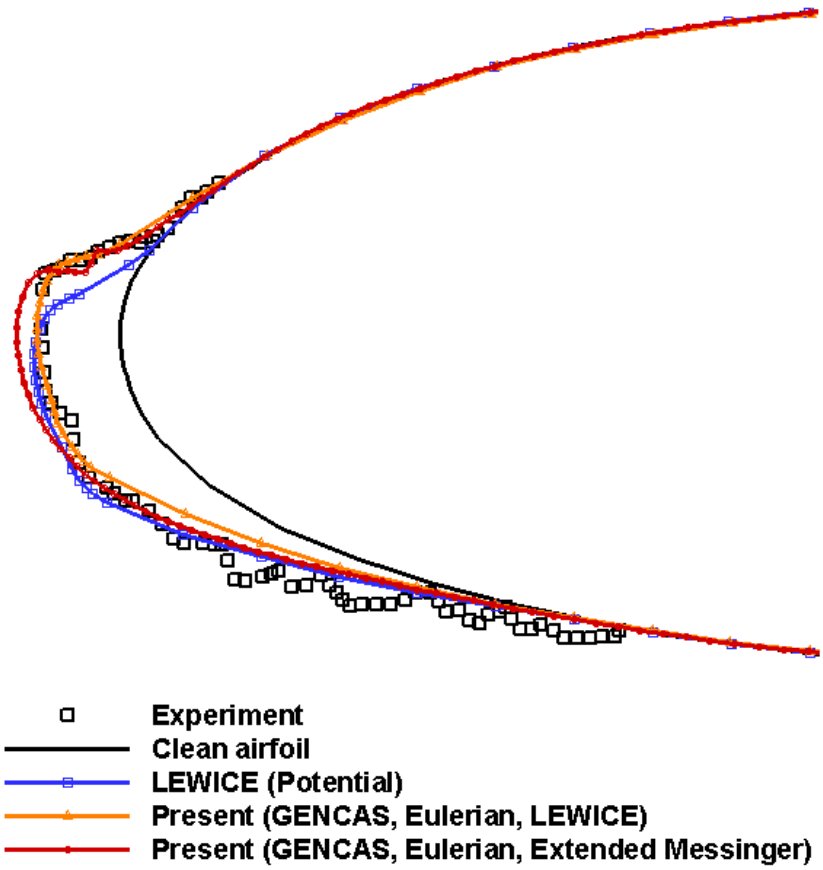

Figure 3.32: Predicted Ice Shape for NACA0012 (Run404).

Ice Accretion for Model Rotor Icing

Ice growth simulations have been done for a model rotor blade [20] tested in NASA Lewis Icing Research Tunnel (IRT). The model rotor blade is designed and built by McDonnell Douglas Helicopter Company using molds which were constructed by Sikorsky Aircraft. The rotor radius is 3 ft, chord length is 4.9 in, and has rectangular blade with NACA0012 airfoil with -10 deg. of linear twist.

A similar averaging technique used in Ref. 20 is employed in the present study. Korkan [87] developed a technique which simplified analysis of a helicopter main rotor in forward flight with a rime ice accretion. In current simulations, The local angle of attack at the radial location of interest was averaged azimuthally. The local velocity is taken to be the rotational velocity at the specified radial location. This is, in effect, the averaged velocity. These averaged quantities are used as inputs for ice accretion simulation.

Ice accretion simulations have been done for a specific condition called Run34. Present results are compared to numerical results obtained with LEWICE and experimental results from Ref. 20 and icing test at the Penn State University. For same icing conditions, wind tunnel tests have been done in the Adverse Environment Rotor Test Stand Facility (AERTS) at the Penn State University. Table 3.6 shows the flow conditions, closer to rime ice conditions. GENCAS is used to obtain flow field data. In the CFD simulation, Roe scheme with a 3rd order MUSCL reconstruction is used for flux calculations. A temporally first order implicit LUSGS scheme is used for marching in time. Spalart-Allmaras (SA) is used to compute eddy viscosity distributions. A structured C-type mesh (483 x 121) is used.

During the ice accretion phase of the simulation, a single-step approach is used due to the relatively short spray time. Figure 3.33 shows the computed ice shape. Three different simulations are performed. LEWICE means a stand-alone mode simulation (case 1). The other two cases use data from CFD simulation and Eulerian droplet

simulation in order to calculate ice growth. LEWICE (case 2) and ice accretion code using the extended Messinger model (case 3) are used. All simulations show an under-prediction of ice thickness near stagnation point. All simulations predict almost identical limits of impact and match the experiments on the suction side of the airfoil. Ice thickness , however, is under-predicted by both codes on the pressure side of the airfoil. The limits of impact is over-predicted on the lower surface of the airfoil.

Ice accretion simulations have been done for an another condition called Run41. Present results are compared to numerical results obtained with LEWICE and experimental results from Ref. 20 and icing test at the Penn State University. Table 3.7 shows the flow conditions, closer to rime ice conditions. GENCAS is used to obtain flow field data. Same size of mesh (483 x 121) and CFD solver options used in Run 34 case are used.

During the ice accretion phase of the simulation, a multi-step approach is used with a time step of 35.0 sec. Figure 3.34 shows the computed ice shape. Three different simulations are performed. LEWICE means a stand-alone mode simulation (case 1). The other two cases use data from CFD simulation and Eulerian droplet simulation in order to calculate ice growth. LEWICE (case 2) and ice accretion code using the extended Messinger model (case 3) are used. Case 1 and case 2 show an under-prediction of ice thickness near stagnation point. Case 3 matches the experiments fairly well near stagnation point. As seen in Run34 cases, all simulations predict almost identical limits of impact and match the experiments on the upper side of the airfoil. Ice thickness is captured well by both codes on the pressure side of the airfoil. However, the limits of impact is over-predicted on the lower surface of the airfoil.

Table 3.6: Test Conditions for Run34

Parameter	Value
Air speed (m/sec)	65.4
Angle of Attack (Deg.)	3.7
LWC (g/m^3)	0.46
MVD (μm)	28
Temperature (K)	258.45
Time (sec)	44
Chord (in)	4.9

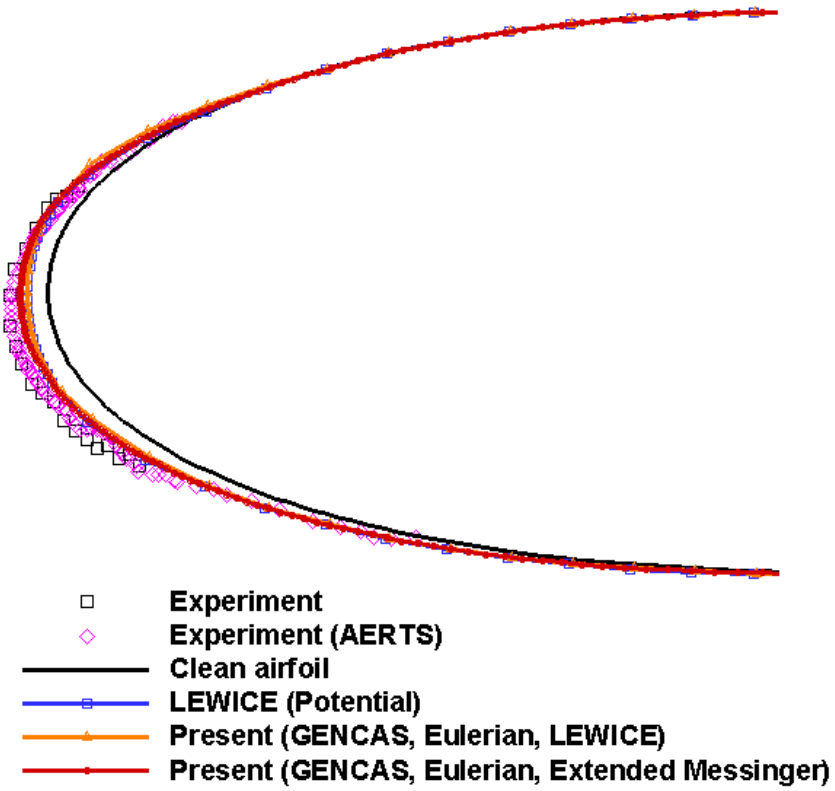

Figure 3.33: Predicted Ice Shape for a Model Rotor (Run34).

Table 3.7: Test Conditions for Run41

Parameter	Value
Air speed (m/sec)	56.2
Angle of Attack (Deg.)	3.5
LWC (g/m^3)	0.44
MVD (μm)	28
Temperature (K)	257.75
Time (sec)	70
Chord (in)	4.9

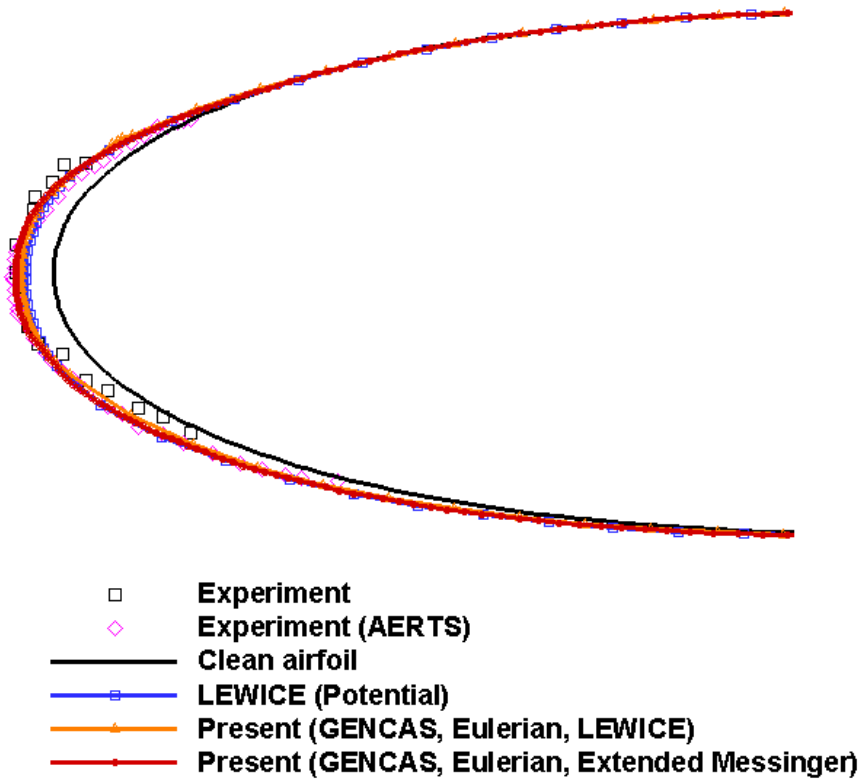

Figure 3.34: Predicted Ice Shape for a Model Rotor (Run41).

3.3.2 Glaze Ice

In this section, several ice accretion simulations are presented with the classical and extended Messinger models for glaze ice accretion. Because all of the impinging water do not freeze and the remaining water runs aft along the surface and freeze somewhat downstream, ice growth process is complex. Further understanding and improvement for this glaze ice accretion are still required.

NASA30

In order to validate the ice accretion module, simulation results are compared with experimental ice shape [85] over a NACA0012 airfoil. A specific condition called NASA30 has been modeled using the present suite of tools. Table 3.8 shows the flow conditions, closer to glaze ice conditions. The flow conditions are same with NASA27 (rime ice) except temperature. GENCAS is used to obtain flow field data. In the CFD simulation, Roe scheme with a 3rd order MUSCL reconstruction is used for flux calculations. A temporally first order implicit LUSGS scheme is used for marching in time. Spalart-Allmaras (SA) is used to compute eddy viscosity distributions. A structured C-type mesh (397 x 101) is used.

During the ice accretion phase of the simulation, a multi-step approach is used with a time step of 120.0 sec. Figure 3.35 shows the computed ice shape. LEWICE means a stand-alone mode simulation. Simulation with the Extended Messinger model uses data from CFD simulation and Eulerian droplet simulation in order to calculate ice growth. LEWICE shows under-prediction of the maximum ice thickness and the location of upper horn is shifted to downstream. While the Extended Messinger model predicted ice thickness near leading edge fairly well, the location of upper horn is shifted to upstream.

Table 3.8: Test Conditions for NASA30

Parameter	Value
Air speed (m/sec)	58.1
Angle of Attack (Deg.)	4.0
LWC (g/m^3)	1.3
MVD (μm)	20
Temperature (K)	289.85
Time (min)	6
Chord (m)	0.53

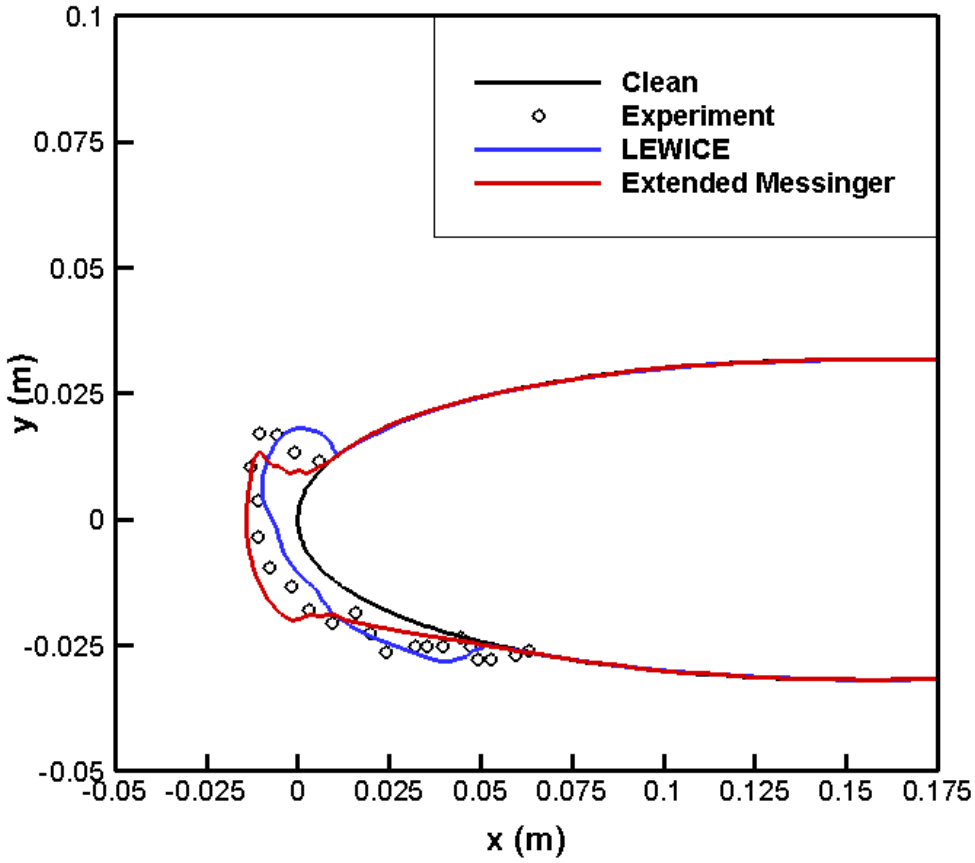

Figure 3.35: Predicted Ice Shape for NACA0012 (NASA30).

Run308

Reference 86 contains a rich set of validation data for ice accretion over a NACA0012 airfoil. A specific condition called runs 308 has been modeled using the present suite of tools. Table 3.9 shows the flow conditions, closer to glaze ice conditions. GENCAS is used to obtain flow field data. In the CFD simulation, Roe scheme with a 3rd order MUSCL reconstruction is used for flux calculations. A temporally first order implicit LUSGS scheme is used for marching in time. Spalart-Allmaras (SA) is used to compute eddy viscosity distributions. A structured C-type mesh (397 x 101) is used.

During the ice accretion phase of the simulation, a multi-step approach is used with a time step of 57.75 sec. Figure 3.36 shows the computed ice shape. Three different simulations are performed. LEWICE means a stand-alone mode simulation (case 1). The other two cases use data from CFD simulation and Eulerian droplet simulation in order to calculate ice growth. LEWICE (case 2) and ice accretion code using the extended Messinger model (case 3) are used. All simulations show an under-prediction of the horn shape formed over the upper part of the airfoil. Although case 1 and 2 show good agreement near the stagnation point, the location of upper horn is shifted to downstream. While case 3 predicted the location of upper horn fairly well, ice thickness near leading edge is over-predicted.

Table 3.9: Test Conditions for Run308

Parameter	Value
Air speed (m/sec)	102.8
Angle of Attack (Deg.)	3.5
LWC (g/m^3)	1.0
MVD (μm)	20
Temperature (K)	262.04
Time (min)	3.85
Chord (m)	0.5334

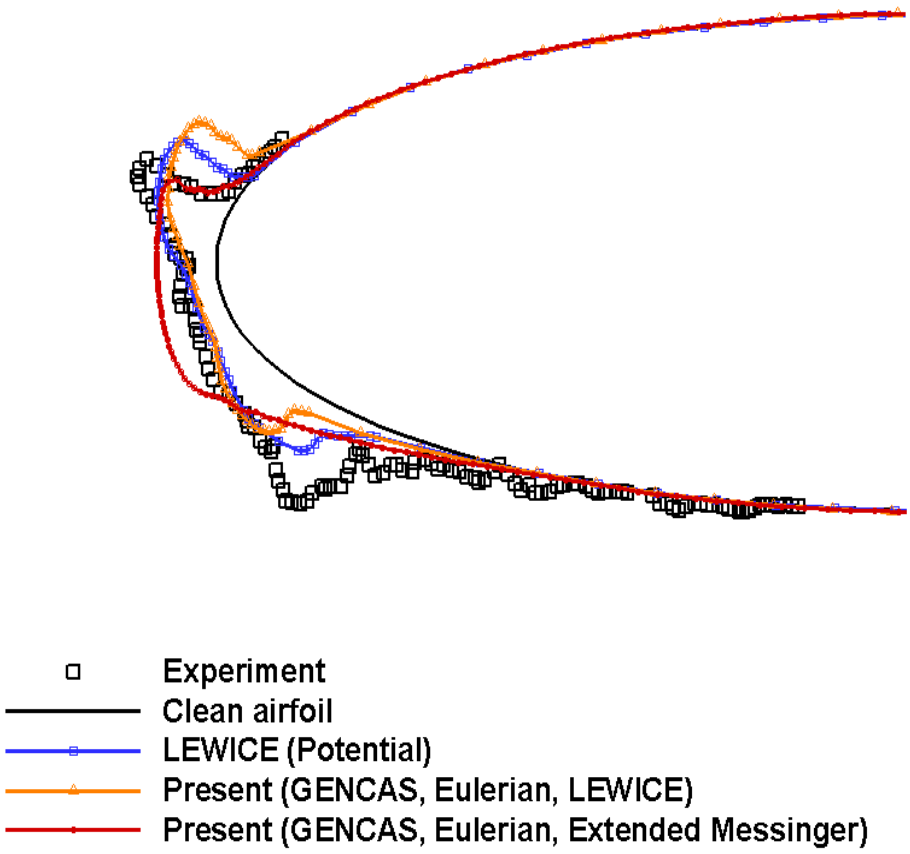

Figure 3.36: Predicted Ice Shape for NACA0012 (Run308).

Business Jet Airfoil

Ice accretion with a business jet airfoil with scaled chord also has been modeled using the present suite of tools. Table 3.10 shows the flow conditions, closer to glaze ice conditions. GENCAS is used to obtain flow field data. Same size of mesh (397 x 101) and CFD solver options used in Run 308 case are used. During the ice accretion phase of the simulation, a multi-step approach is used with a time step of 13.2 sec. Geometry smoothing is applied for CFD simulation.

Figure 3.37 shows the computed ice shape. Three different simulations are performed. LEWICE means a stand-alone mode simulation (case 1). The other two cases use data from CFD simulation and Eulerian droplet simulation in order to calculate ice growth. LEWICE (case 2) and ice accretion code using the extended Messinger model (case 3) are used. Case 3 predicted the location and thickness of upper and lower horn fairly well.

Table 3.10: Test Conditions for a Business Jet Airfoil

Parameter	Value
Air speed (m/sec)	136.86
Angle of Attack (Deg.)	0
LWC (g/m^3)	1.42
MVD (μm)	27.3
Temperature (K)	252.4
Time (sec)	66
Chord (m)	0.3048

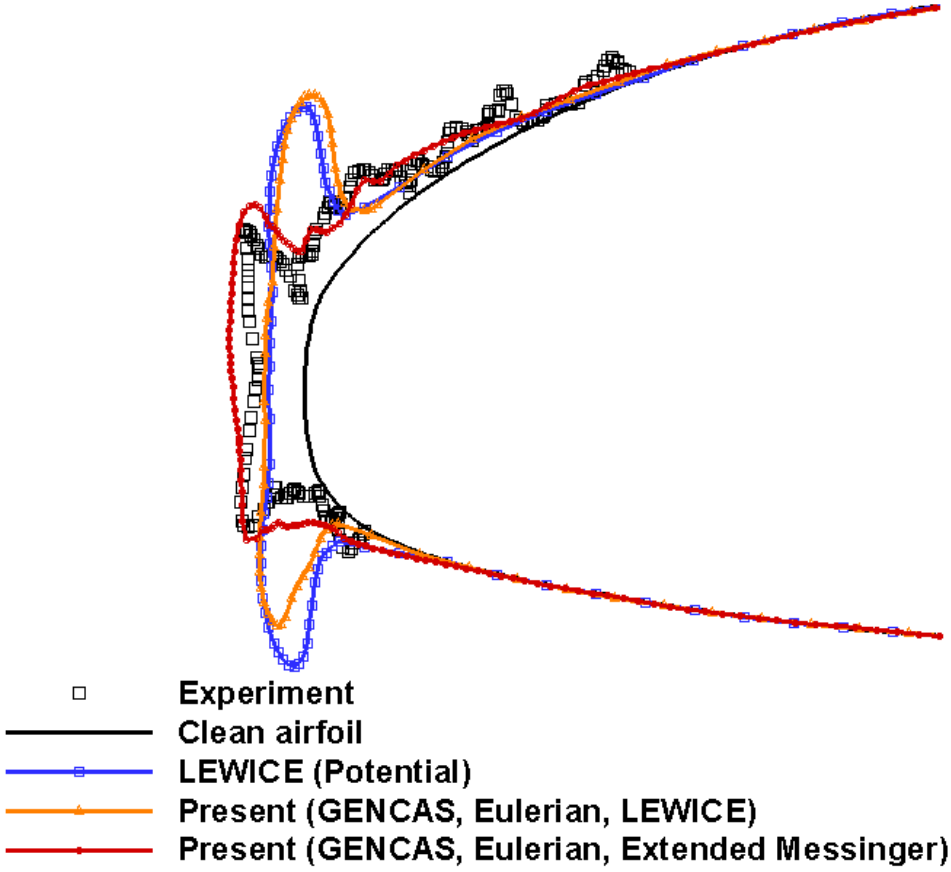

Figure 3.37: Predicted Ice Shape for Business Jet Airfoil.

Arnold Engineering Development Center (AEDC) case5

Reference 88 contains several validation data for ice accretion over a NACA0012 airfoil. One of conditions called case5 has been modeled using the present suite of tools. Table 3.11 shows the flow conditions, closer to glaze ice conditions. For same icing conditions, wind tunnel tests also have been done in the Adverse Environment Rotor Test Stand Facility (AERTS) at the Penn State University. GENCAS is used to obtain flow field data. Same size of mesh (397 x 101) and CFD solver options used in Run 308 case are used.

During the ice accretion phase of the simulation, a multi-step approach is used with a time step of 60 sec. Figure 3.38 shows the computed ice shape. Three different simulations are performed. LEWICE means a stand-alone mode simulation (case 1). The other two cases use data from CFD simulation and Eulerian droplet simulation in order to calculate ice growth. LEWICE (case 2) and ice accretion code using the extended Messinger model (case 3) are used. Case 1 and case 2 show similar ice shape. The maximum ice thickness at leading edge is under-predicted. Case 3 (ice accretion code using the Extended Messinger model) shows a quite different ice shape compared to LEWICE and the maximum ice thickness at leading edge is over-predicted.

Table 3.11: Test Conditions for a AEDC case5

Parameter	Value
Air speed (m/sec)	67.1
Angle of Attack (Deg.)	0
LWC (g/m^3)	0.92
MVD (μm)	26
Temperature (K)	262.05
Time (min)	4
Chord (m)	0.267
Scaling	Yes (1/2)

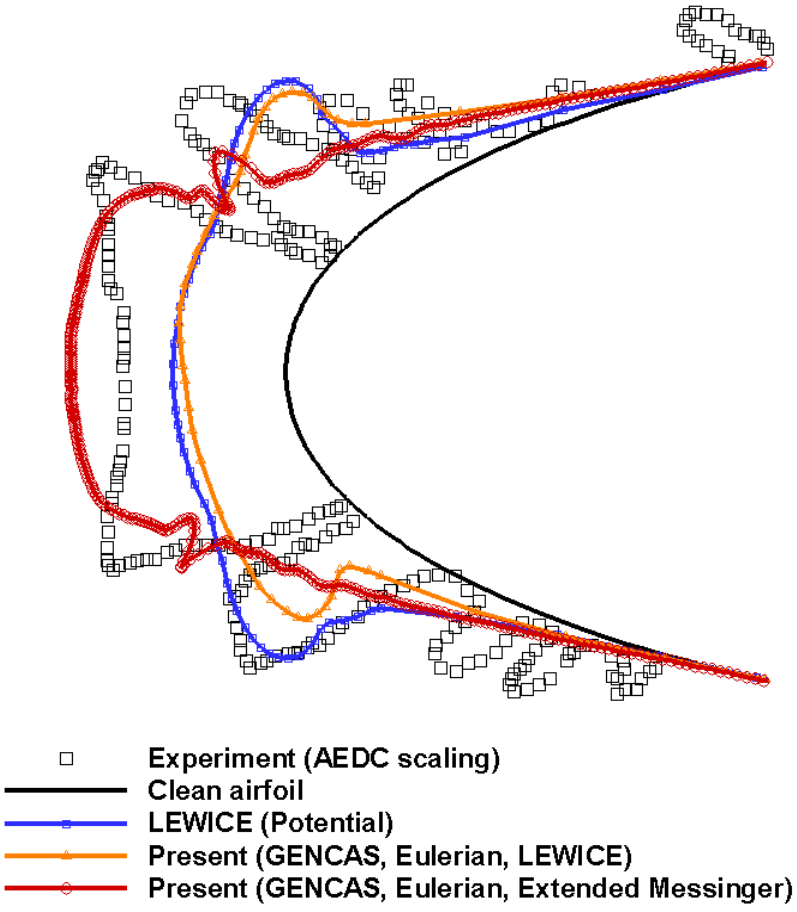

Figure 3.38: Predicted Ice Shape for AEDC Case5.

112Feo

Reference 89 contains several validation data for ice accretion over a NACA0012 airfoil. One of conditions called 112Feo has been modeled using the present suite of tools. Table 3.12 shows the flow conditions, closer to glaze ice conditions. For same icing conditions, wind tunnel tests also have been done in the Adverse Environment Rotor Test Stand Facility (AERTS) at the Penn State University. GENCAS is used to obtain flow field data. Same size of mesh (397 x 101) and CFD solver options used in Run 308 case are used.

During the ice accretion phase of the simulation, a multi-step approach is used with a time step of 60 sec. Figure 3.39 shows the computed ice shape. Three different simulations are performed. LEWICE means a stand-alone mode simulation (case 1). The other two cases use data from CFD simulation and Eulerian droplet simulation in order to calculate ice growth. LEWICE (case 2) and ice accretion code using the extended Messinger model (case 3) are used. Case 1 and case 2 show similar ice shape as seen in AEDC case 5. The maximum ice thickness at leading edge is also under-predicted. Case 3 shows a quite different ice shape compared to LEWICE and the maximum ice thickness at leading edge is over-predicted.

Table 3.12: Test Conditions for a 112Feo

Parameter	Value
Air speed (m/sec)	56.9
Angle of Attack (Deg.)	0
LWC (g/m^3)	0.96
MVD (μm)	27
Temperature (K)	264.95
Time (min)	4.2
Chord (m)	0.267
Scaling	No

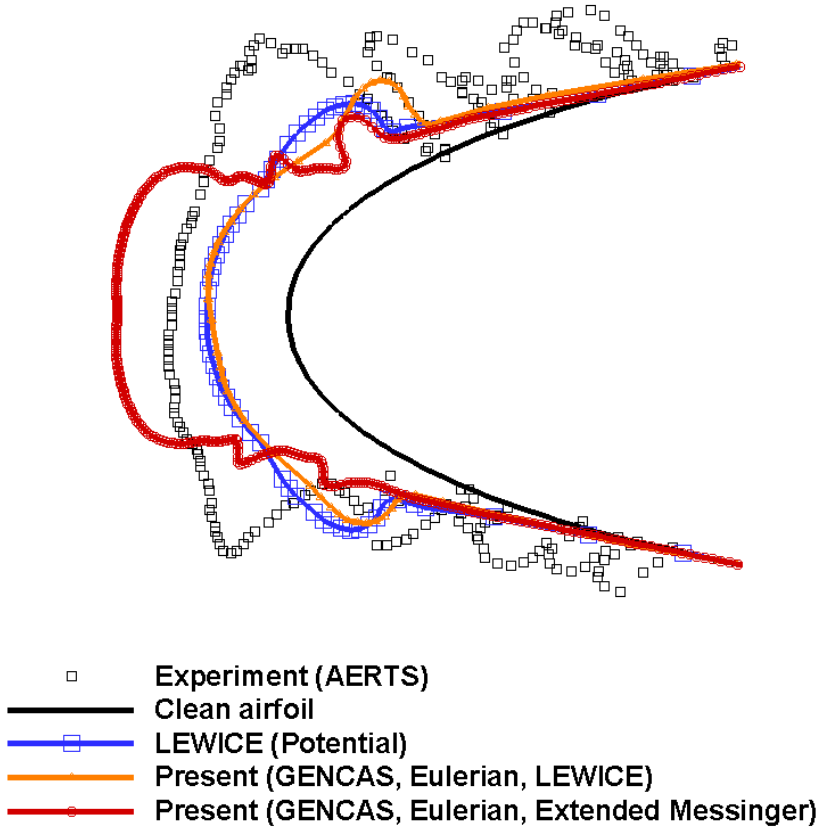

Figure 3.39: Predicted Ice Shape for 112Feo.

CHAPTER 4

NUMERICAL SIMULATION OF ICE ACCRETION ON 3-D ROTOR BLADE

In this section, selected results of numerical and experimental studies for rotorcraft icing phenomena are presented. Extensive rotor blade ice tests have been done in NASA Glenn's Icing Research Tunnel (IRT) in September 2013 [90-92]. In the present study, ice growth simulations have been performed for some of the numerous test conditions.

The model rotor is a production of Bell Helicopter Model 206B tail rotor blade with heater blankets bonded to the blade surface. The rotor is a two-bladed teetering rotor with a δ3 of 45°. The rotor radius is 32.6", a chord of 5.3" and has rectangular blade with NACA0012 airfoil.

4.1 Coupled CFD/Flapping Dynamics Analysis

In current study, the blade motion (flapping angle) is obtained from the coupled CFD / Flapping Dynamics analysis for clean rotor. Flapping angles of blade are estimated after every coupled CFD iteration until the hub roll and pitching moments are removed. Initial blade motion is estimated analytically by using harmonic balance approach.

Figure 4.1 shows flowchart of the CFD / Flapping Dynamics analysis. The process is represented by the following steps:

1. Perform classical linear aerodynamics calculations. Estimate initial β_0, β_{1c} and β_{1s} from harmonic balance approach. Use the estimates of flapping angles to create a blade motion file for CFD analysis.
2. Perform CFD analysis (Iteration-0). Obtain sectional lift L'_{CFD} as a function of azimuth and radial location. Typically, CFD solvers normally save C_nM^2. Thus, L' is simply $\frac{1}{2} * r * c * a_\infty^2 * C_nM^2$.

3. Compute the pitching and rolling moments at the hub using the CFD data. It will have the units of force times distance, e.g. lbf.ft.
4. If the flapping angles are exact, the hub moments would be zero.
   - In reality, when the CFD airloads are fed into the moment terms on the right hand side of the flapping dynamics equations, the hub moments (or the sin and cosine components) won't go to zero since the flapping dynamics is based on linear aerodynamics. We need to correct β_{1c} and β_{1s} to account for the imbalance in the rolling and pitching moments at the hub that the use of CFD has produced.
5. Expand the azimuthally averaged $M_{rolling}$ and $M_{pitching}$ at the hub, which are functions of β_{1c} and β_{1s} about the current best estimates for these two quantities, plus a 'delta' quantity.

$$\begin{aligned} M_{Rolling}(\beta_{1c},\beta_{1s}) &= M_{Rolling}\left(\beta_{1c}^{current\_guess}+\Delta\beta,\beta_{1c}^{current\_guess}+\Delta\beta\right)=0 \\ M_{Pitch}(\beta_{1c},\beta_{1s}) &= M_{Pitch}\left(\beta_{1c}^{current\_guess}+\Delta\beta,\beta_{1c}^{current\_guess}+\Delta\beta\right)=0 \end{aligned} \tag{4.1}$$

6. Expand the above two equations about the current guess for b_{1c} and b_{1s}. The equation below may be inverted to get $\Delta\beta_{1c}$ and $\Delta\beta_{1s}$.

$$\begin{bmatrix} \frac{\partial M_{roll}}{\partial \beta_{1c}} & \frac{\partial M_{roll}}{\partial \beta s} \\ \frac{\partial M_{pitch}}{\partial \beta_{1c}} & \frac{\partial M_{Pitchl}}{\partial \beta s} \end{bmatrix} \begin{Bmatrix} \Delta\beta_{1c} \\ \Delta\beta_{1s} \end{Bmatrix} = -\begin{Bmatrix} M_{roll} \\ M_{pitch} \end{Bmatrix}_{CFD} \tag{4.2}$$

where,

$$\begin{aligned} \frac{\partial M_{roll}}{\partial \beta_{1c}} &= -\gamma I\Omega^2\left[-2+\mu^2\right]/32 \\ \frac{\partial M_{roll}}{\partial \beta_{1s}} &= -\gamma I\Omega^2\left[2+3\mu^2\right]/32 \\ \frac{\partial M_{pitch}}{\partial \beta_{1c}} &= \gamma I\Omega^2\left[2+\mu^2\right]/32 \\ \frac{\partial M_{pitch}}{\partial \beta_{1s}} &= \gamma I\Omega^2\left[2+\mu^2\right]/32 \end{aligned}$$

I = single blade moment of inertia,

Ω = angular velocity in radians/sec

7. We add the $\Delta\beta_{1c}$ and $\Delta\beta_{1s}$ to our most recent estimates of β_{1c} and β_{1s}.
8. Repeat steps 3-7 until the hub roll and pitching moments all go to zero.

Blade motion for clean rotor is used in the subsequent ice accretion and iced rotor performance prediction analyses.

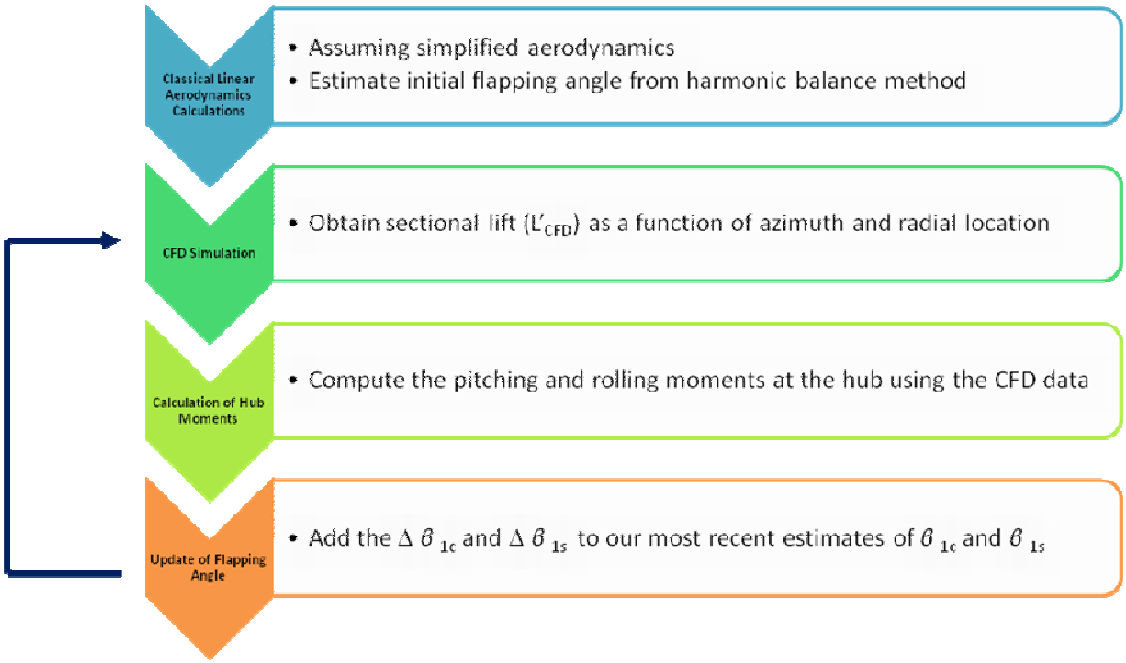

Figure 4.1 Flowchart of the CFD / Flapping Dynamics Analysis.

4.2 Clean Rotor Performance Prediction

Before the ice accretion simulation, performance predictions for clean rotor (called Run84) have been done to validate the Coupled CFD / Flapping Dynamics method. Run 84 [90-92] represents a dry air test for a sweep of collective pitch angles 0°, 2°, 5°, 8°, and 10° with each angle sustained for around 20 seconds. The tunnel was run at an ambient temperature of -10° C (14° F) and 60 kts. The blade motion (flapping angle) is computed from a coupled CFD / Flapping Dynamics analysis of the clean rotor.

Figure 4.2 shows 3-D CFD grids used for simulations. A C-H grid with 131 points in the wrap-around direction, 70 radial grid points on the blade, and 45 points in the normal direction was additionally generated using an in-house grid generator. For solutions presented in this paper, the Roe upwind, third order accurate scheme with the Spalart-Allmaras Detached Eddy Simulation (SA-DES) turbulence model is used. The predicted thrust and power are compared with measured values in Figure 4.3. While the predicted results are not exactly equivalent to the experiment, the consistent trend in thrust and power validates the Coupled CFD / Flapping Dynamics method.

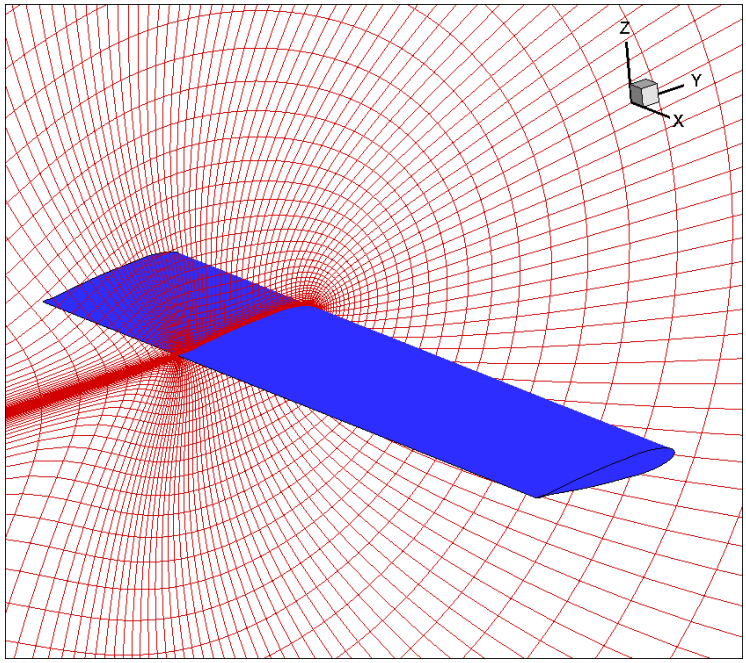

Figure 4.2: Bell Tail Rotor Blade Grid System (131 x 70 x 45).

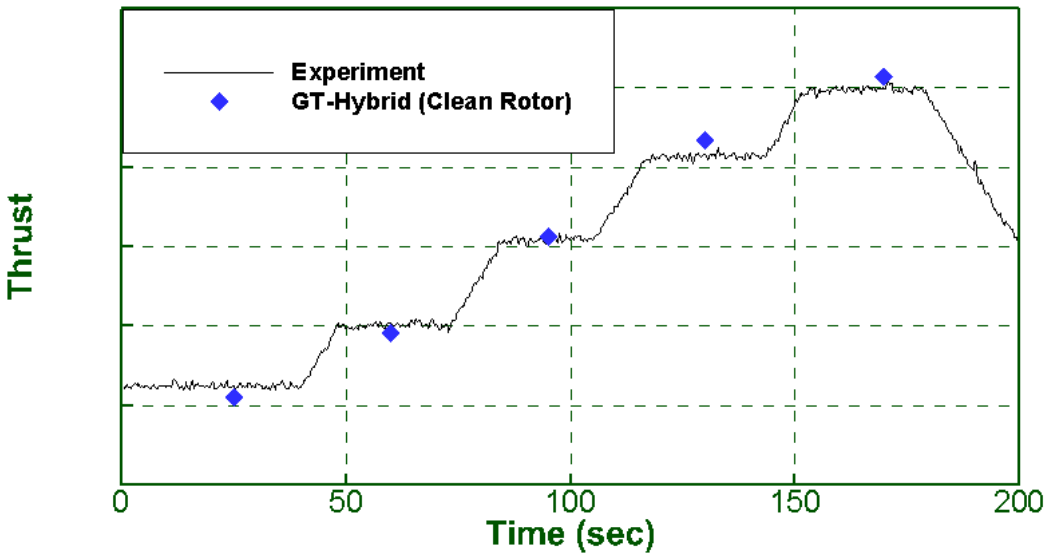

a) Thrust

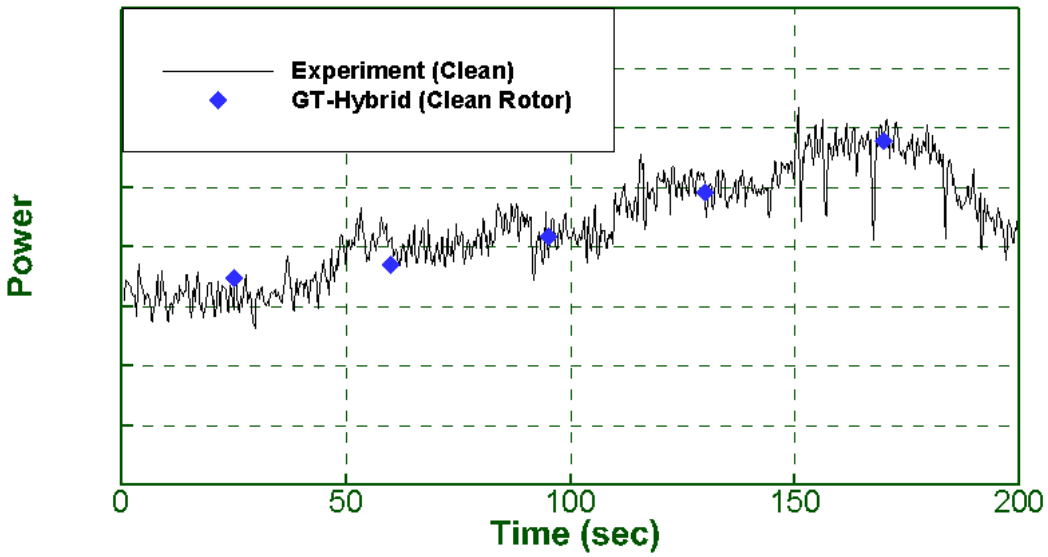

b) Power

Figure 4.3: Comparison of Clean Rotor Performance (Run84).

4.3 Ice Shape Prediction

4.3.1 Hover

Ice accretion tests for hovering rotor have been done in the Adverse Environment Rotor Test Stand Facility at the Penn State University [93]. Figure 4.4 shows the Adverse Environment Rotor Test Stand Facility (AERTS) and example of ice accretion shape. The accreted ice shapes formed on truncated helicopter rotor blades were hand traced at multiple locations along the span of the rotor. At the tip of the blades, ice shapes were photographed and digitized.

Ice growth simulations have been performed for one of the test conditions, called Test4. Table 4.1 shows the corresponding test conditions. The rotor tested in the Penn State facility is a two-bladed teetering rotor. The rotor has a rectangular planform, and is made of NACA 0015 airfoil sections. The radius is 46", and the chord is 6.8”.

A C-H grid, 131 (chordwise) x 70(spanwise) x 45 (normal), was used for flow field prediction. The predicted flow field solutions from GT-Hybrid were fed into the present Eulerian droplet model and the ice accretion is subsequently computed. Figure 4.5 shows the comparison of predicted ice shape using the Extended Messinger model at the blade tip. The Extended Messinger model did a reasonably good job of predicting the ice shape at the nose, but the ice was thicker than expected downstream of the nose region.

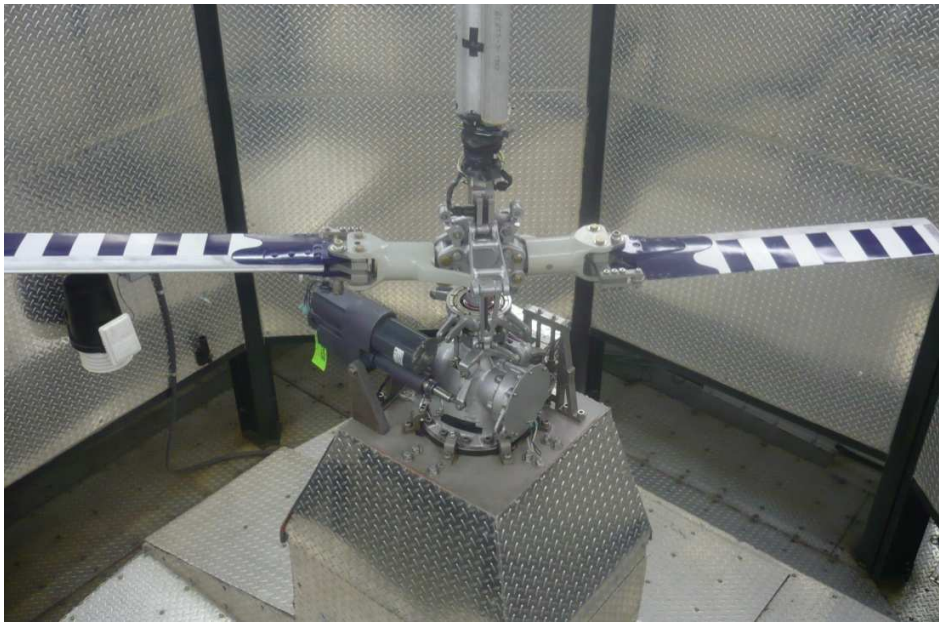

a) AERTS Configuration

b) Ice shape on Rotor Blade

Figure 4.4: Photograph of AERTS Facility and Example of Ice Accretion Shape.

Table 4.1: Test Conditions for Test4 (AERTS at Penn State)

Parameter	Value
Flight condition	Hover
Collective (Deg.)	0
LWC (g/m^3)	2.5
MVD (μm)	20
Temperature (K)	263.15
Time (min)	1

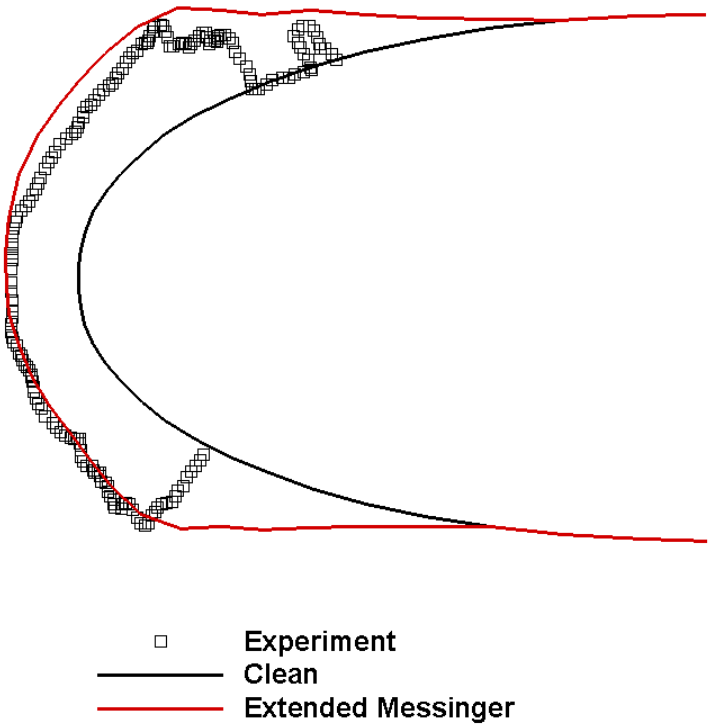

Figure 4.5: Comparisons of Ice Shape for Test4 (AERTS at Penn State).

4.3.2 Forward Flight

Run53

Extensive rotor blade ice tests have been done in NASA Glenn's Icing Research Tunnel (IRT) in September 2013 [90-92]. One of test conditions, Run53, is selected as a baseline case. Table 4.2 shows the corresponding test conditions. The blade motion (flapping angle) is computed from a coupled CFD / Flapping Dynamics analysis of the clean rotor. Comparison of blade motion for Run53 with experiment is seen in Figure 4.6. The maximum difference between predicted and measurement is within 1 degree.

The predicted flow field solutions from CFD simulation (GT-Hybrid) were fed into an Eulerian droplet model and the two ice accretion codes in order to get the ice shape. A multi-step approach is used with a time step of 45 sec. The ice was accreted at four different azimuthal locations (Ψ = 0°, 90°, 180°, 270°). Unsteady flow field data for the clean rotor was used to compute the collection efficiencies at each azimuthal location. Figure 4.7 through 4.8 shows predicted ice shape from both approaches at the selected radial locations 37% R, 50% R, 61% R, 74% R, and 86% R, and 98% R. Ice shapes predicted from both approach are smooth and rounded. Marginal difference in ice shape is seen at the inboard between LEWICE and Extended Messinger model. Predicted ice shapes from both approaches are close to experimental ice shape at the inboard region. Ice shapes start to differ towards blade tip. The Extended Messinger model predicts thicker ice near the leading edge of airfoil. The predicted maximum ice thickness from the Extended Messinger model is closer to experiment. The effect of time step was investigated. Figure 4.9 shows predicted ice shape from 8 time steps. Eight data exchanges were made between GT-Hybrid and Extended Messinger model when predicting the ice growth. Marginal difference is seen for the predicted ice shapes compared to those predicted from 4 time step case.

Table 4.2: Test Conditions for Run53 (NASA Glenn's IRT)

Parameter	Value
Forward Velocity (knot)	60
RPM	1200
Collective (Deg.)	2
LWC (g/m^3)	0.5
MVD (μm)	15
Temperature (K)	263.15
Time (min)	3

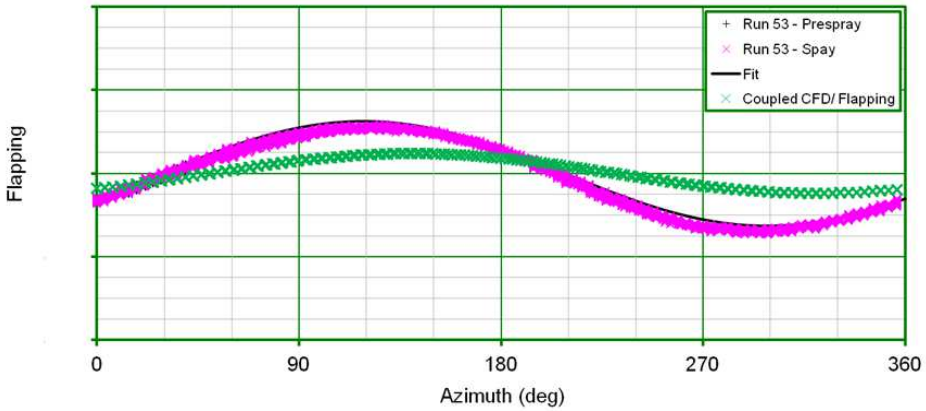

Figure 4.6: Comparison of Blade Flapping Angle for Run 53.

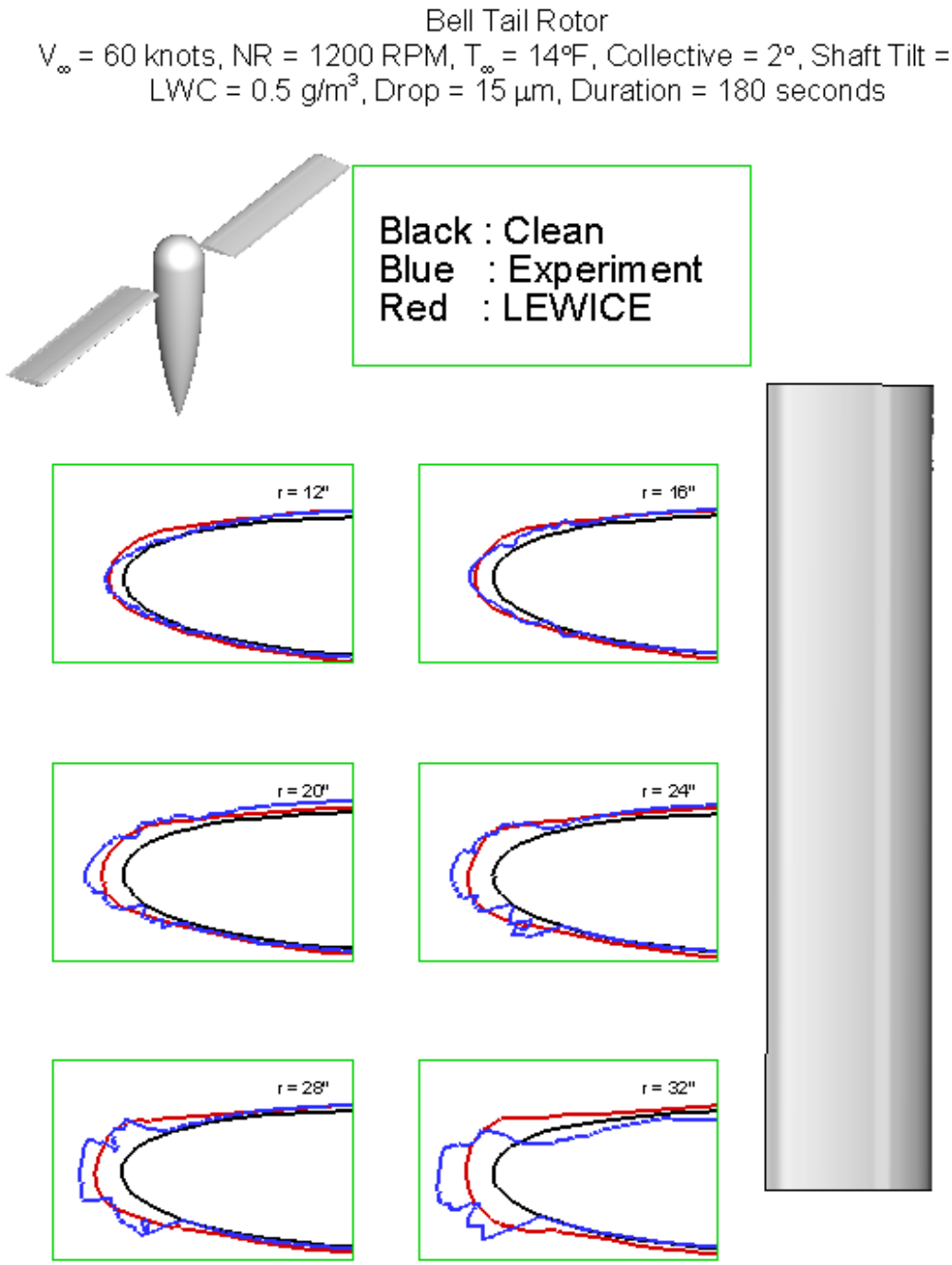

Figure 4.7: Comparison of Ice Shape for Run 53 (LEWICE, 4 steps).

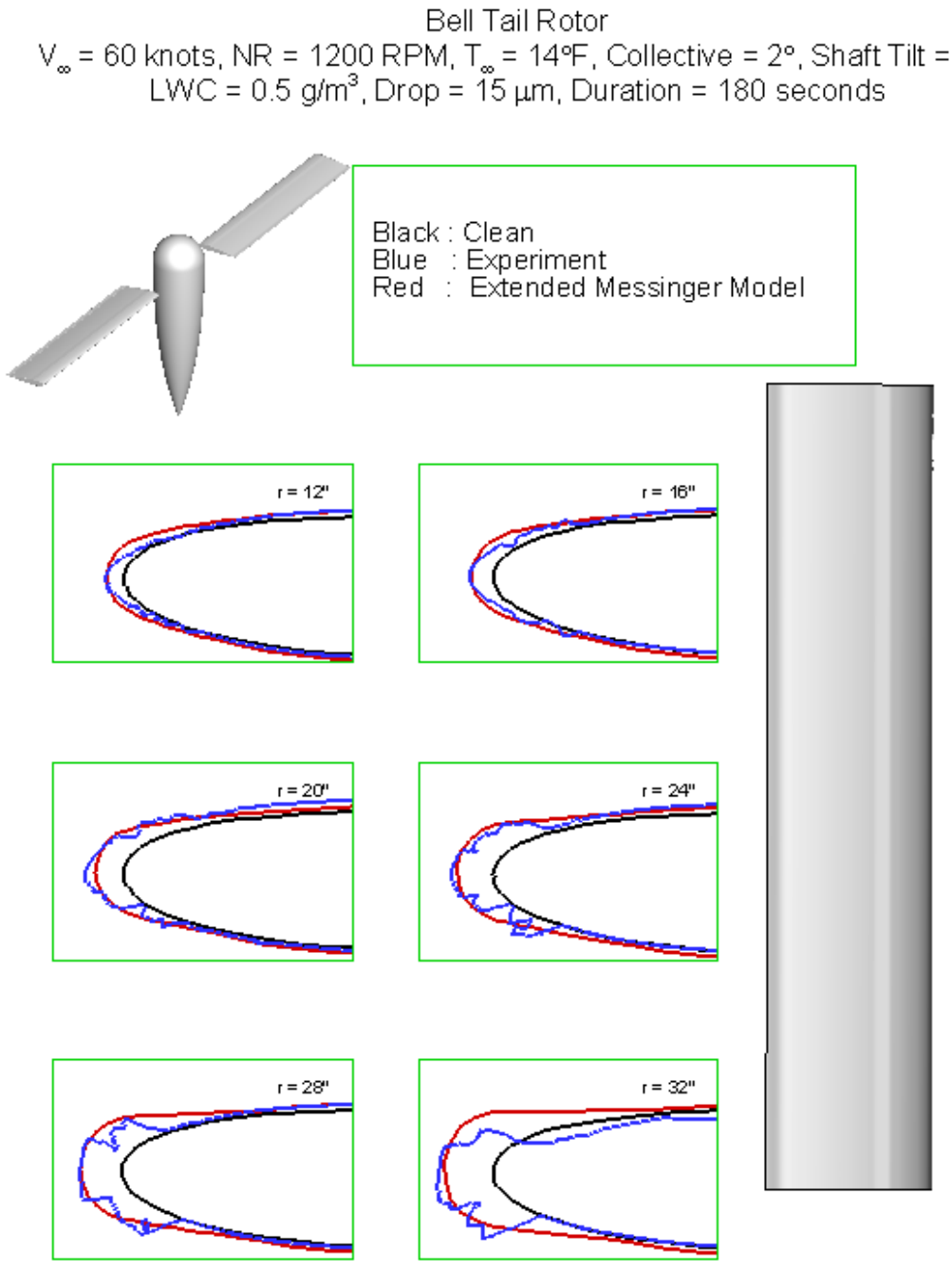

Figure 4.8: Comparison of Ice Shape for Run 53 (Extended Messinger Model, 4 steps).

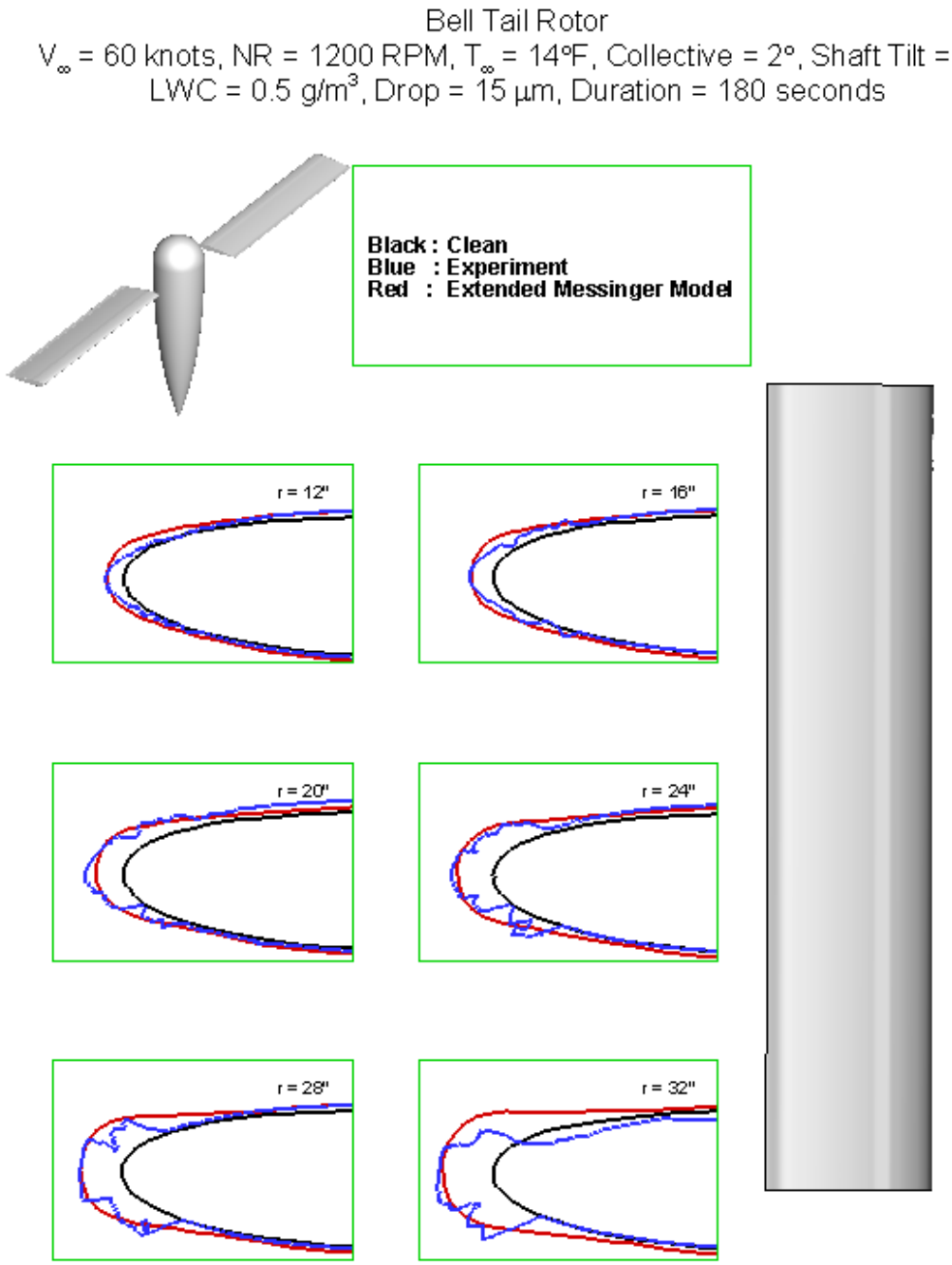

Figure 4.9: Comparison of Ice Shape for Run 53 (Extended Messinger Model, 8 steps).

Run54

Ice accretion simulations were done for another test condition, called Run54. Table 4.3 shows the corresponding test conditions. For this case, rotational speed of blade and collective pitch angle are higher than Run53. In present study, effect of various factors such as blade motion and kinetic heating on ice accretion simulation are examined. For all simulations, four data exchanges were made between GT-Hybrid and LEWICE / Extended Messinger model when predicting the ice growth. Figure 4.10 through Figure 4.13 contain comparisons of experimental ice and predicted ice for many of the conditions simulated. As seen in simulations for Run53, predicted ice shapes from both approaches are close to experimental ice shape at the inboard region. Ice shapes start to differ towards blade tip. For the effect of blade motion (Figure 4.12), there is marginal difference in predicted ice shape. In order to consider kinetic heating effect, surface temperature from GT-Hybrid (Figure 4.14) was fed into the Extended Messinger model. As seen in Figure 4.11, the ice thickness near blade tip is over-predicted without kinetic heating effect. By considering kinetic heating effect, improvement on prediction of ice shape is seen in Figure 4.13.

Table 4.3: Test Conditions for Run54 (NASA Glenn's IRT)

Parameter	Value
Forward Velocity (knot)	60
RPM	2100
Collective (Deg.)	8
LWC (g/m^3)	0.5
MVD (μm)	15
Temperature (K)	263.15
Time (min)	1

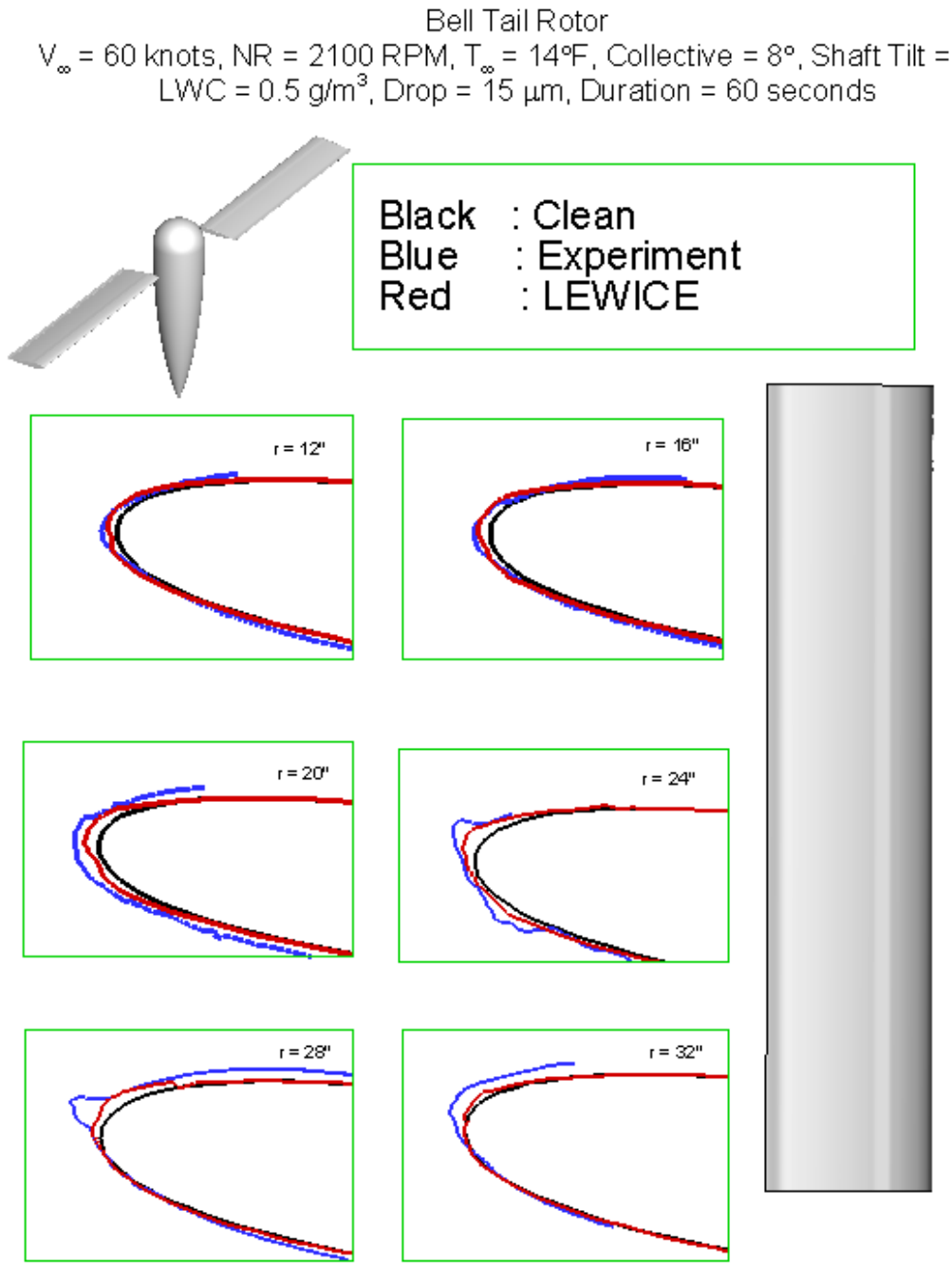

Figure 4.10: Comparison of Ice Shape for Run 54 (LEWICE).

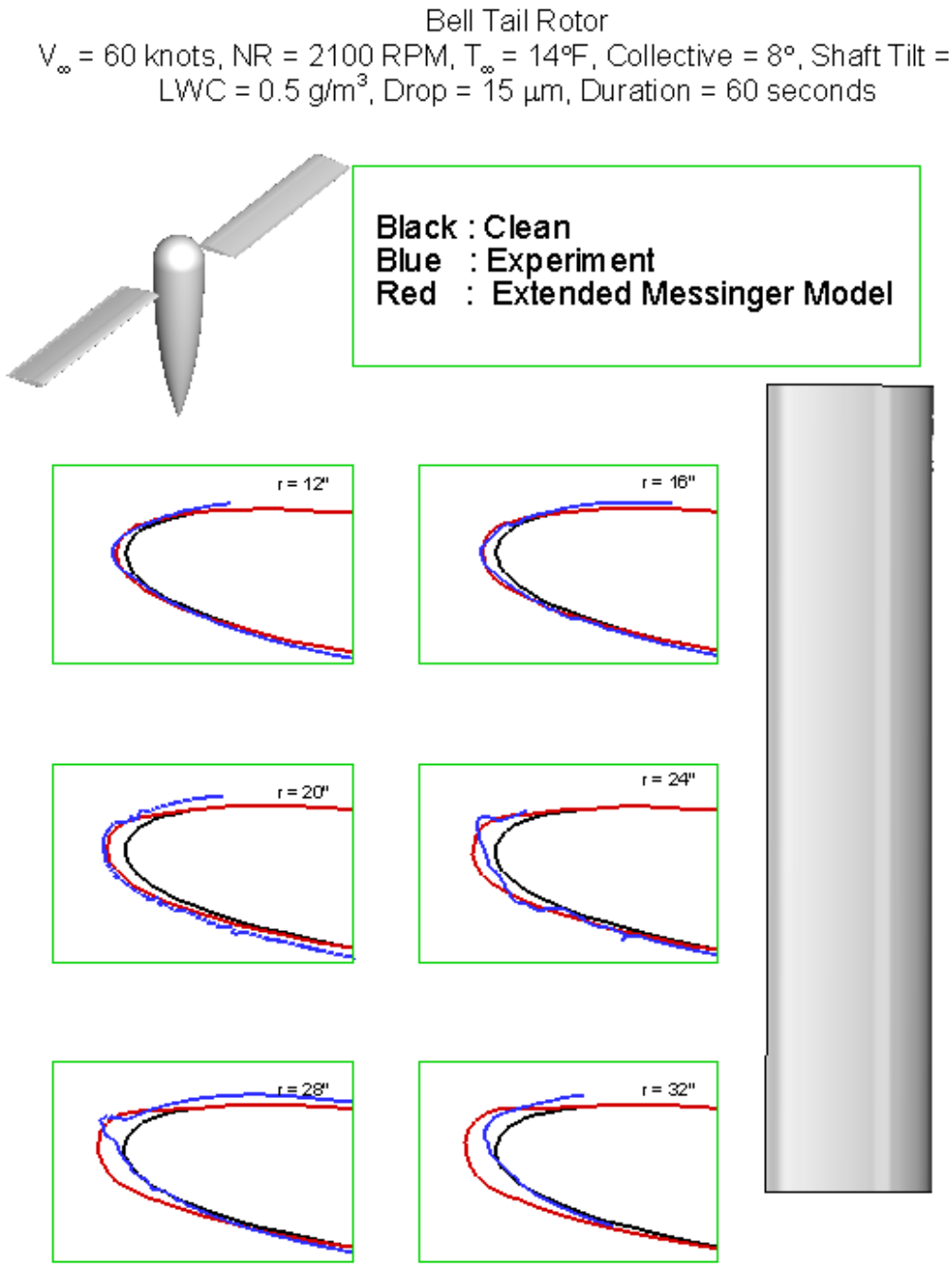

Figure 4.11: Comparison of Ice Shape for Run 54 (Extended Messinger Model).

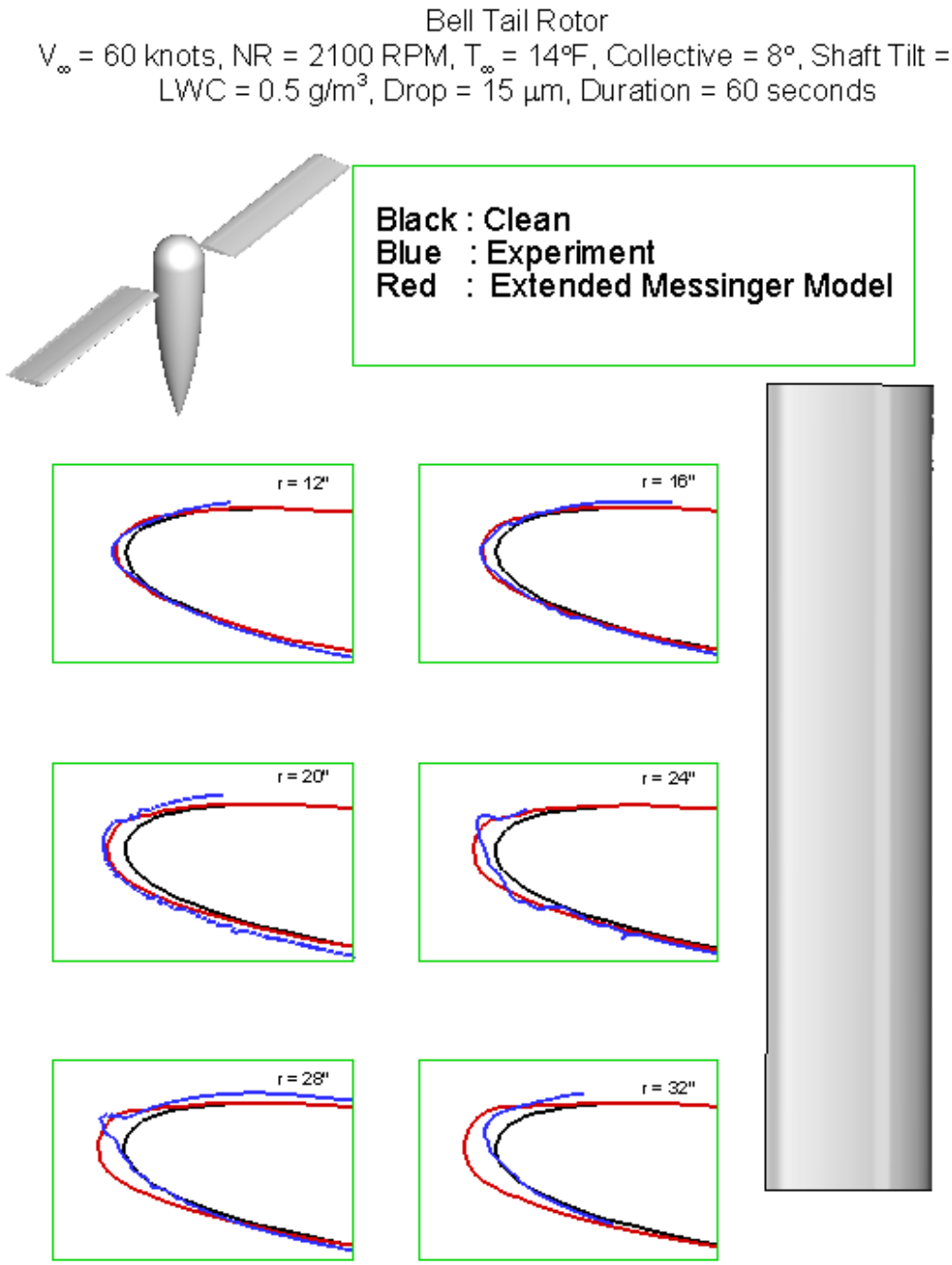

Figure 4.12: Comparison of Ice Shape for Run 54 (Extended Messinger Model, using measured flapping angle).

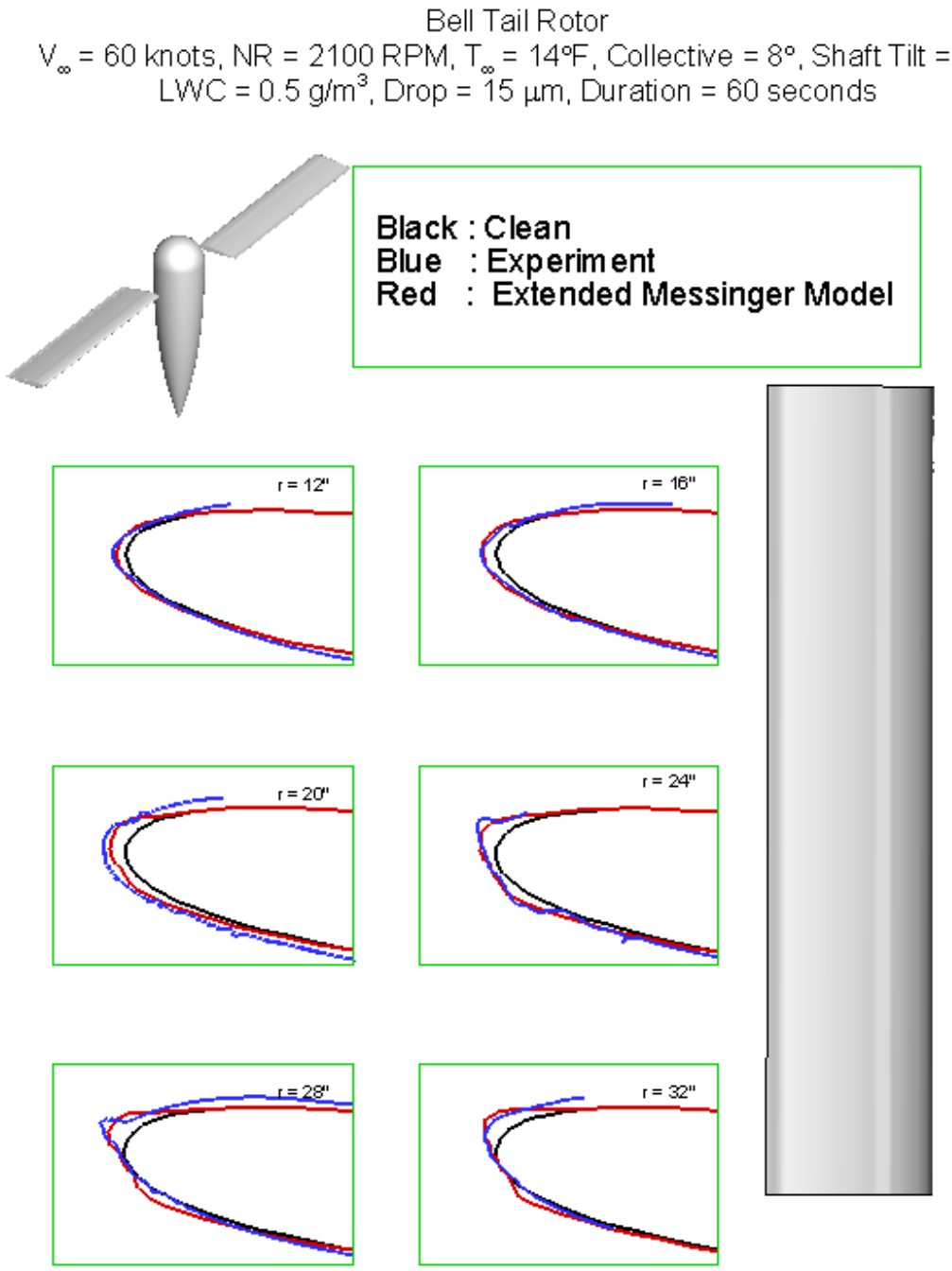

Figure 4.13: Comparison of Ice Shape for Run 54 (Extended Messinger Model, considering kinetic heating effect).

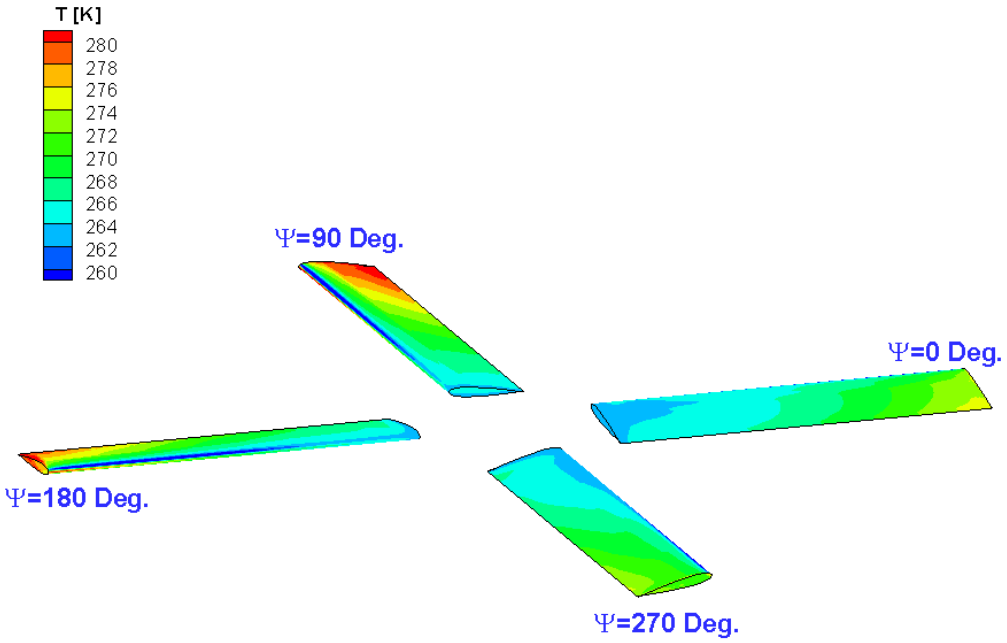

Figure 4.14: Predicted Blade Surface Temperature Distribution at Different Azimuth Locations from GT-Hybrid.

4.4 Degraded Performance Prediction

4.4.1 Run53

Performance predictions for clean rotor, measured and predicted ice shape from the Extended Messinger model have been done to investigate the effect of ice formation on rotor performance. The grid density for the clean rotor and iced rotor simulations are comparable, with the same number of nodes in the wrap-around, normal, and radial directions with comparable grid spacings. Other options (temporal and spatial discretization, turbulence models) were also kept the same in the clean and iced rotor simulations. Predicted thrust and power of clean, measured and predicted iced rotor have also been compared with measured values (unpublished data). The power of iced blade is increased by 35% and thrust is decreased by 16% compared to clean rotor. The computed and measured thrust values are in reasonable agreement. The predicted power is much lower than experiment. One of possible reason for this discrepancy is the lack of surface roughness modeling in the CFD solver. The performance degradation of the iced rotor compared to clean rotor is only qualitatively captured. Also, the effect of blade motion (flapping angle) on performance was examined. Figure 4.15 through Figure 4.20 contain comparison of sectional loads. Blade motion affects more sectional normal force distributions than sectional chordwise force distributions. For iced blade, significant increase of sectional chordwise force at advancing side is seen compared to clean rotor case.

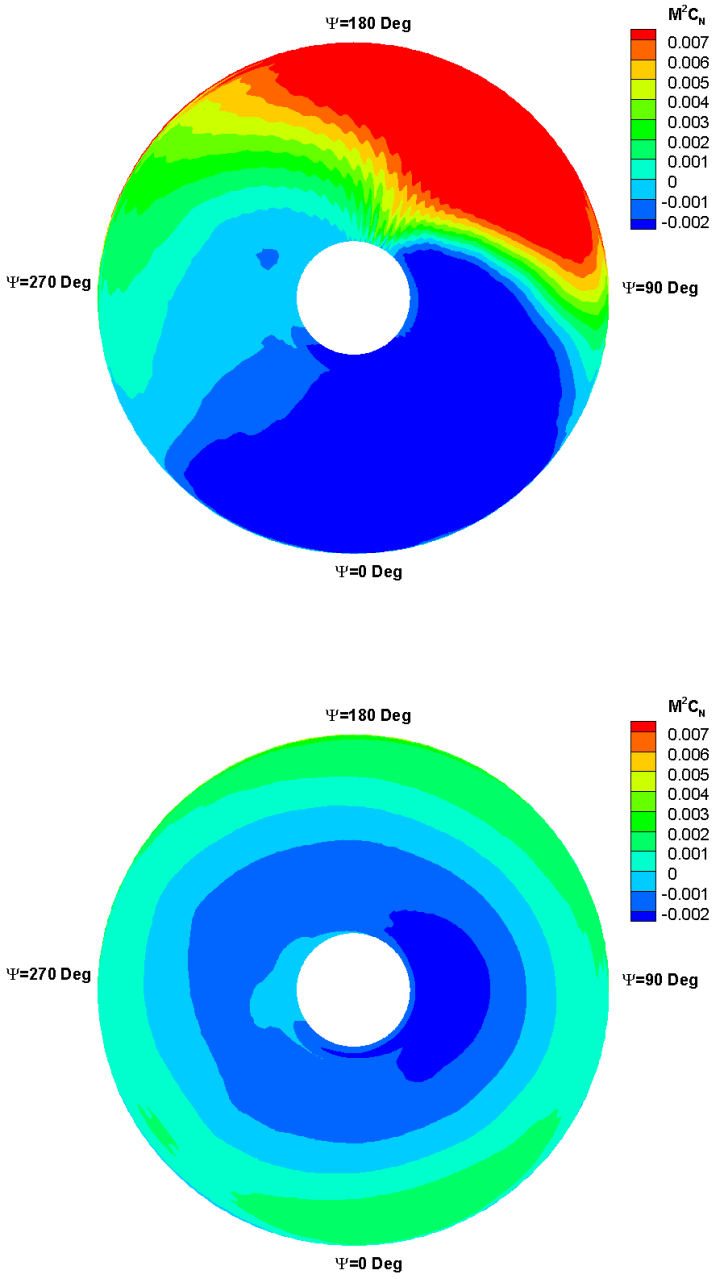

Figure 4.15: Comparison of Sectional Normal Force Distributions for using Measured Flapping Motion (Upper) and using Predicted Flapping Motion (Lower), Run53 (Clean Rotor).

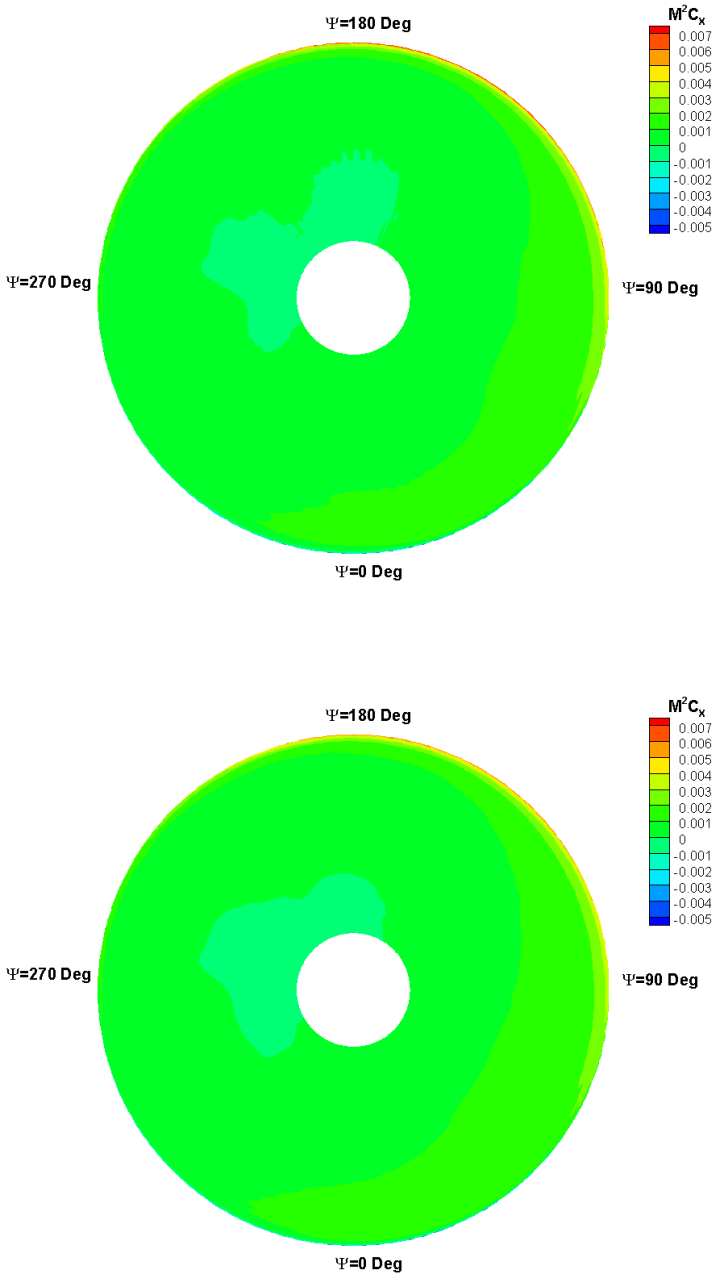

Figure 4.16: Comparison of Sectional Chordwise Force Distributions for using Measured Flapping Motion (upper) and using Predicted Flapping Motion (lower) , Run53 (Clean Rotor).

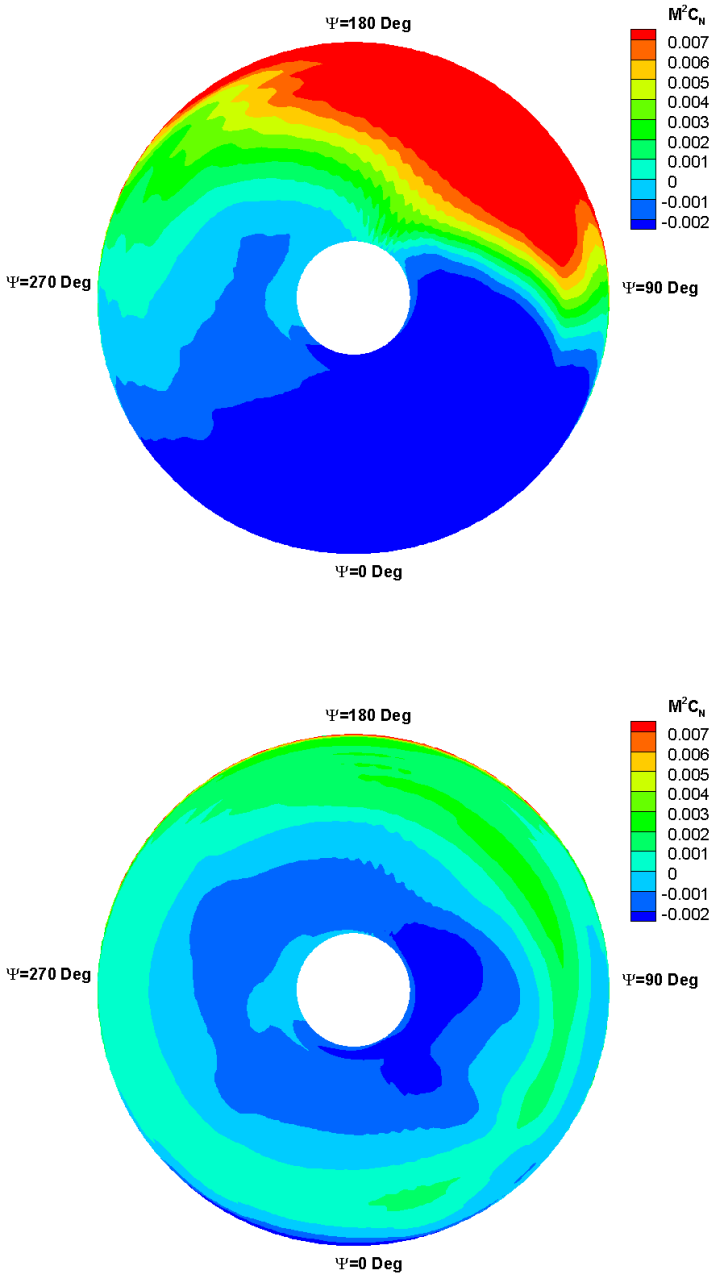

Figure 4.17: Comparison of Sectional Normal Force Distributions for using Measured Flapping Motion (Upper) and using Predicted Flapping Motion (Lower), Run53 (Measured Ice Shape).

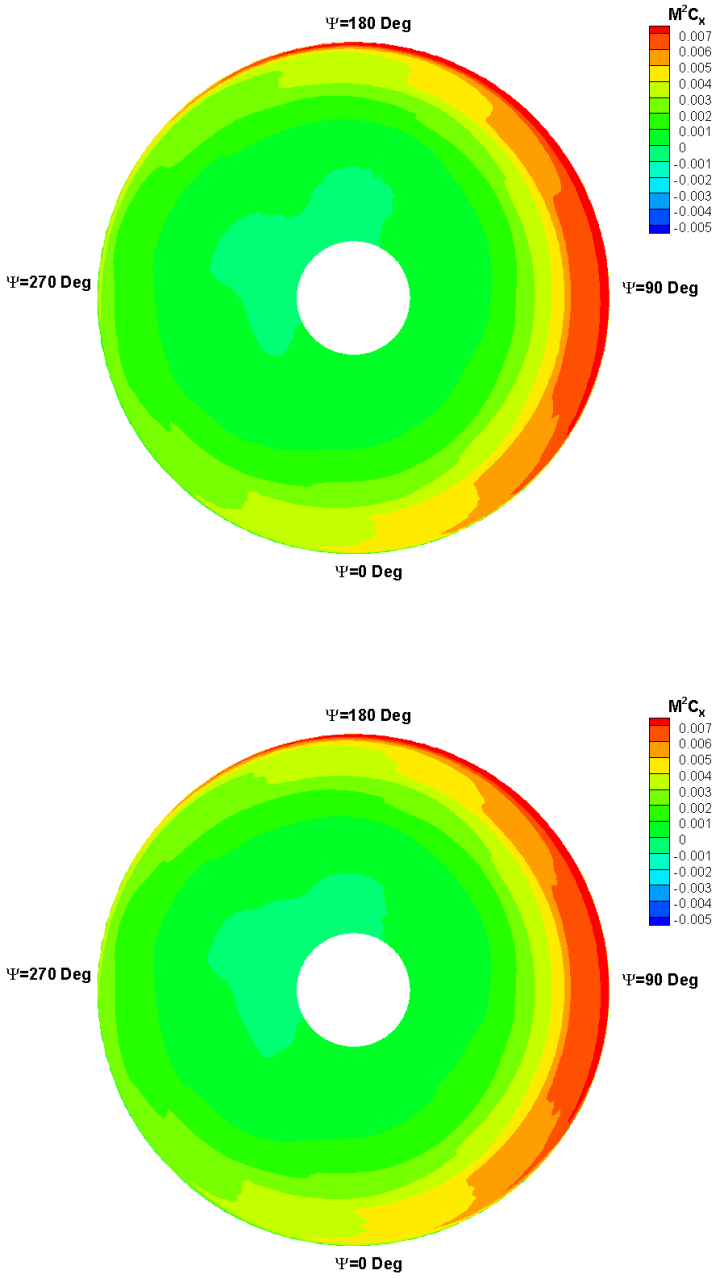

Figure 4.18: Comparison of Sectional Chordwise Force Distributions for using Measured Flapping Motion (upper) and using Predicted Flapping Motion (Lower) , Run53 (Measured Ice Shape).

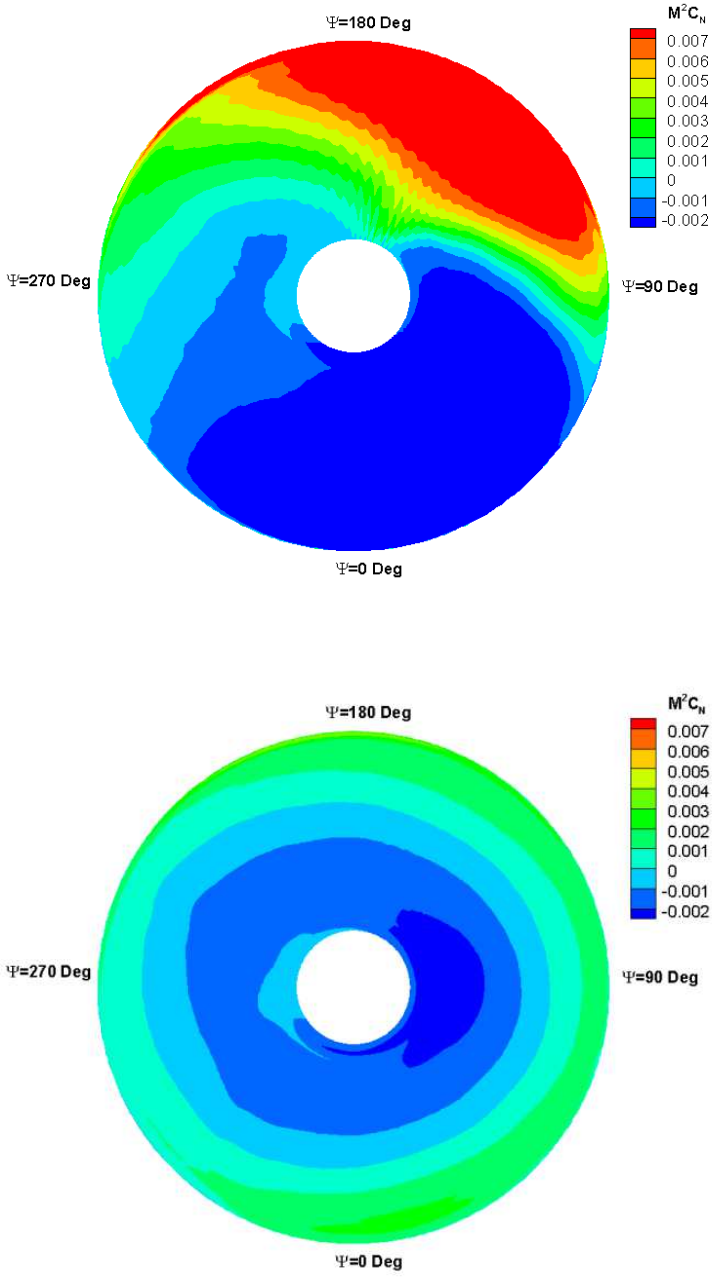

Figure 4.19: Comparison of Sectional Normal Force Distributions for using Measured Flapping Motion (Upper) and using Predicted Flapping Motion (Lower), Run53 (Predicted Ice Shape).

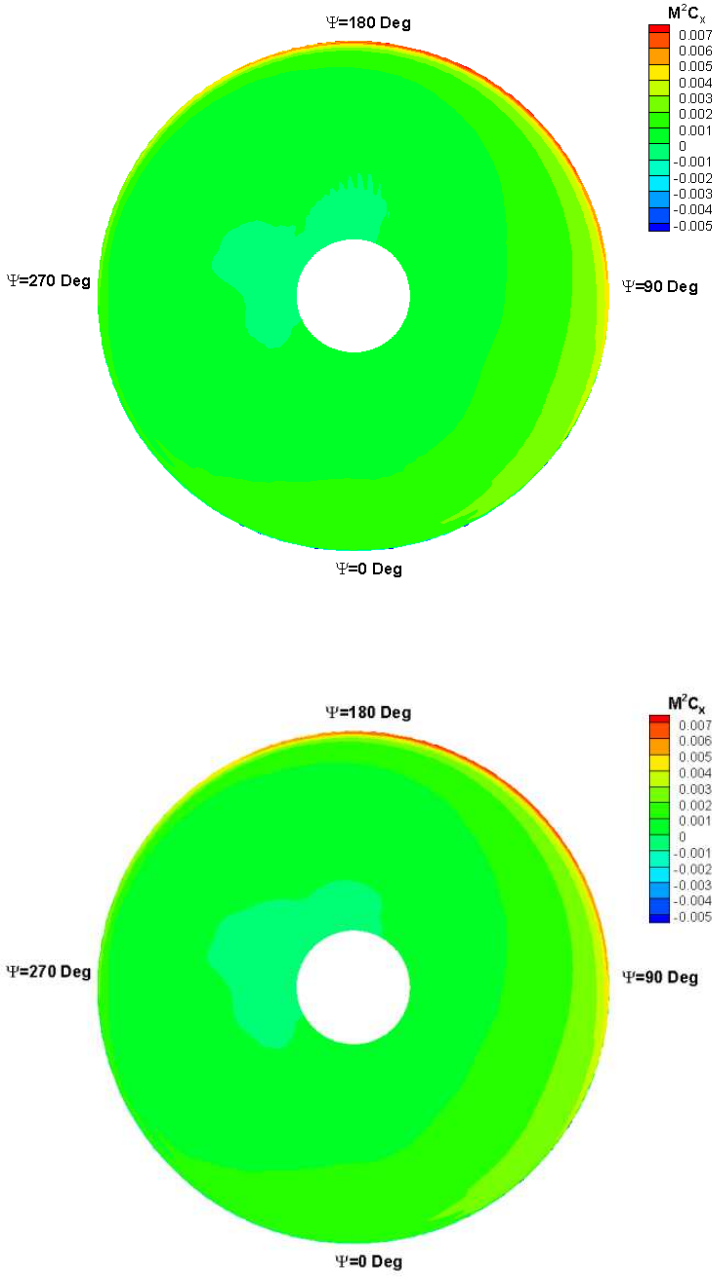

Figure 4.20: Comparison of Sectional Chordwise Force Distributions for using Measured Flapping Motion (Upper) and using Predicted Flapping Motion (Lower) , Run53 (Predicted Ice Shape).

4.4.2 Run54

Performance predictions for clean rotor and iced rotor have been done. In present study, ice shape from measurements is used instead of using predicted ice shape. The grid density for the clean rotor and iced rotor simulations are comparable, with the same number of nodes in the wrap-around, normal, and radial directions with comparable grid spacings. Other options (temporal and spatial discretization, turbulence models) were also kept the same in the clean and iced rotor simulations. Predicted thrust and power of clean and measured iced rotor have also been compared with measured values. When measured flapping motion is used in CFD simulation, the power is increased by 78.6% and thrust is decreased slightly compared to clean rotor. The power is increased by 32% in case of using predicted flapping motion. The computed and measured thrust values are in reasonable agreement. Like Run53 case, the predicted power is much lower than experiment. This discrepancy may be due to the lack of surface roughness modeling in the CFD solver and surface smoothing during the mesh generation. The performance degradation of the iced rotor compared to clean rotor is only qualitatively captured. Figure 4.21 through Figure 4.24 contain comparison of sectional loads. Unlike Run53, blade motion affects sectional normal force distributions and sectional chordwise force distributions. For iced blade, significant increase of sectional chordwise force near 180 deg azimuth location is seen compared to clean rotor case.

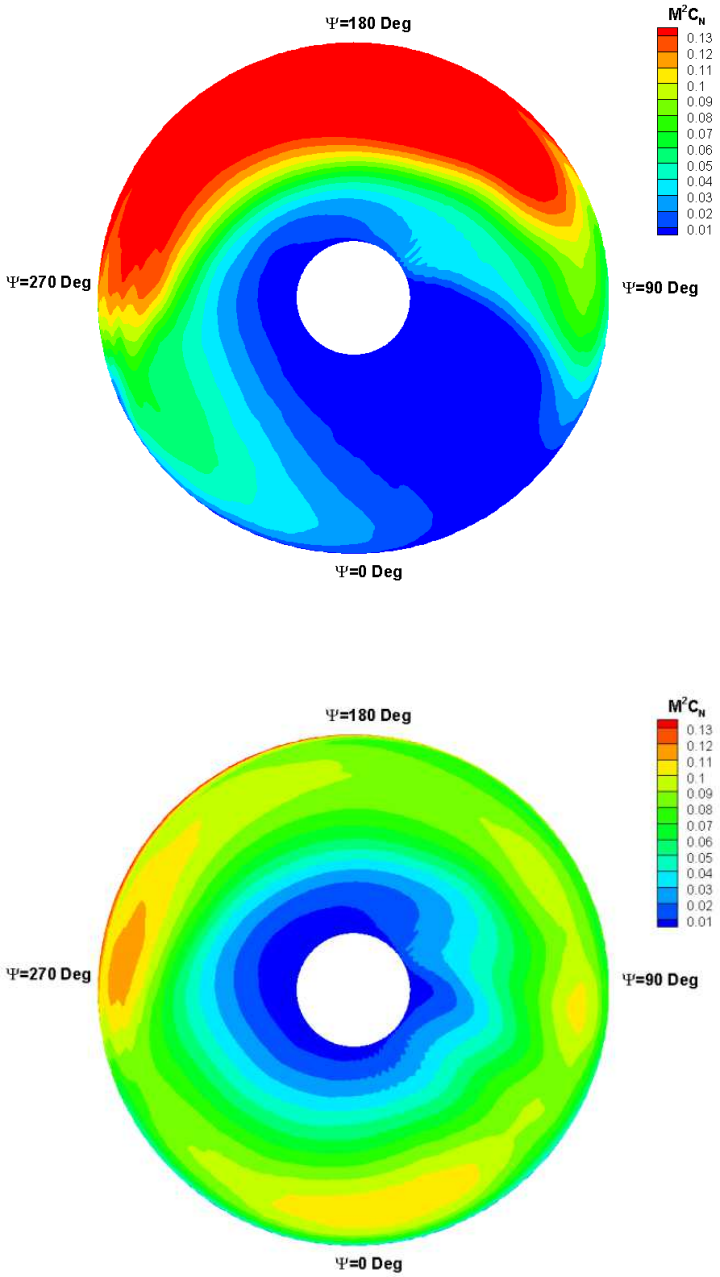

Figure 4.21: Comparison of Sectional Normal Force Distributions for using Measured Flapping Motion (Upper) and using Predicted Flapping Motion (Lower), Run54 (Clean Rotor).

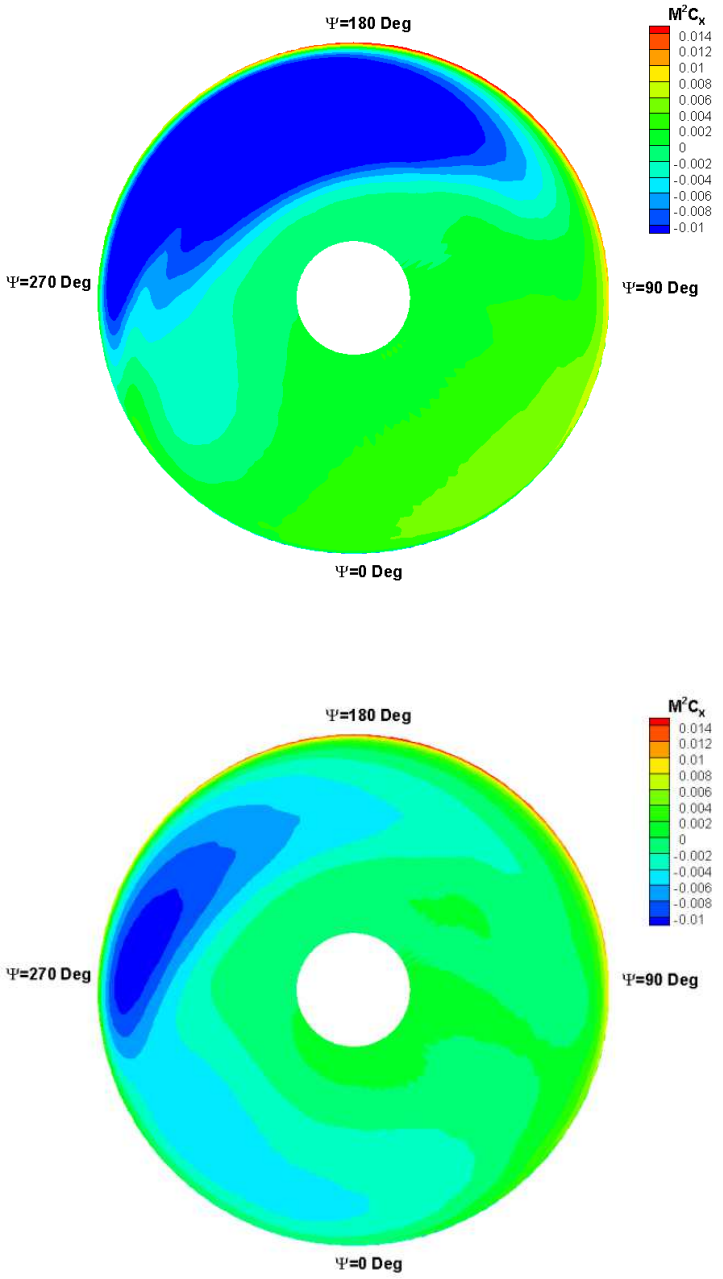

Figure 4.22: Comparison of Sectional Chordwise Force Distributions for using Measured Flapping Motion (Upper) and using Predicted Flapping Motion (Lower) , Run54 (Clean Rotor).

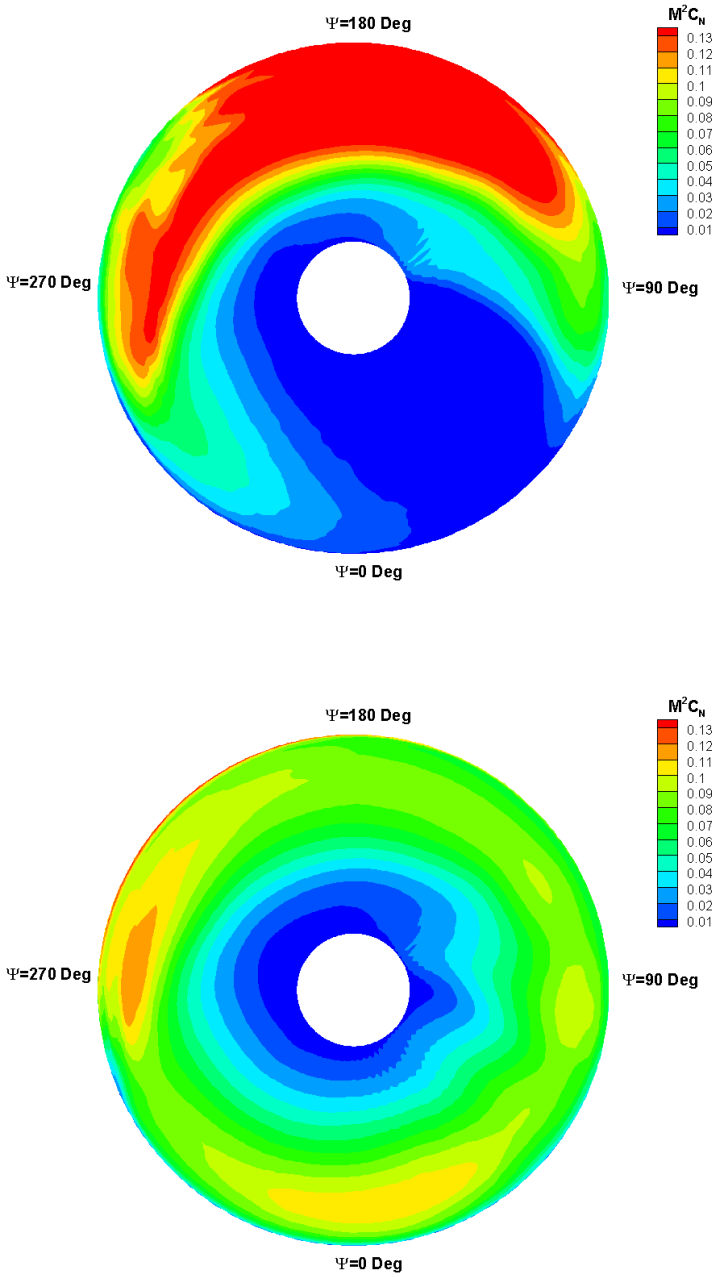

Figure 4.23: Comparison of Sectional Normal Force Distributions for using Measured Flapping Motion (Upper) and using Predicted Flapping Motion (Lower), Run54(Measured Ice Shape).

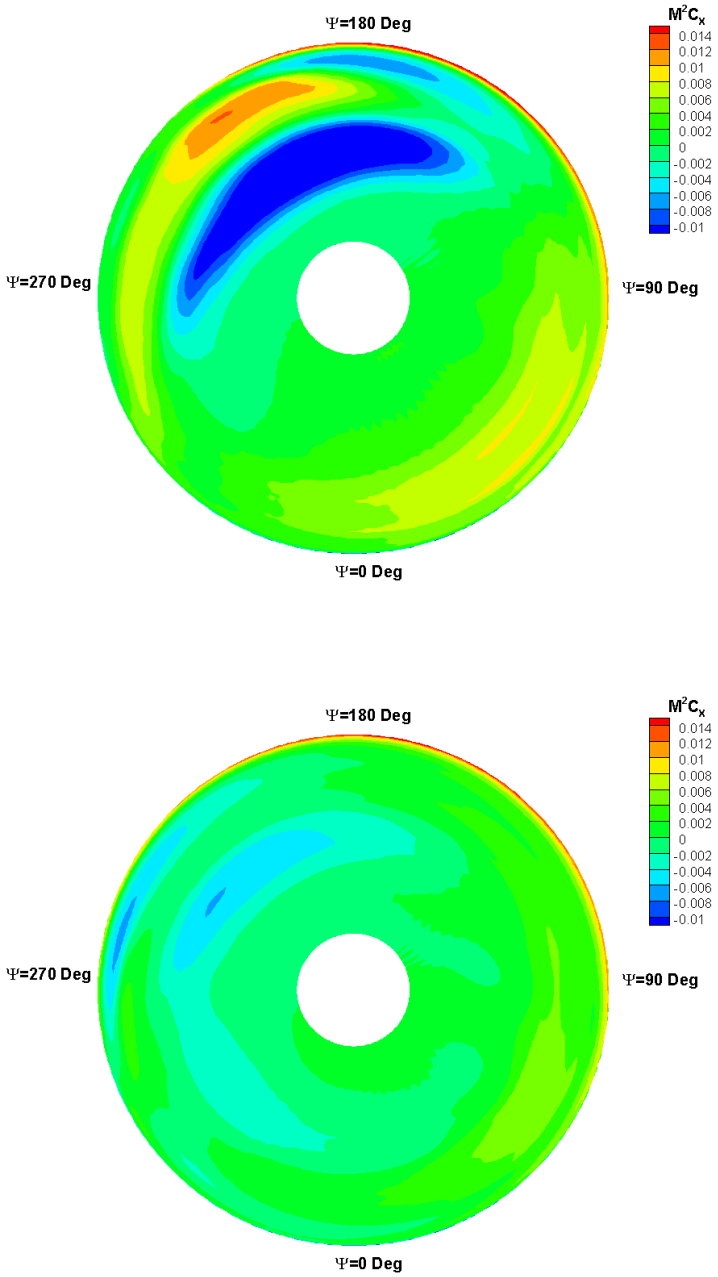

Figure 4.24: Comparison of Sectional Chordwise Force Distributions for using Measured Flapping Motion (Upper) and using Predicted Flapping Motion (Lower) , Run54 (Measured Ice Shape).

CHAPTER 5

3-D ROTOR BLADE ICE SHEDDING ANALYSIS

In this section, numerical simulations for 3-D rotor blade ice shedding are presented. As explained in introduction, ice shedding is one of inherent issues to helicopter. High centrifugal force on accreted ice causes it to release from the rotor blade.

5.1 Empirical Model for Self-shedding

An empirical model for self-shedding [21] was used in present ice shedding simulations. The following procedure used to determine the length of the shed ice and the time at which shedding occurs:

a. At any specified instant in time, the contact area, volume, and mass of the ice are computed. This is done using the simultaneous integration of the flow equations, structural dynamics equations, and the ice accretion equations in time.
b. The shear stress at the blade surface between the ice mass and the blade and the cohesive stresses exerted on a segment of ice by the neighboring ice mass are computed. The surface shear stresses are based on temperature and on the rotor blade surface ,using relationships derived from experimental data.
c. The components of the centrifugal, shear, and cohesive force vectors are summed up, on sections on the rotor blade.
d. The feasibility of shedding is examined. It is assumed that all the ice mass outboard of a given radial location will be shed if the sum of applied forces (centrifugal, edge cohesion, and optionally aerodynamic pressure) on the mass of ice exceeds the adhesion force.

Ice formed on a blade surface is subjected to several forces, with the most dominant shown in Figure 5.1. The ice shedding analysis is done by assuming that the lift and drag forces are negligible as well as the blade vibratory and flexing loads compared to centrifugal force. The balance force on the shedding ice piece only rely on the centrifugal (F_{cen}), adhesive (F_{adh})and cohesion (F_{coh}) forces.

$$F_{cen} \approx F_{adh} + F_{coh} \tag{5.1}$$

The centrifugal force is calculated by:

$$F_{cen} = m_{ice}\, r\, \Omega^2 \tag{5.2}$$

The mass of accreted ice (m_{ice}) is obtained by:

$$m_{ice} = Vol_{ice}\, \rho_{ice} \tag{5.3}$$

One of important parameter in ice shedding analysis is the ice density. In current study, the Laforte [94] empirical equation, which is based on ice accretion on a rotating cylinder, is used. This equation is valid when the air temperature is lower than the freezing temperature.

$$\rho_{ice} = 917 \left(\frac{MVD\sqrt{V_\infty^2 + r^2\Omega^2}}{MVD\sqrt{V_\infty^2 + r^2\Omega^2} + 2.6 \times 10^{-6}\left[T_f - T\right]} \right) \tag{5.4}$$

where MVD is median volumetric diameter, r is radial position, Ω is rotating speed, V_∞ is freestream velocity, T is temperature and T_f is freezing temperature.

The cohesion force is given by:

$$F_{coh} = \sigma A_c \tag{5.5}$$

The ice cross section area is calculated by (Figure 5.2):

$$A_c = \int_{S_{low}}^{S_{hi}} h_{ice}\, ds \tag{5.6}$$

The failure stress as a function of grain size (d) is given by [21]:

$$\sigma_f = 9.39 \times 10^9 \left[1 + 0.001384\left(T_f - T\right)\right] \frac{0.47 \times 10^{-6}}{9 \times 10^{-3} + d} \tag{5.7}$$

Table 5.1 shows grain sizes (d) used in present simulations:

Table 5.1: Grain Size [21]

Temperature [°C]	Grain Size [μm]
-5	242
-10	171
-15	216
-20	66

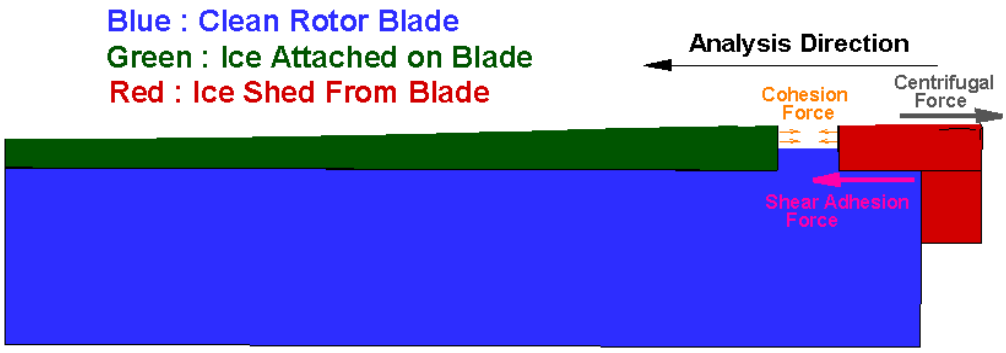

Figure 5.1: Forces on Accreted Ice.

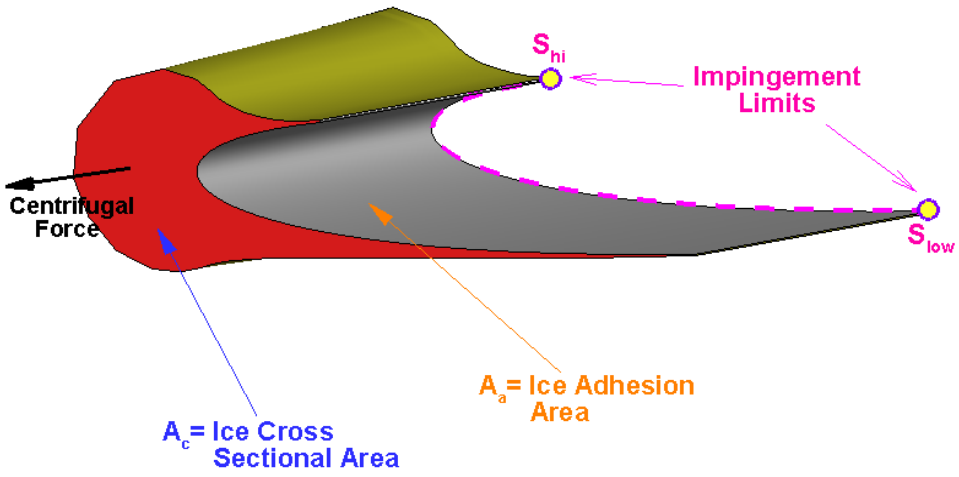

Figure 5.2: Ice Cohesion and Adhesion Forces Details.

In Eq. 5.3, the volume (Vol_{ice}) of shedding ice is calculated by:

$$Vol_{ice} = \left(A_{c,j+1} - A_{c,j}\right) l_{ice} \tag{5.8}$$

The adhesive force at the ice/airfoil surface interface, which represent the molecular and mechanical bonds between the ice and substrate, is calculated by:

$$F_{adh} = \tau A_a \tag{5.9}$$

with an adhesive surface of

$$A_a = (S_{hi} - S_{low}) l_{ice} \tag{5.10}$$

The adhesion shear stress (τ) is expressed as a function of temperature such as:

$$\tau = 10^6 \times \left(0.26 - 0.013 \times (T + 20)\right) \tag{5.11}$$

Equation (5.11) is a linear curve fit for data from Reference 21.

5.2 Rotor Blade Shedding Analysis

Following the application of the present ice accretion methodology to rotors in hover and forward flight, numerical simulations have been performed for the rotor blade ice shedding. A rotor configuration tested by Fortin [21] was considered. The rotor is a 1/18-scale model of a small helicopter. The rotor diameter is 780 mm and chord length is 69.75 mm. The blades are untwisted, and made of NACA 0012 sections. Table 5.2 shows the corresponding test conditions. The forward speed of the rotor was 15 m/sec, leading to a low advance ratio (forward speed to tip speed ratio) of 0.115. The ambient temperature was parametrically varied between -20 deg Celsius and -5 degree C.

A C-H grid, 131 (chordwise) x 70(spanwise) x 45 (normal), was used for flow field prediction. Figure 5.3 shows 3-D blade mesh used for simulations The predicted flow field solutions from GT-Hybrid were fed into the present Eulerian droplet model and the ice accretion (Extended Messinger model) is subsequently computed. In this study, the model rotor was assumed to be rigid and operated at a fixed collective pitch of 6 degrees with zero cyclic pitch.

After calculating ice thickness, a shedding analysis was done to check if and when the centrifugal forces outboard of a given radial station exceed the surface adhesion forces that exist at each cross section of the ice shape. The accretion time at which such shedding occurs as well as the thickness and length of the shed ice shape was extracted from the present simulations. Figures 5.4 through 5.7 show comparisons with measurement and another numerical simulation [95]. Figure 5.4 shows for the standard test that the ice thickness at the stagnation point grows almost linearly along the blade and increases from the hub to the tip. The results from Reference 95 show overestimation of the ice thickness over the entire length of the blade. The present simulations show good agreement with measurement except mid-span region. Reasonably good agreement and similar trend with prediction of LEWICE were found for the other properties, such as the length of the shed ice and the time at which shedding occurs.

Table 5.2: Test Conditions of Ice Shedding Analysis

Parameter	Value
Forward Velocity (m/sec)	15
Tip speed (m/sec)	130
Collective (Deg.)	6
LWC (g/m^3)	0.842
MVD (μm)	26.7
Temperature (°C)	-20 to -5

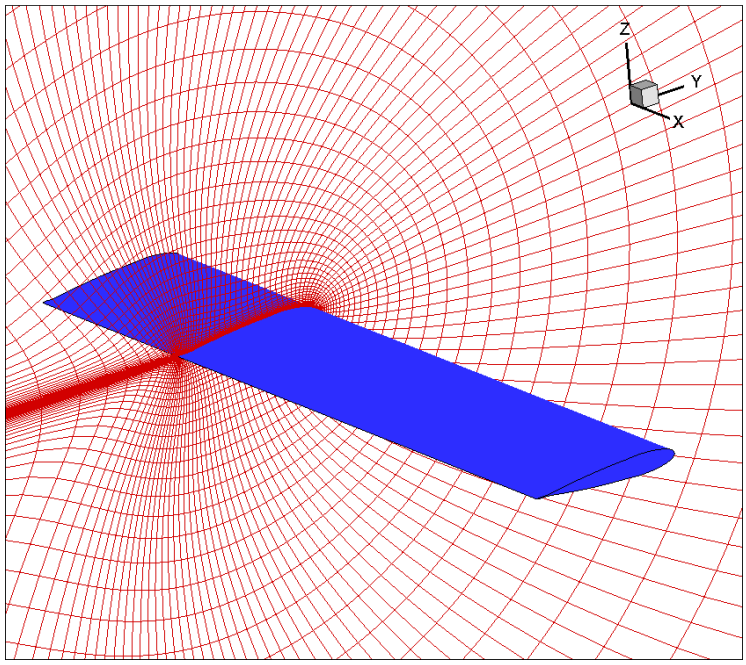

Figure 5.3: Spinning Rotor Blade II (SRB-II) Grid System (131 x 70 x 45).

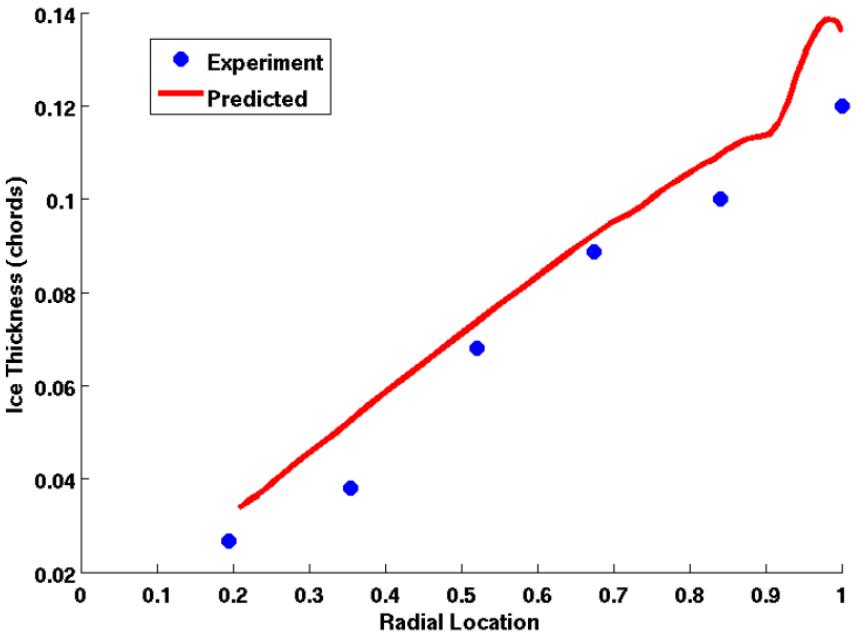

a) Result from Reference 95 (OVERFLOW + LEWICE3D)

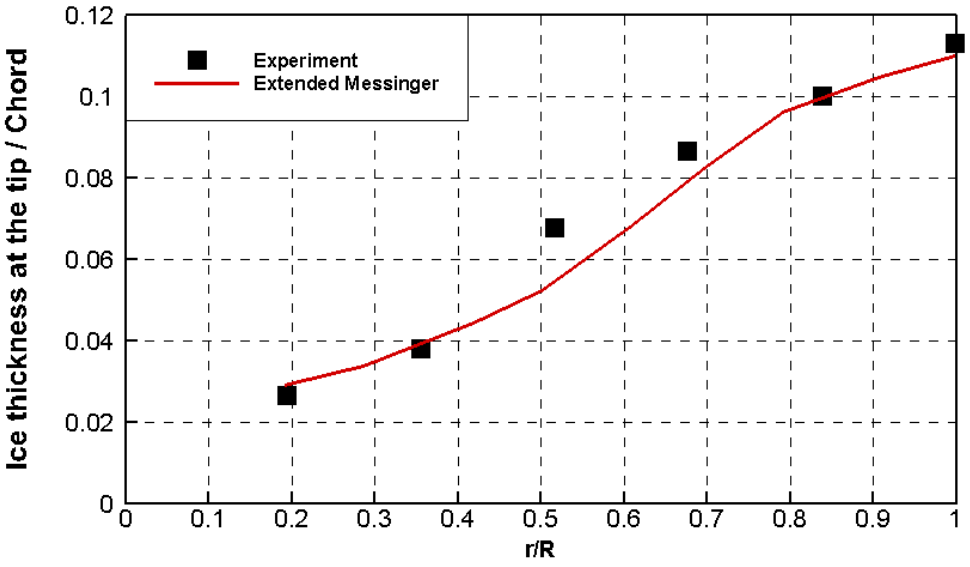

b) Present Result (GT-Hybrid + Extended Messinger)

Figure 5.4: Comparison of Ice Thickness along the Blade Span

(Standard Test, Ice Accretion Time=130 sec).

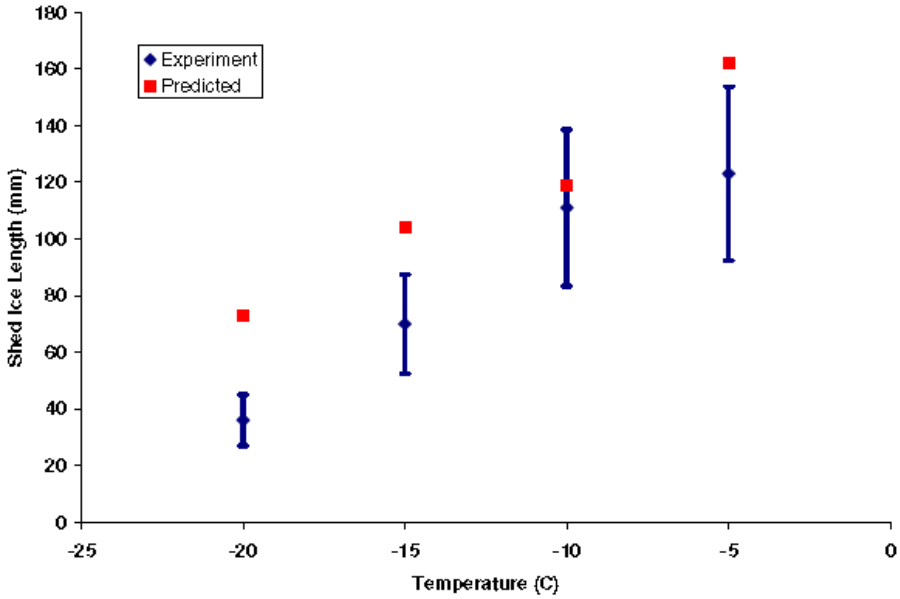

a) Result from Reference 95 (OVERFLOW + LEWICE3D)

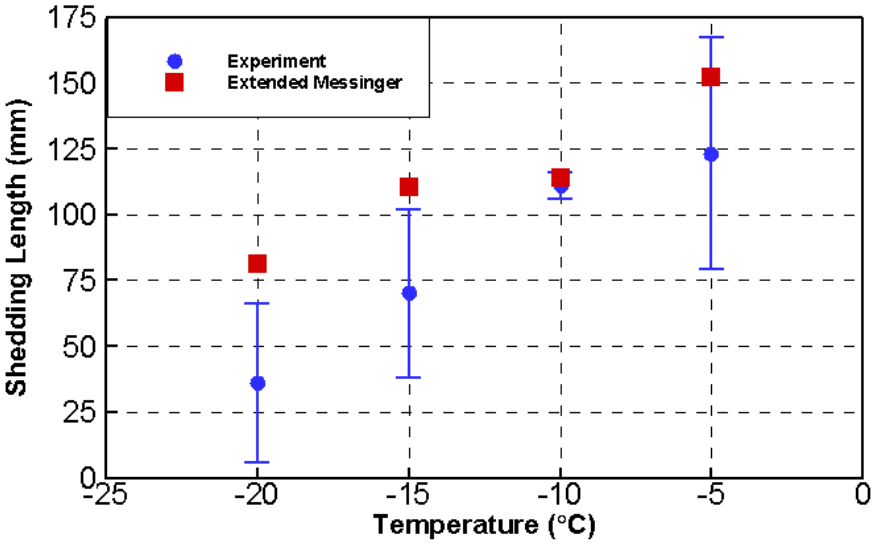

b) Present Result (GT-Hybrid + Extended Messinger)

Figure 5.5: Shedding Length versus Temperature.

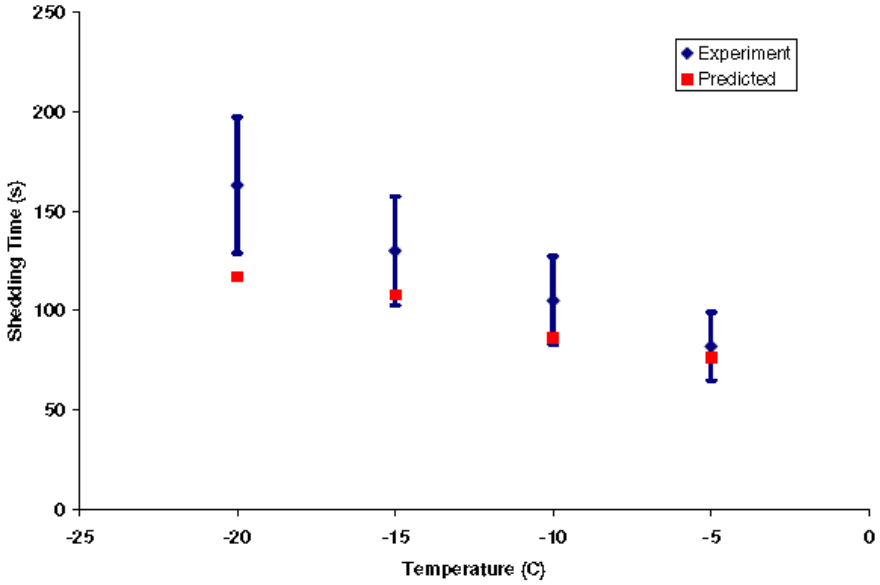

a) Result from Reference 95 (OVERFLOW + LEWICE3D)

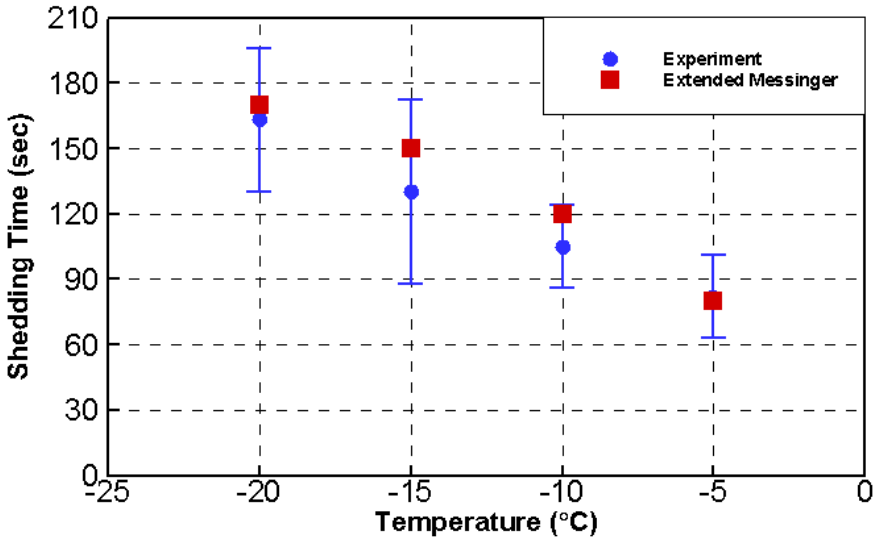

b) Present Result (GT-Hybrid + Extended Messinger)

Figure 5.6: Shedding Time versus Temperature.

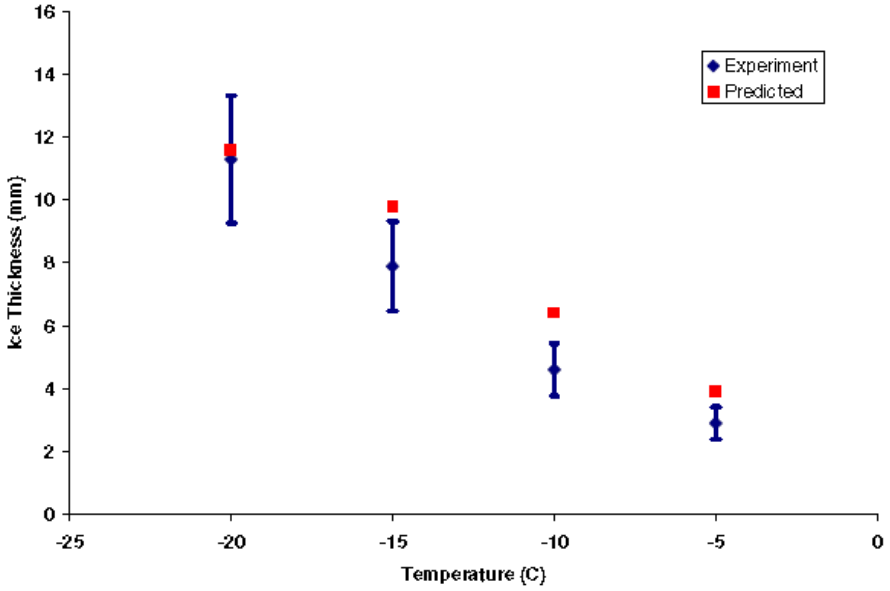

a) Result from Reference 95 (OVERFLOW + LEWICE3D)

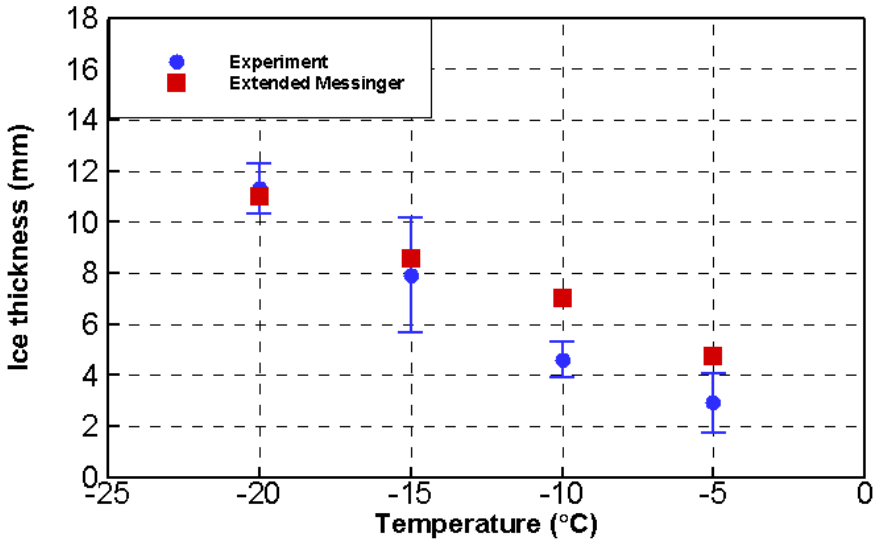

b) Present Result (GT-Hybrid + Extended Messinger)

Figure 5.7: Ice Thickness at Tip versus Temperature.

CHAPTER 6

NUMERICAL SIMULATION OF ELECTROTHERMAL DEICING

LEWICE and an in-house 3D heat conduction solver were used for the study of electrothermal deicing problem. LEWICE uses 2-D strip theory, and solves the heat conduction equations on a Cartesian grid. A fully 3-D heat conduction analysis that acknowledges curvature of the heat elements, and the finite spanwise extent of the heating elements has been developed. The selected cases include validation studies for some of benchmark cases and deicing problems for helicopter rotor blades.

6.1 Development of a 3-D Heat Conduction Solver

6.1.1 Governing Equation

In order to develop a 3-D, unsteady, mathematical model for heat conduction in a composite blade, the followings are assumed:

1. The ambient temperature, air temperature at blade surface and all heat transfer coefficients are constant with respect to time.
2. The thermal physical properties of the material composing each layer inside blade can be different, but do not rely on temperature.
3. There is perfect thermal contact between each layer.

The mathematical formulation for the problem of unsteady heat conduction in a composite blade with electrothermal heating can be represented as with the above assumptions :

$$\left(\rho_j C_{p,j}\right)\frac{\partial T_j}{\partial t} = k_j\frac{\partial^2 T_j}{\partial x^2} + k_j\frac{\partial^2 T_j}{\partial y^2} + k_j\frac{\partial^2 T_j}{\partial z^2} + q_j \qquad (6.1)$$

where j stands for the layer and where

ρ_j = density of the j^{th} layer;

$C_{p,j}$ = specific heat capacity of the jth layer;

T_j = temperature in the jth layer;

k_j = thermal conductivity of the jth layer;

q_j = rate of heat generation per unit volume in the jth layer;

t = time variable;

x, y, z = spatial coordinates.

6.1.2 Mathematical and Numerical Formulation

Coordinate Transformation

On a general curvilinear coordinate system, Eq. (6.1) may be expressed as follows after coordinate transformation used in Chapter 2.3:

$$\frac{\partial}{\partial t}\left(\rho_j C_{p,j}\frac{T_j}{J}\right) = k_j\frac{\partial P}{\partial \xi} + k_j\frac{\partial Q}{\partial \eta} + k_j\frac{\partial R}{\partial \zeta} + \frac{q_j}{J} \tag{6.2}$$

where,

$$P = A_1 T_\xi + A_2 T_\eta + A_3 T_\zeta$$

$$Q = A_2 T_\xi + A_4 T_\eta + A_5 T_\zeta$$

$$R = A_3 T_\xi + A_5 T_\eta + A_6 T_\zeta \tag{6.3}$$

and,

$$A_1 = \frac{\xi_x^2 + \xi_y^2 + \xi_z^2}{J}$$

$$A_2 = \frac{\xi_x\eta_x + \xi_y\eta_y + \xi_z\eta_z}{J}$$

$$A_3 = \frac{\xi_x\zeta_x + \xi_y\zeta_y + \xi_z\zeta_z}{J}$$

$$A_4 = \frac{\eta_x^2 + \eta_y^2 + \eta_z^2}{J}$$

$$A_5 = \frac{\zeta_x \eta_x + \zeta_y \eta_y + \zeta_z \eta_z}{J}$$

$$A_6 = \frac{\zeta_x^2 + \zeta_y^2 + \zeta_z^2}{J}$$

In the above equations, J is the Jacobian of transformation, given as the determinant of the following matrix:

$$J = det \begin{vmatrix} \xi_x & \xi_y & \xi_z \\ \eta_x & \eta_y & \eta_z \\ \zeta_x & \zeta_y & \zeta_z \end{vmatrix} \tag{6.4}$$

The metrics of transformation (ξ_x, ξ_y, ξ_z) may be evaluated in terms of quantities as $\partial x/\partial \xi$, $\partial y/\partial \eta$ etc. through the following matrix equation:

$$\begin{bmatrix} \xi_x & \xi_y & \xi_z \\ \eta_x & \eta_y & \eta_z \\ \zeta_x & \zeta_y & \zeta_z \end{bmatrix} = \begin{bmatrix} x_\xi & x_\eta & x_\zeta \\ y_\xi & y_\eta & y_\zeta \\ z_\xi & z_\eta & z_\zeta \end{bmatrix}^{-1} \tag{6.5}$$

Spatial Dirscretization

The discretized form of the governing equations, Eq. (6.2), at a cell (*i*,*j*,*k*) may be written as follows using central differences:

$$\frac{\rho_j C_{p,j}}{J}\left(\frac{T_{i,j,k}^{n+1} - T_{i,j,k}^{n}}{\Delta t}\right) = k_j \frac{P_{i+\frac{1}{2},j,k} - P_{i-\frac{1}{2},j,k}}{\Delta \xi} + k_j \frac{Q_{i,j+\frac{1}{2},k} - Q_{i,j-\frac{1}{2},k}}{\Delta \eta} + k_j \frac{R_{i,j,k+\frac{1}{2}} - R_{i,j,k-\frac{1}{2}}}{\Delta \zeta} + \frac{q_j}{J} \tag{6.6}$$

where:

$$\Delta \xi = \xi_{i+\frac{1}{2},j,k} - \xi_{i-\frac{1}{2},j,k} = 1$$

$$\Delta \eta = \eta_{i,j+\frac{1}{2},k} - \eta_{i,j-\frac{1}{2},k} = 1 \tag{6.7}$$

$$\Delta\zeta = \zeta_{i,j,k+\frac{1}{2}} - \zeta_{i,j,k-\frac{1}{2}} = 1$$

Here, $\left(\mathrm{i} \pm \frac{1}{2}, \mathrm{j} \pm \frac{1}{2}, \mathrm{k} \pm \frac{1}{2}\right)$ represents six faces of the cell. Using the central difference operator, δ, Eq. (6.6) is written in the following form:

$$\frac{\rho_j C_{p,j}}{J}\left(\frac{T_{i,j,k}^{n+1} - T_{i,j,k}^{n}}{\Delta t}\right) = \delta_\xi k_j P + \delta_\eta k_j Q + \delta_\zeta k_j R + \frac{q_j}{J} \tag{6.8}$$

Time Marching Scheme

In an implicit formulation with first order backward differencing in time, Eq. (6.8) may be written as:

$$\frac{\rho_j C_{p,j}}{J}\frac{\Delta T^{n+1}}{\Delta t} = \delta_\xi k_j P^{n+1} + \delta_\eta k_j Q^{n+1} + \delta_\zeta k_j R^{n+1} + \frac{q_j}{J} \tag{6.9}$$

Here, $\Delta T^{n+1} = T^{n+1} - T^n$, the superscritp n and n+1 represent time level. The inviscid flux terms are linearized using Taylor series expansion as follows:

$$P^{n+1} \cong P^n + [A^n]\Delta T^{n+1}$$

$$Q^{n+1} \cong Q^n + [B^n]\Delta T^{n+1} \tag{6.10}$$

$$R^{n+1} \cong R^n + [C^n]\Delta T^{n+1}$$

Where the flux Jacobian matrices are defined as:

$$[A] = \frac{\partial P}{\partial T} \quad [B] = \frac{\partial Q}{\partial T} \quad [C] = \frac{\partial R}{\partial T}$$

With Eq. (6.10), Eq (6.9) may be re-arranged as:

$$\left[1 - \frac{J\Delta t k_j}{\rho_j C_{p,j}}\left(\delta_\xi [A]^n + \delta_\eta [B]^n + \delta_\zeta [C]^n\right)\right]\Delta T^{n+1} = (RHS)^n \tag{6.11}$$

$$(RHS)^n = \frac{J\Delta t k_j}{\rho_j C_{p,j}}\left(\delta_\xi P^n + \delta_\eta Q^n + \delta_\zeta R^n\right) + \frac{q_j\,\Delta t}{\rho_j C_{p,j}} \tag{6.12}$$

Equation (6.11) is a matrix system, which is computationally very expensive to invert. To reduce the computational time, the matrix inside the bracket on the left-hand

side is approximately factored using an alternating direction implicit (ADI) method. In the ADI scheme, Eq. (6.11) is expressed as:

$$\left[1-\frac{J\Delta tk_j}{\rho_j C_{p,j}}\delta_\xi[A]^n\right]\left[1-\frac{J\Delta tk_j}{\rho_j C_{p,j}}\delta_\eta[B]^n\right]\left[1-\frac{J\Delta tk_j}{\rho_j C_{p,j}}\delta_\zeta[C]^n\right]\Delta T^{n+1}=(RHS)^n \quad (6.13)$$

$$\left[1-\frac{J\Delta tk_j}{\rho_j C_{p,j}}\delta_\xi[A]^n\right]\Delta T^{n+\frac{1}{3}}=(RHS)^n$$

$$\left[1-\frac{J\Delta tk_j}{\rho_j C_{p,j}}\delta_\eta[B]^n\right]\Delta T^{n+\frac{2}{3}}=\Delta T^{n+\frac{1}{3}} \quad (6.14)$$

$$\left[1-\frac{J\Delta tk_j}{\rho_j C_{p,j}}\delta_\zeta[C]^n\right]\Delta T^{n+1}=\Delta T^{n+\frac{2}{3}}$$

Initial and Boundary Conditions

In the beginning of the simulation, the initial temperature in the composite volume can be set equal to a constant or can be a function of spatial position. In current study, the initial temperature is set equal to ambient temperature of freestream.

For all surface of the composite volume, Newton's law-of-cooling may be used to represent the required boundary condition. The convective heat transfer coefficient, h, was set to the desired values to represent standard convective heat transfer.

$$-k\left.\frac{\partial T}{\partial n}\right|_S=h(T_S-T_\infty) \quad (6.15)$$

The boundary conditions for two layers in perfect thermal contact require that the temperature and heat fluxes be continuous. Thus, the required temperature and flux conditions are:

$$T_1|_I=T_2|_I \quad (6.16)$$

$$k_1\left.\frac{\partial T}{\partial n_1}\right|_I=k_2\left.\frac{\partial T}{\partial n_2}\right|_I \quad (6.17)$$

6.2 Validation of a 3-D Heat Conduction Solver

6.2.1 Steady Simulations

Heat Transfer through an Insulated Wall

The developed 3-D heat conduction solver was validated for a heat transfer problem which has analytic solution. The problem is a heat transfer through an insulated wall [96]. Figure 6.1 shows details of the problem. The values for the brick and insulation thermal conductivity are:

$$k_{brick} = k_2 \quad = 0.7 \text{ W/mK}$$

$$k_{insulation} = k_1 = k_3 = 0.07 \text{ W/mK}$$

Figure 6.2 shows analytic solution for this problem. Temperatures at interfaces between brick and insulation are:

$$T_2 \quad = 90 \text{ °C} \qquad / \qquad T_3 \quad = 70 \text{ °C}$$

Figure 6.3 shows comparison of temperature distribution through an insulated wall. Present simulation shows good agreement with analytic solution. The solution was obtained on an 33 x 11 grid.

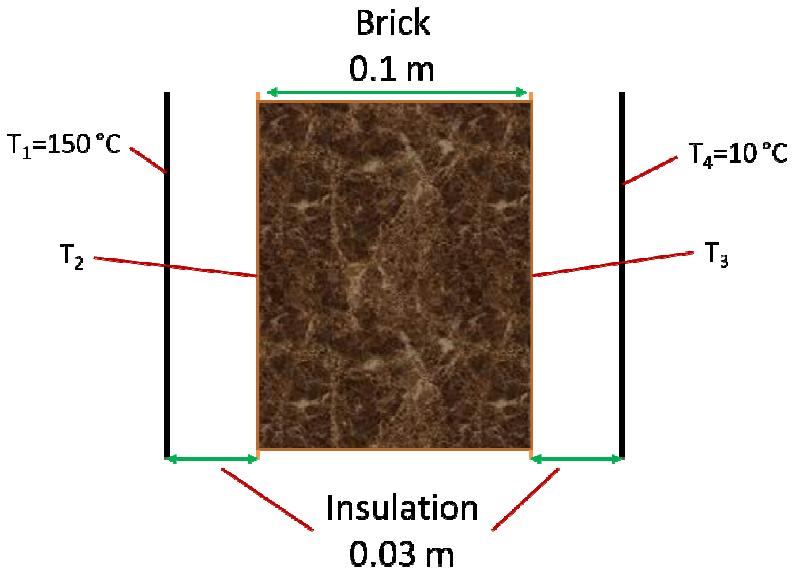

Figure 6.1: Heat Transfer through an Insulated Wall.

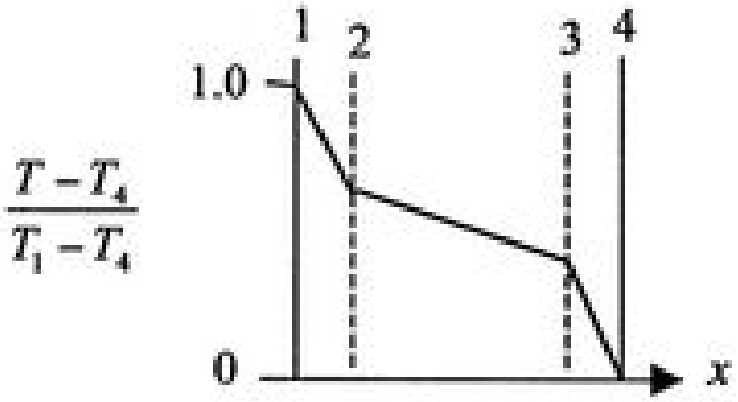

Figure 6.2: Analytic Solution for Heat Transfer through an Insulated Wall.

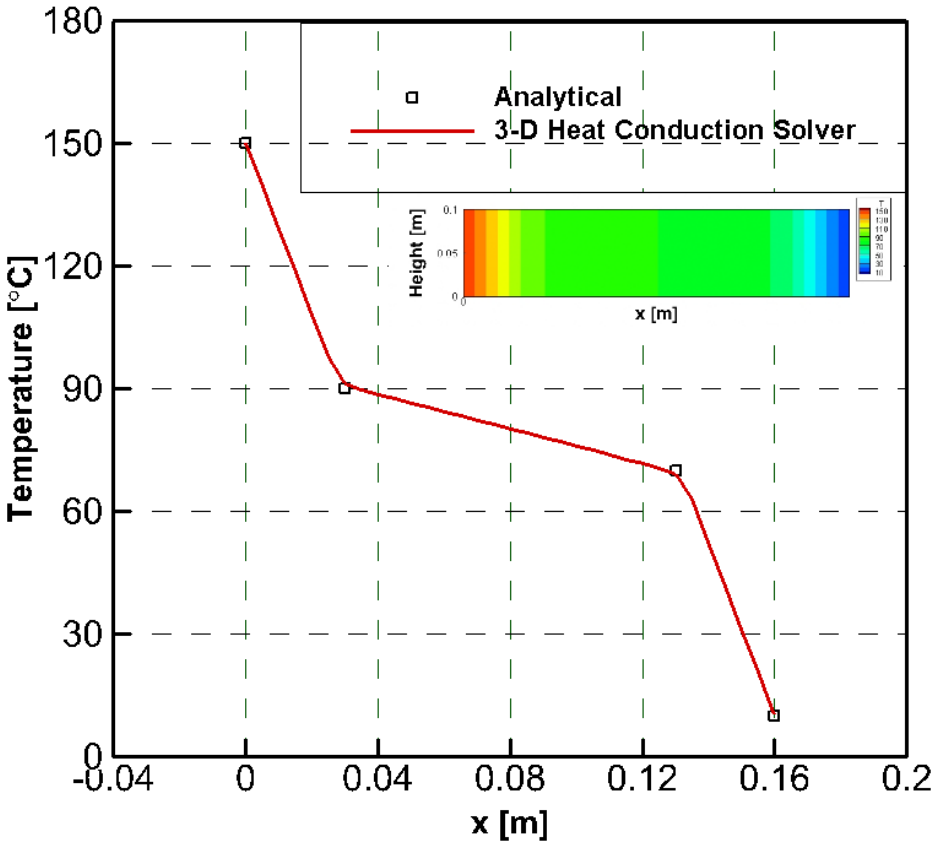

Figure 6.3: Solver Verification Results : Temperature Distribution through an Insulated Wall.

Heat transfer in Four Concentric Cylinders

As a next verification of a 3-D heat conduction solver, simulation has been done for steady state problem of four concentric cylinders [97]. The parameters used for this problem are shown in Table 6.1. The surface temperature of the inner cylinder was held at 1000 degrees C, while the surface temperature of the outer cylinder was fixed at 100 degrees C. The analytic solution at each interfaces are available (shown in Table 6.2). Figure 6.4 shows a graphical representation of the numerical solution. Present simulation shows good agreement with analytic solution. The solution was obtained on an 65 x 36 grid.

Table 6.1: Parameters used in the Multiple Zone Steady State Verification Problem

Layer	Inner Radius (mm)	Outer Radius (mm)	Thermal Conductivity K (KJ/hr m °C)
1	1000	800	155.77
2	800	700	249.23
3	700	500	18.69
4	500	300	93.46

Table 6.2: Analytic Solution for Heat Transfer in Four Concentric Cylinders

Interface	Temperature (°C)
1	100
2	173.25
3	196.0
4	815.1
5	1000

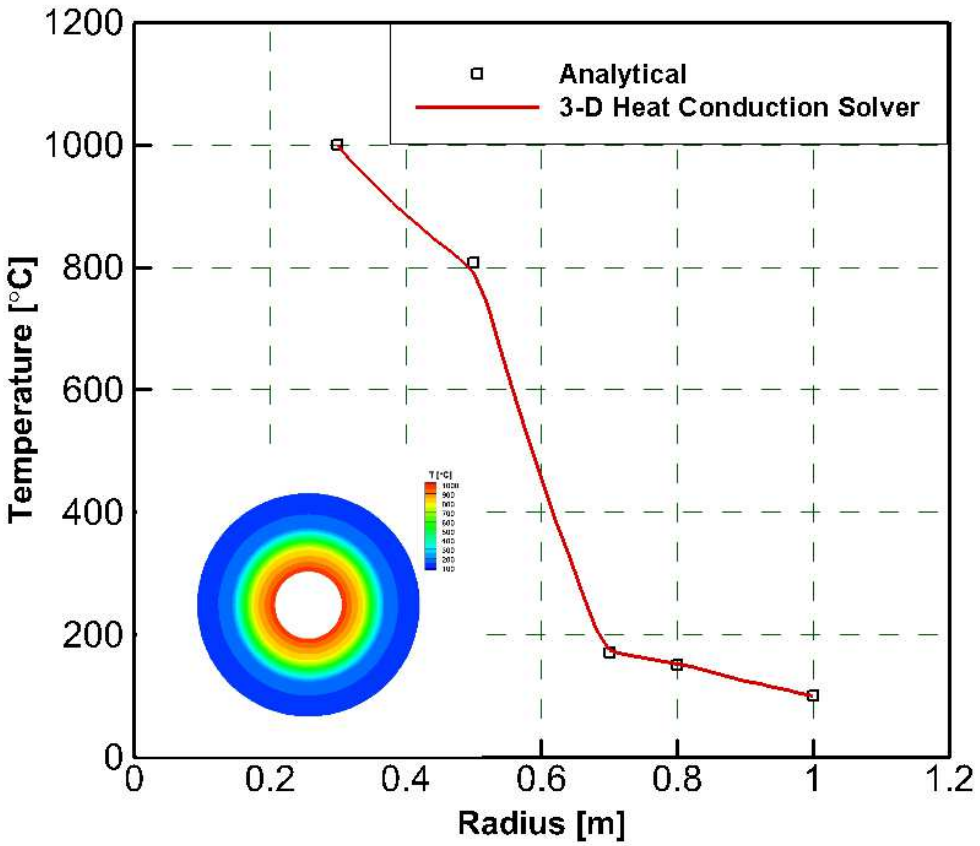

Figure 6.4: Solver Verification Results : Temperature Distribution in Four Concentric Cylinders.

6.2.2 Transient Simulations

Transient Heat Transfer

Simulation has been done for a 2-D transient heat transfer problem. The equation for this problem is:

$$\frac{\partial T}{\partial t} = \frac{\partial^2 T}{\partial x^2} + \frac{\partial^2 T}{\partial y^2} \quad (x, y) \in (0,1) \times (1,0)$$

The boundary conditions are:

$$T(0, y, t) = T(1, y, t) = 0, \quad y \in [0,1], \qquad t \geq 0$$

$$T(x, 0, t) = T(x, 1, t) = 0, \quad x \in [0,1], \qquad t \geq 0$$

The initial condition is:

$$T(x, y, 0) = \sin(\pi x) sin(2\pi y), \quad (x, y) \in (0,1) \times (1,0)$$

Figure 6.5 shows initial temperature distribution inside the domain. The analytic solution for this problem is:

$$T(x, y, t) = e^{-5\pi^2 t} \sin(\pi x) sin(2\pi y), \quad (x, y) \in (0,1) \times (1,0)$$

Figure 6.6 shows comparison of temperature distribution with analytic solution at different time. Present simulation shows good agreement with analytic solution. The solution was obtained on an 51 x 51 grid.

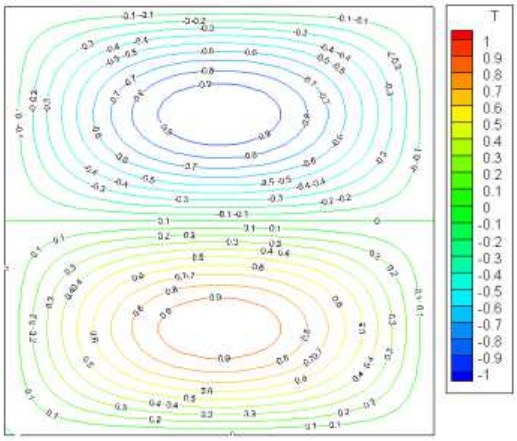

Figure 6.5: Initial Temperature Distribution inside the Domain.

Time	Analytical	3-D Heat Conduction Solver
0.01	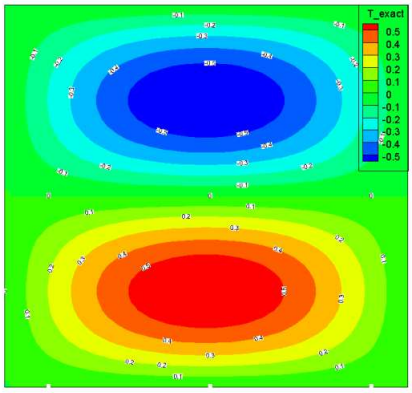	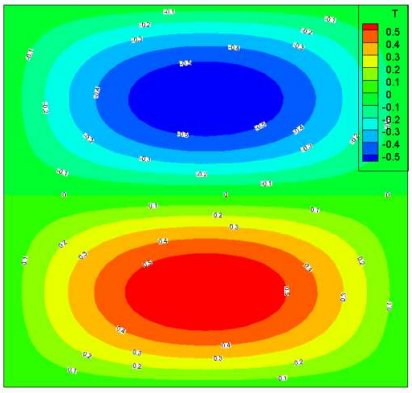
0.02	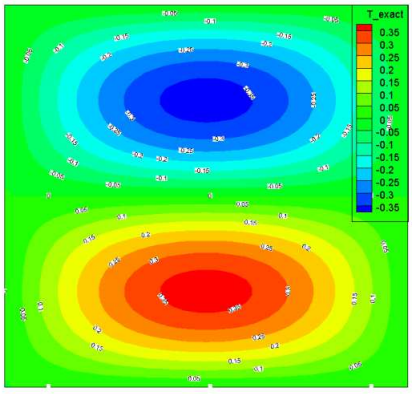	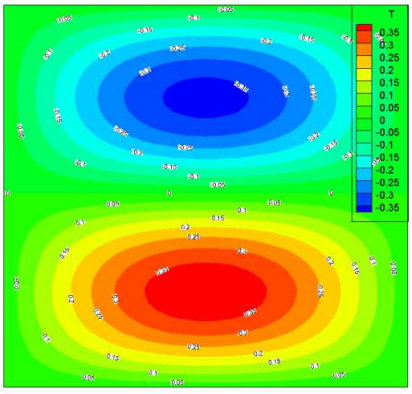

Figure 6.6: Solver Verification Results : Temperature Distribution inside the Domain.

Time Dependent Problem with Heat Source

Additional simulation has been done for a 2-D transient heat transfer problem with heat source. The equation for this problem is:

$$\frac{\partial T}{\partial t} = \frac{\partial^2 T}{\partial x^2} + \frac{\partial^2 T}{\partial y^2} + q \quad (x, y) \in (0,1) \times (1,0)$$

The boundary conditions are:

$$T(0, y, t) = T(1, y, t) = 0, \quad y \in [0,1], \qquad t \geq 0$$

$$T(x, 0, t) = T(x, 1, t) = 0, \quad x \in [0,1], \qquad t \geq 0$$

The initial condition is:

$$T(x, y, 0) = 0, \quad (x, y) \in (0,1) \times (1,0)$$

The heat source is:

$$q = \sin(\pi x) sin(\pi y), \quad (x, y) \in (0,1) \times (1,0)$$

The analytic solution for this problem is:

$$T(x, y, t) = \left(-\frac{1}{2\pi^2} e^{-2\pi^2 t} + \frac{1}{2\pi^2}\right) \sin(\pi x) sin(\pi y), \quad (x, y) \in (0,1) \times (1,0)$$

As noticed from the analytic solution, the temperature distribution reaches to steady state. Figure 6.7 shows comparison of steady state temperature distribution with analytic solution. Present simulation shows good agreement with analytic solution. For this problem simulations have been done with different size of grid and the effect of grid density on numerical error has been investigated. Figure 6.8 shows RMS error relative to analytic solution with different size of grid. The RMS error decreases linearly.

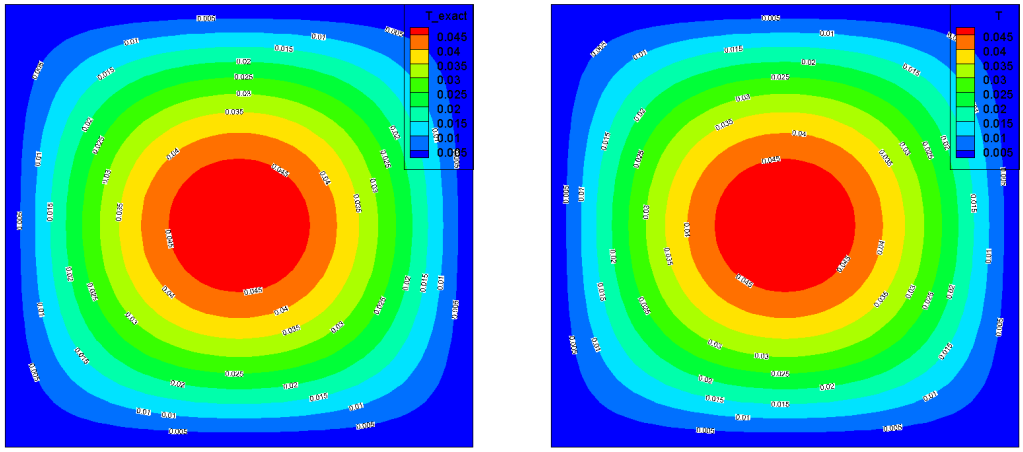

a) Analytic b) 3-D Heat Conduction Solver

Figure 6.7: Solver Verification Results : Temperature Distribution inside the Domain.

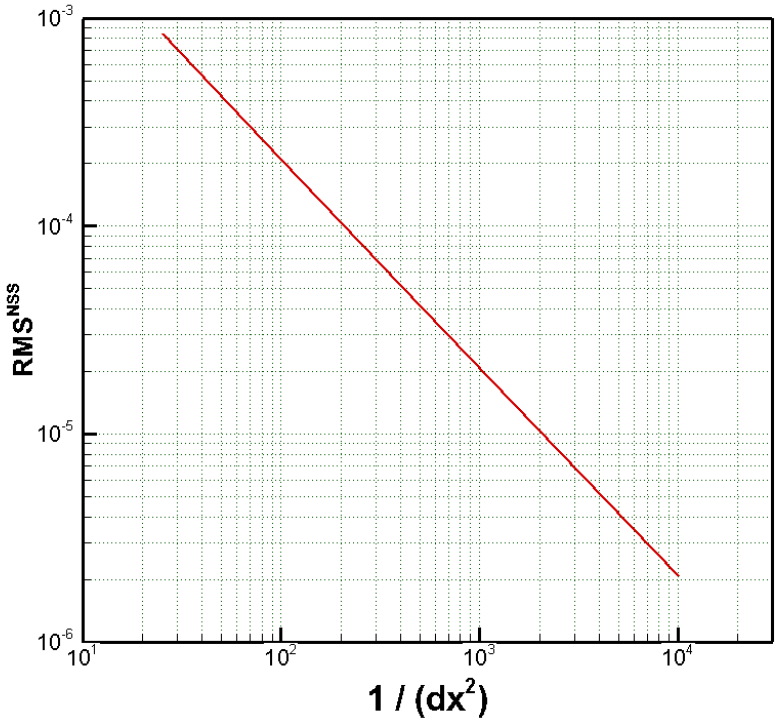

Figure 6.8: RMS Error Relative to Exact Time-dependent Solution.

6.3 Aerothermal Prediction for Rotor Blade

De-icing tests also have been done in NASA Glenn's Icing Research Tunnel (IRT) in 2013 [90-92]. In the present work, the aerothermal analysis also have been performed by LEWICE and an in-house 3D heat conduction solver developed by present investigator. LEWICE uses 2-D strip theory, and solves the heat conduction equations on a Cartesian grid. A fully 3-D heat conduction analysis that acknowledges curvature of the heat elements, and the finite spanwise extent of the heating elements has been developed.

6.3.1 Run33

One of test conditions, Run33, is selected as a baseline case. This condition is dry air case and used for the validation of the current aerothermal prediction module. Table 6.3 shows the corresponding test conditions. De-icing simulations have been done at 2D cross section, mid-span. Azimuthally averaged local velocity (210 ft/sec) and pitch angle (2.6 Deg.) are used as a flow condition. Convective boundary condition is applied at boundaries on computational geometry. Heat transfer coefficient (HTC) predicted from LEWICE is used as a boundary condition on external airfoil surface. Figure 6.9 shows predicted HTC for Run33. It also shows value of heat transfer coefficient at each temperature sensor (RTD) locations. Figure 6.10 shows cross section of heater zones and RTD locations. For the initial temperature, 54°F was used for all simulations instead of 45°F to account for the residual heat in the structure from the previous cycles. Comparison of blade surface temperature at different locations are seen in Fig. 6.11 and 6.12. At location B(leading edge region), LEWICE predicts temperature variation and peak value quite well. Unfortunately the in-house 3-D heat conduction code considering curvature effect under-predicted the peak value at external surface. One of reasons for this is due to the lack of modeling of aerodynamic heating in 3-D heat conduction code. LEWICE shows increase of surface temperature near leading edge region before the heater is turned on due to aerodynamic heating. Although current 3-D heat conduction

code shows under-prediction of surface temperature at leading edge region, it is physically meaningful to acknowledges curvature of the heat elements and the finite spanwise extent of the heating elements. At location C (downstream region), both analyses show similar temperature variation.

Table 6.3: Test Conditions for Run33

	Conditions
Forward Velocity (knot)	60
RPM	1200
Temperature (°F)	45
Time (Min)	5
Collective (Deg.)	5

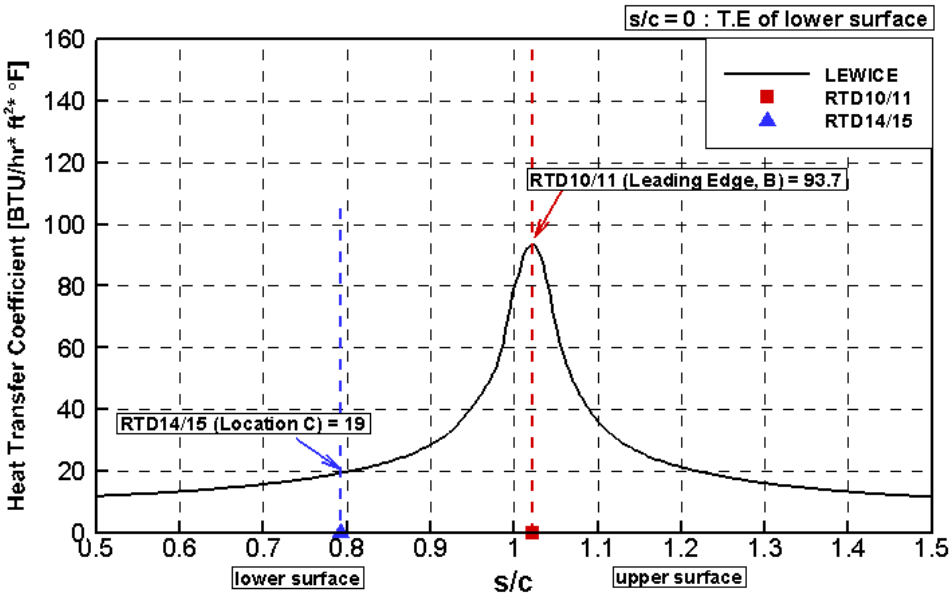

Figure 6.9: Predicted Heat Transfer Coefficient from LEWICE (Run33).

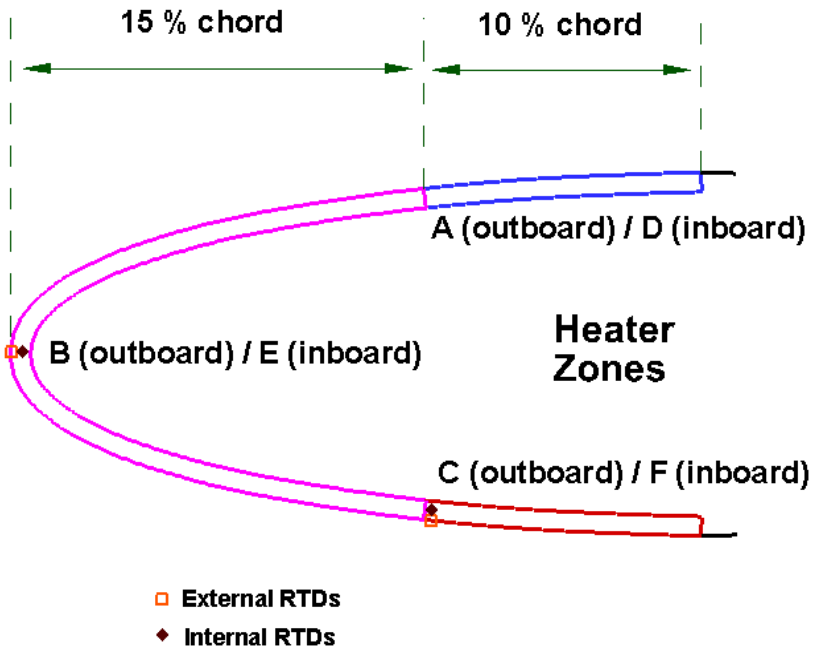

a) Cross section of heater zones

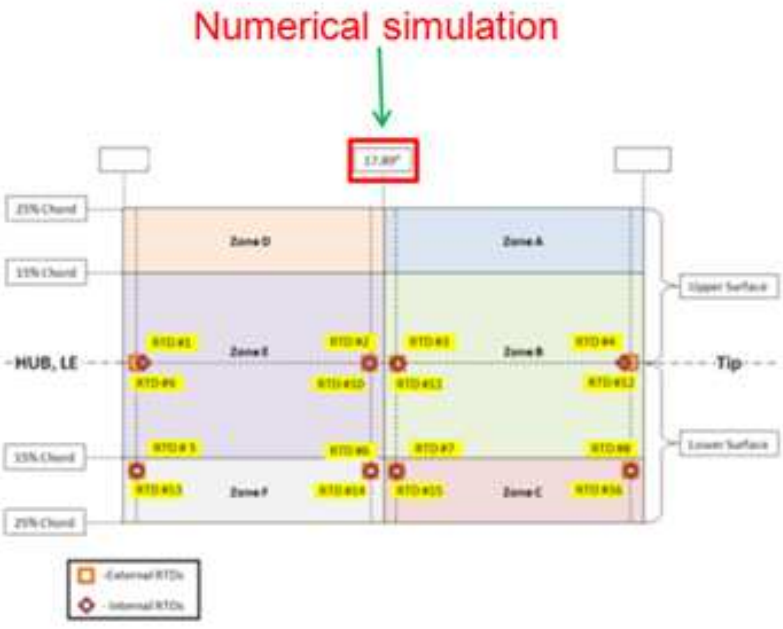

b) RTD locations

Figure 6.10: Heater Zone Layout (NASA Glenn's IRT).

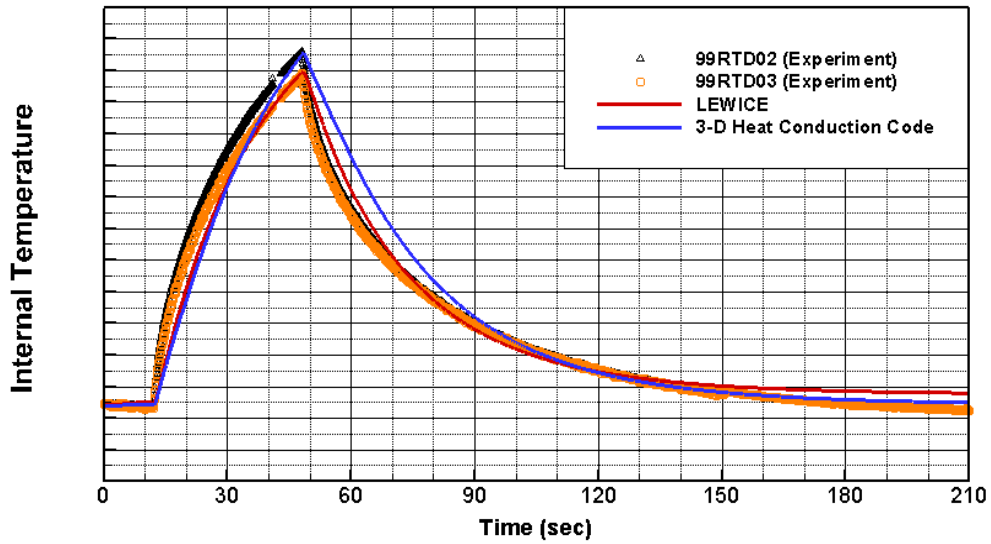

a) Internal

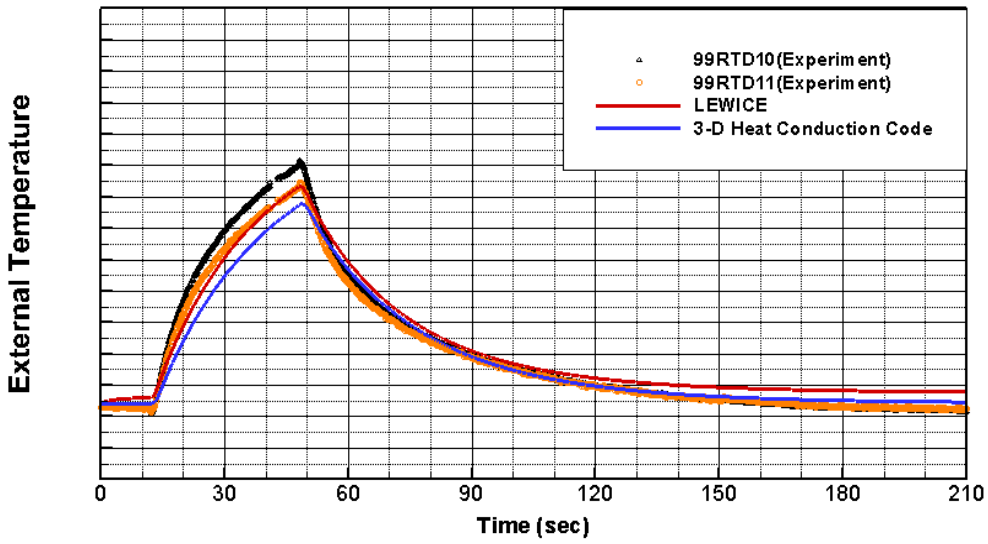

b) External

Figure 6.11: Comparison of Blade Surface Temperature at Location B.

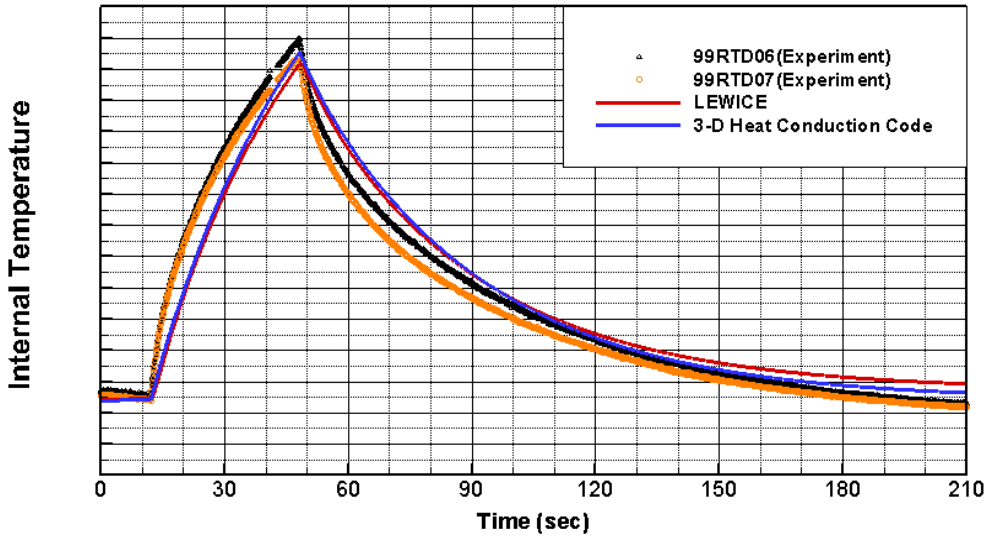

a) Internal

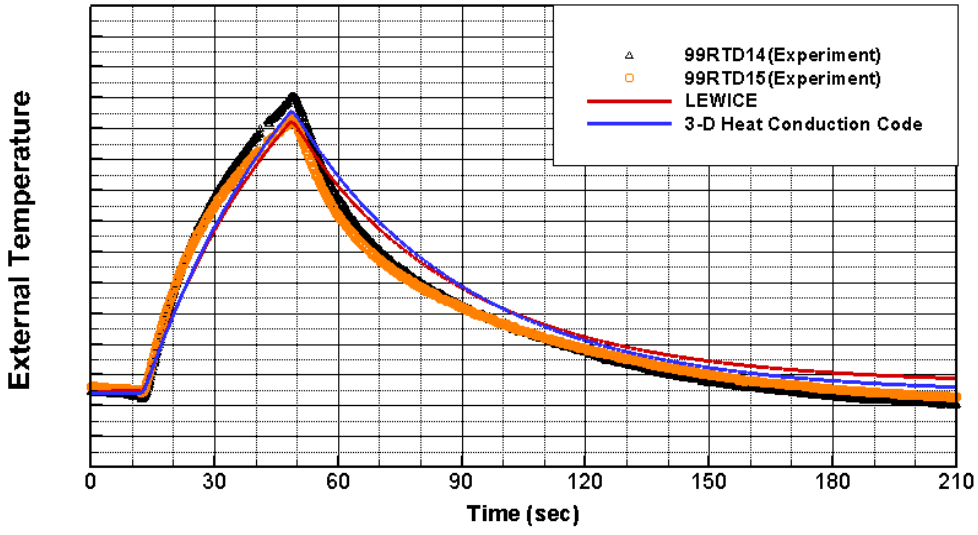

b) External

Figure 6.12: Comparison of Blade Surface Temperature at Location C.

6.3.2 Run40

De-icing simulations also have been performed for another test condition called Run40. Table 6.4 shows the corresponding test conditions. Like Run33, de-icing simulations have been done at 2D cross section, at mid-span (17.89 inch). Azimuthally averaged local velocity (327.85 ft/sec) and pitch angle (1.04 Deg.) are used as a flow condition. Convective boundary condition is applied at boundaries on computational geometry. Heat transfer coefficient (HTC) predicted from LEWICE is used as a boundary condition on external airfoil surface. Figure 6.13 shows predicted HTC for Run40. It also shows value of heat transfer coefficient at each temperature sensor (RTD) locations. For the initial temperature, 54°F was used for all simulations instead of 45°F to account for the residual heat in the structure from the previous cycles. Comparison of blade surface temperature at different locations are seen in Fig. 6.14 and 6.15. LEWICE shows reasonable peak temperature at location B (leading edge of airfoil) and location C (downstream region). Predictions from the 3-D heat conduction code also show reasonable peak temperature, except on the external surface at the leading edge. Unfortunately the in-house 3-D heat conduction code considering curvature effect under-predicted the peak value at external surface. One of reasons for this is due to the lack of modeling of aerodynamic heating in 3-D heat conduction code. LEWICE shows increase of surface temperature near leading edge region before the heater is turned on due to aerodynamic heating. Although current 3-D heat conduction code shows under-prediction of surface temperature at leading edge region, it is physically meaningful to acknowledges curvature of the heat elements and the finite spanwise extent of the heating elements.

Table 6.4: Test Conditions for Run40

	Conditions
Forward Velocity (knot)	105
RPM	2100
Temperature (°F)	45
Time (Min)	5
Collective (Deg.)	5

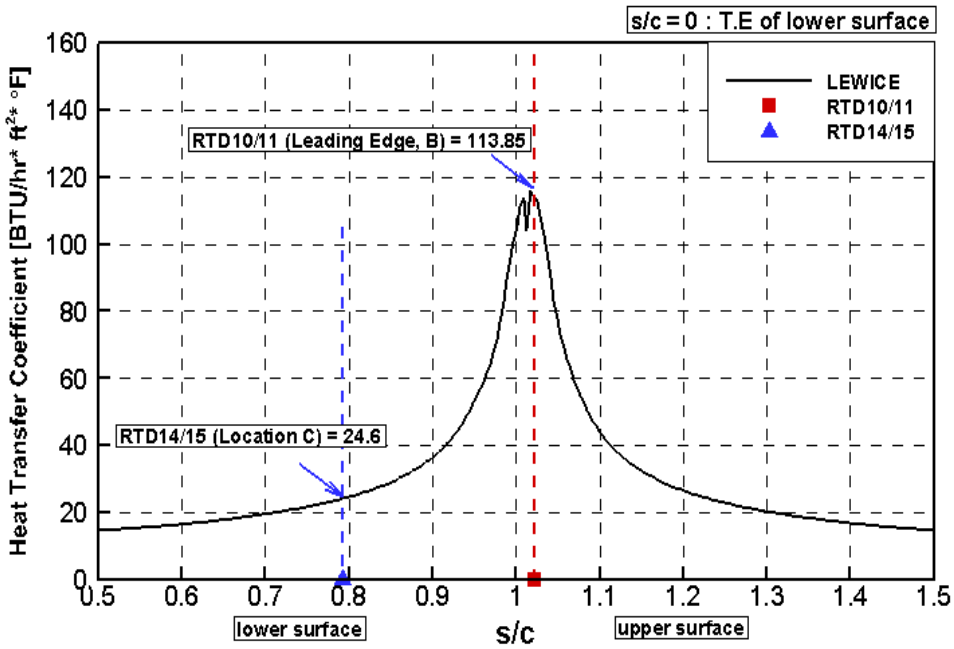

Figure 6.13: Predicted Heat Transfer Coefficient from LEWICE (Run40).

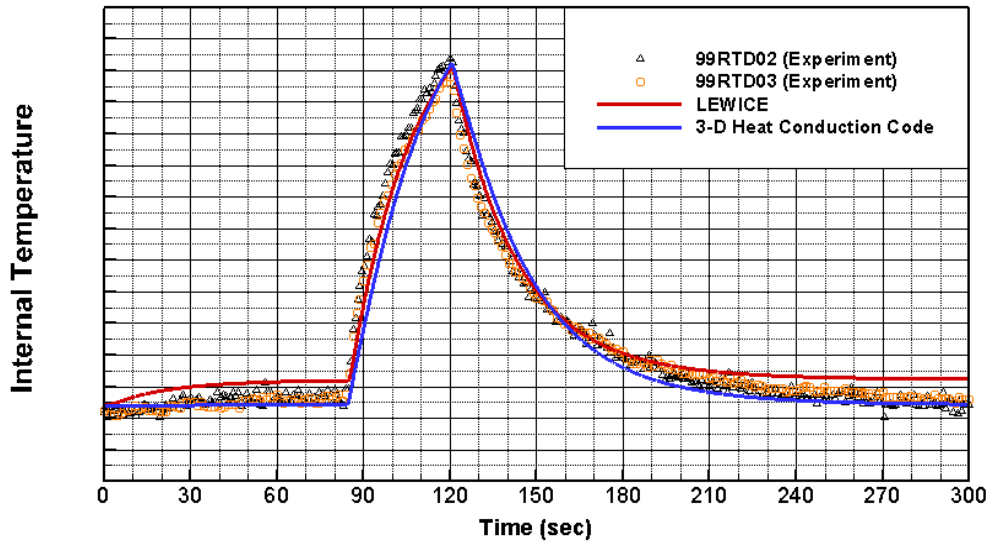

a) Internal

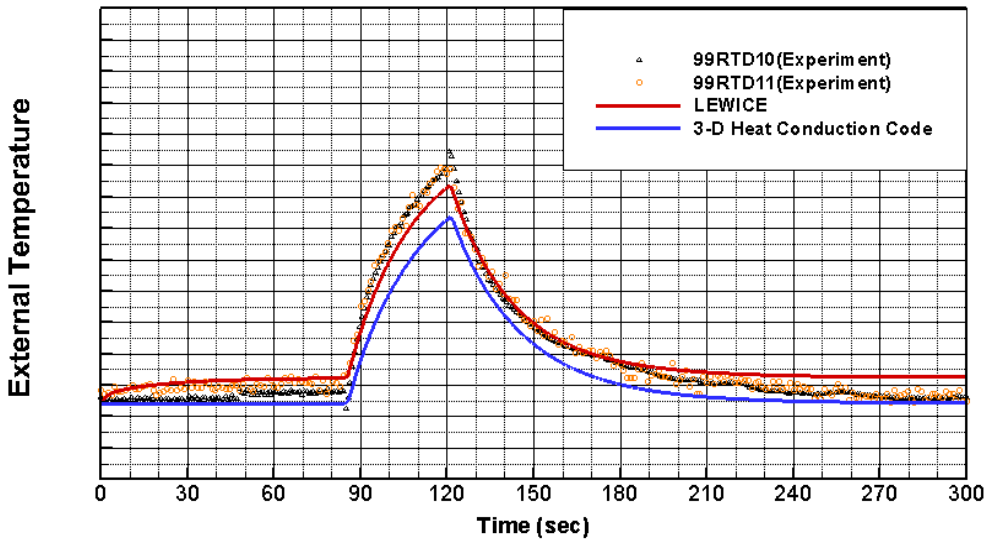

b) External

Figure 6.14: Comparison of Blade Surface Temperature at Location B.

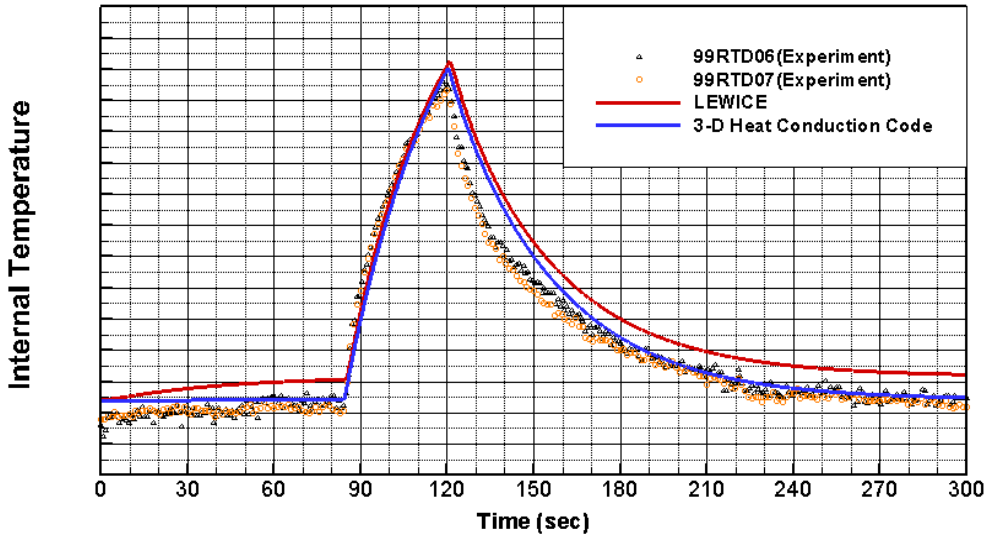

a) Internal

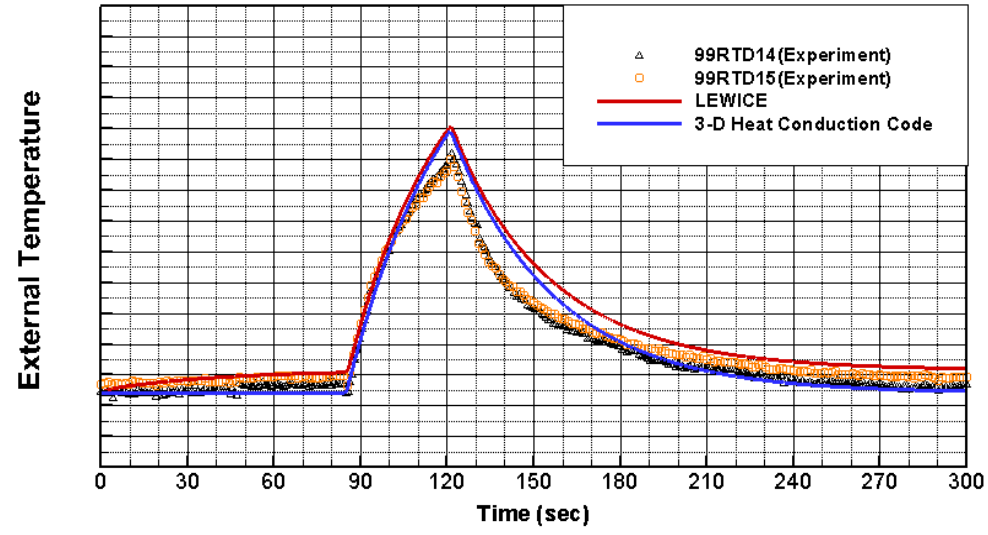

b) External

Figure 6.15: Comparison of Blade Surface Temperature at Location C.

CHAPTER 7

CONCLUSIONS AND RECOMMENDATIONS

A physics based methodology for the prediction of rotor blade ice formation has been developed and numerical studies for rotorcraft icing phenomena has been carried out to understand the fundamental phenomena of ice formation over rotorcraft airfoil sections. To this end, a series of progressively challenging simulations have been carried out. These include ability of the solvers to model airloads over an airfoil with a prescribed/simulated ice shape, collection efficiency modeling, ice growth, ice shedding, de-icing modeling, and assessment of the degradation of airfoil performance associated with the ice formation. Two different Navier-Stokes solvers, named GENCAS and GT-Hybrid, are used for the prediction of flowfield over 2-D airfoil and 3-D rotor blade. In order to compute the droplet flowfield properties at the same nodes of the discrete domain where the flow variables of air are known, a droplet solver, named GTDROP, based on an Eulerian approach has been developed. For the ice growth simulation, classical and extended Messinger models are used and numerical studies have been performed to systematically assess the difference between them. In this study, a Bell Helicopter Model 206B tail rotor blade (two-bladed teetering rotor) was used as a representative rotor.

The developed ice accretion module has been coupled with an empirical model for rotor blade ice shedding. A rotor configuration tested by Fortin was considered for ice shedding simulations.

Finally, the aerothermal analysis also have been performed by LEWICE and an in-house 3D heat conduction solver developed by the present author. LEWICE uses 2-D strip theory, and solves the heat conduction equations on a Cartesian grid. A fully 3-D heat conduction analysis that acknowledges curvature of the heat elements, and the finite spanwise extent of the heating elements has been developed. Conditions for aerothermal simulations were chosen from de-icing tests done in NASA Glenn's Icing Research Tunnel (IRT).

7.1 Conclusions

Based on the study, the following conclusions may be drawn:

1. 2-D static and oscillating airfoil simulations are done by GENCAS with the clean and simulated iced (SimIce) airfoils. Computational results are compared against experimental data. Performance degradation due to ice formation was captured reasonably.
2. A 3-D Eulerian based stand-alone solver has been validated for various benchmark cases. The present Eulerian based solver has been shown to successfully predict collection efficiencies on two-dimensional and three dimensional wing. The present approach is also in reasonable agreement to a well-validated Lagrangian code (LEWICE).
3. Ice accretion calculations have been done using the classical and extended Messinger model for rime and glaze ice conditions over 2-D airfoils. It was found that the Extended Messinger model predicts thicker ice near the leading edge of airfoil than classical Messinger model.

4. For 3-D rotor ice accretion, marginal difference in ice shape is seen at the inboard between the classical and extended Messinger models. Predicted ice shapes from both approaches are close to experimental ice shape at the inboard region.
5. Ice shapes start to differ towards blade tip. As seen in the 2D cases, the Extended Messinger model predicts thicker ice near the leading edge of airfoil. The predicted maximum ice thickness from the Extended Messinger model is closer to measurements.
6. In the tip region of helicopter blades at high speed, the effect of kinetic heating affect ice accretion process. In order to consider kinetic heating effect, blade surface temperature distributions which are predicted from CFD simulation were fed into Extended Messinger model. There is marginal difference in predicted ice shape at the inboard. However, improvement on the prediction of ice shape is seen in the tip region by considering kinetic heating effect.
7. Performance predictions for clean rotor, measured and predicted ice shape from the Extended Messinger model have been done to investigate the effect of ice formation on rotor performance. Only the computed and measured thrust values are in reasonable agreement. The predicted power is much lower than experiment. One of possible reason for this discrepancy is the lack of surface roughness modeling in the CFD solver. The performance degradation of the iced rotor compared to clean rotor is only qualitatively captured.
8. From rotor blade ice shedding simulations, it is found that reasonably good agreement was predicted for properties, such as the length of the shed ice and the time at which shedding occurs.
9. An in-house 3D heat conduction solver that acknowledges curvature of the heat elements has been developed and validated for various benchmark cases. The present in-house 3D heat conduction solver has been shown to successfully predict

temperature distribution inside two-dimensional composite airfoils. The present approach is also in reasonable agreement to a well-validated code (LEWICE).

10. While current results are encouraging, much additional work remains in modeling detailed physics important to rotorcraft icing phenomena. Despite these difficulties, progress in assessing helicopter ice accretion has been made and tools for initial analyses have been developed.

7.2 Recommendations

Based on the study, the following recommendations are mode for further research:

1. Ice accretion simulations on 3-D body have been done based on 3-D unsteady flowfield and water droplet analysis. However, ice growth is still done based on 2-D strip approach. Extension from 2-D to 3-D ice accretion modeling should be pursued.
2. Estimation of convective heat transfer coefficient is still based on empirical formulation using Reynolds analogy. Approach using high fidelity CFD analysis should be further investigated.
3. Degraded performance prediction due to ice formation was qualitatively captured. Surface roughness modeling in the CFD solver should be considered.
4. Although the current rotor blade ice shedding model shows reasonably good agreement with measurements, this empirical model requires input from actual experiments on ice shedding to determine shear stresses. The methodology does not use fracture mechanics. Further study on the modeling of ice shedding is recommended.
5. In present study, external ice layer was not considered in de-icing simulations. External ice layer and phase change inside ice layer should be considered.

APPENDIX A

ENERGY TERMS

The energy terms appearing in the extended Messinger model equations are expressed:

- Convective heat transfer (Q_c)

$$Q_c = h_c(T_s - T_a) \tag{A.1}$$

- Cooling by incoming droplets (Q_d)

$$Q_d = (LWC)\beta V_\infty C_{pw} h_c(T_s - T_a) \tag{A.2}$$

- Evaporative hat loss (Q_e)

$$Q_e = \chi_e e_0(T_s - T_a) \tag{A.3}$$

$$\chi_e = \frac{0.622 h_c L_E}{C_p P_t Le^{2/3}}, \qquad e_0=27.03, \qquad P_t = \text{total pressure of the airflow}$$

- Sublimation hat loss (Q_s)

$$Q_e = \chi_s e_0(T_s - T_a) \tag{A.4}$$

$$\chi_s = \frac{0.622 h_c L_S}{C_p P_t Le^{2/3}}$$

- Radiation (Q_r)

$$Q_r = 4\varepsilon\sigma_r T_a^3(T_s - T_a) \tag{A.5}$$

ε : Surface emissivity, σ_r : Stefan-Boltzmann constant

- Aerodynamic heating (Q_a)

$$Q_a = \frac{r h_c V_\infty^2}{2C_p} \tag{A.6}$$

r: Adiabatic recovery factor ($r=Pr^{1/2}$ for laminar flow, $r=Pr^{1/3}$ for turbulent flow)

- Kinetic energy of incoming droplets (Q_k)

$$Q_k = (LWC)\beta V_\infty \frac{V_\infty^2}{2} \tag{A.7}$$

- Heat brought in by runback water (Q_{in})

$$Q_{in} = \dot{m}_{in} C_{pw} (T_f - T_s) \tag{A.8}$$

- Latent heat release (Q_l)

$$Q_l = \rho_r L_F \frac{\partial B}{\partial t} \tag{A.9}$$

APPENDIX B

PARAMETER VALUES USED IN THE ICING CALCULATIONS

The parameter values used in the icing calculations are:

Symbol	Description	Value	Units
C_p	Specific heat of air	1006	J/Kg K
C_{pi}	Specific heat of ice	2050	J/Kg K
C_{pw}	Specific heat of water	4218	J/Kg K
e_0	Saturation vapor pressure constant	27.03	
g	Gravitational acceleration	9.81	m/s^2
k_i	Thermal conductivity of ice	2.18	W/m K
k_w	Thermal conductivity of water	0.571	W/m K
Le	Lewis number	1/Pr	
L_F	Latent heat of solidification	3.344×10^5	J/Kg
L_E	Latent heat of vaporization	2.50×10^6	J/Kg
L_S	Latent heat of sublimation	2.8344×10^6	J/Kg
Pr	Laminar Prandtl number of air	0.72	
Pr_t	Turbulent Prandtl number of air	0.9	
ε	Radiative surface emissivity of ice	0.5 - 0.8	
μ_w	Viscosity of water	1.795×10^{-3}	Pa s
ρ_r	Density of rime ice	880	Kg/m^3
ρ_g	Density of glaze ice	917	Kg/m^3
ρ_w	Density of water	999	Kg/m^3
σ_r	Stefan-Boltzmann constant	5.6704×10^{-8}	
σ_w	Surface tension of water	0.072	N/m

REFERENCES

[1] AGARD-AR-344, “Ice Accretion Simulation,” Advisory Group of Aerospace Research and Development (AGARD), NATO, 1997.

[2] Gent, R.W., Dart, N.P. and Cansdale, J.T., “Aircraft Icing”. *Phil. Trans. R. Soc. Lond.*, Vol. 358, 2000, pp.2873-2911.

[3] Potapczuk, M. G., and Reinmann, J. J., “Icing Simulation: A Survey of Computer Models and Experimental Facilities,” AGARD, Effects of Adverse Weather on Aerodynamics, 1991.

[4] Hardy, J. K. , “Protection of aircraft against ice,” RAE Report SME 3380, 1946.

[5] Messinger, B. L., “Equilibrium temperature on an unheated icing surface as a function of airspeed,” *J. Aeronautical Sci.* Vol. 20, 1953, pp. 29-41.

[6] Langmuir, I. and Blodgett, K. B., “A mathematical investigation of water droplet trajectories,” Army Air Forces Technical Report 5418, 1946.

[7] Harold E. Addy, Andy P. Broeren, Joseph G. Zoeckler, and Sam Lee," A Wind Tunnel Study of Icing Effects on a Business Jet Airfoil," NASA TM-2003-212124.

[8] Gurbacki, H. M. and Bragg, M. B., "Unsteady Aerodynamic Measurments on an Iced Airfoil," 40th AIAA Aerospace Sciences Meeting and Exhibit , AIAA 2002-9241.

[9] Kumar, Satish and Loth, Eric, "Aerodynamic Simulations of Airfoils with Upper-Surface Ice-Shapes," Journal of Aircraft, 2001, Vol. 38, 2001.

[10] Miller T. L. and Bond T. H., "Icing Research Tunnel Test of a Model Helicopter Rotor," NASA/TM-101978, 1989.

[11] Shaw, Robert J. and Richter, G. Paul., "The UH-1H Helicopter Icing Flight Test Program: An Overview," 23rd Aerospace Sciences Meeting, AIAA 1985-338, 1985.

[12] "Inflight Icing and the Helicopter," Flight Saftey Foundation Helicopter Saftey. November/December, Vol. 16, 6, 1990.

[13] Guffond D. P., "Icing and Deicing Test on a ¼ Scale Rotor in the ONERA SIMA Wind Tunnel," AIAA 24th Aerospace Science Meeting, January 6-9, Reno, Nevada, 1986.

[14] Lee, John D., Harding, Rorry and Palko, Richard L. “Documentation of Ice Shapes on the Main Rotor of a UH-1H Helicopter in Hover”. NASA CR 168332, 1984.

[15] Miller T. L. and Bond T. H., "Icing Research Tunnel Test of a Model Helicopter Rotor," NASA/TM-101978, 1989.

[16] Bond T. H., Flemming R. J. and Britton R. K., "Icing Tests of a Model Main Rotor, " AMS, Annual Forum 46th Washington, DC, USA, 1990.

[17] Flemming R., Britton R. K. and Bond T. H, "Model Rotor Icing Test in the NASA Lewis Icing Research Tunnel," NASA/TM-104351, 1991.

[18] Korkan K., "Experimental Study of Performance Degradation of a Rotating System in the NASA Lewis RC Icing Tunnel," NASA/CR-190684, 1991.

[19] Flemming R., Bond T. H. and Britton R. K., "Results of a Sub-Scale Model Rotor Icing Test," NASA/TM-103709, 1991.

[20] Britton R. K. and Bond T. H., "A Review of Ice Accretion Data from a Model Rotor Icing Test and Comparison with Theory," NASA/TM-103712 and AIAA-91-0661, 1991.

[21] Fortin, G. and Perron, J., “Spinning Rotor Blade Tests in Icing Wind Tunnel” Paper AIAA 2009-4260, 1st AIAA Atmospheric and Space Environments Conference, San Antonio, TX, 2009.

[22] E. W. Brouwers, J. L. Palacios, E. C. Smith, A. A. Peterson, "The experimental investigation of a rotor hover icing model with shedding," AHS 66th Annual Forum and Technology Display, Phoenix, USA, 2010.

[23] Wright, W. B., “User Manual for LEWICE Ver. 3.2,” NASA CR 214255, Cleveland, OH, 2008.

[24] GUFFOND, D.; BRUNET, L., "Validation du programme bidimensionnel de capitation," Châtillon Cedex, France: Office National D'Études et de Recherches Aérospatiales, 1988.

[25] HENRY, R. "Development of an electrothermal de-icing/anti-icing model," Chatillon Cedex: Office National d'Etudes et de Recherches Aérospatiales, 1992.

[26] E. Montreuil, A. Chazottes and D. Guffond, A. Murrone, F. Caminade, and S. Catris, " Enhancement of Prediction Capability in Icing Accretion and related Performance Penalties Part I: Three-dimensional CFD Prediction of the Ice Accretion," Paper AIAA 2009-3969, 1st AIAA Atmospheric and Space Environments Conference, San Antonio, Texas, 2009.

[27] Beaugendre, H., Morency, F., and Habashi, W., "FENSAP-ICE's Three-Dimensional In-Flight Ice Accretion Module: ICE3D," Journal of Aircraft, Vol. 40 No.2, 2003.

[28] MORENCY, F.; TEZOK, F.; PARASCHIVOIU, I. "Anti-icing system simulation using CANICE," Journal of Aircraft, v. 36, n. 6, 1999.

[29] S. Gouttebroze, F. Saeed and I. Paraschivoiu, "CANICE- Capabilities and current tatus," in *NATAO/RTO Workshop, Assessment of icing code prediction capabilities*, CIRA, Capua, Italy, December 2000.

[30] CEBECI, T. "Calculation of Compressible Turbulent Boundary Layers with Heat and Mass Transfer," AIAA Journal, vol. 9, n. 6, p. 1091–7,1971.

[31] CHEN, K. K. and THYSON, N. A., "Extension of Emmon's Spot Theory to Flows on Blunt Bodies," AIAA Journal, vol. 9, n. 5, 1971.

[32] MICHEL, R. "Etude de la transition sur les profiles d'aile. Establissement d'un critére de Determination de Point de Transition et Calcul de la Trainee de Profile Incompressible," Chatillon Cedex: Office National D'Études et de Recherches Aérospatiales, 1951.

[33] da Silveira, R. A., Maliska, C. R., Estivam, D. A., and Mendes, R., "Evaluation of Collection Efficiency Methods for Icing Analysis," Proceedings of COBEM 2003, 2003.

[34] Bidwell, C. S. and Potapczuk, M. G., "Users Manual for the NASA Lewis Three-Dimensional Ice Accretion Code (LEWICE3D)," Tech. Report, NASA Glenn Research Center, 1993.

[35] Wright, W. B., "LEWICE 2.2 Capabilities and Thermal Validation," AIAA Paper 2002-0383, 2002.

[36] Bourgault, Y., Boutanios, Z., and Habashi, W. G., "Three-Dimensional Eulerian Approaches to Droplet Impingement Simulations Using FENSAP-ICE, Part 1: Model, Algorithm, and Validation," Journal of Aircraft, Vol. 37 No.1, 2000.

[37] Hill, J. M., *One-Dimensional Stefan Problems: An Introduction*, Longman Science Technical, Harlow, England, U.K., 1987, Chap. 1.

[38] Huang, J. R., Keith, T. G., Jr., and De Witt, K. J., "Ef. cient Finite Element Method for Aircraft De-Icing Problems," *Journal of Aircraft*, Vol.30, No. 5, 1993, pp. 695–704.

[39] Myers T. G. "Extension to the Messinger Model for Aircraft Icing." AIAA J Journal of Aircraft, Vol. 39 No.2, 2001.

[40] Thomas Reid, Guido S. Baruzzi, and Wagdi G. Habashi. "FENSAP-ICE: Unsteady Conjugate Heat Transfer Simulation of Electrothermal De-Icing", Journal of Aircraft, Vol. 49, No. 4, 2012.

[41] Wright, W. B., Keith, T. G., and DeWitt, "Numerical Simulation of Icing, Deicing, and Shedding," AIAA Paper 91-0665, 1991.

[42] DeWitt, K. J., Keith, T. J., Chao, D. F., and Masiulaniec, K. C., "Numerical Simulation of Electrothermal De-Icing Systems," AIAA Paper 83-0114, 1983.

[43] Leffel, K. L., "A Numerical and Experimental Investigation of Electrothermal Aircraft Deicing," NASA CR-175024, 1986.

[44] Masiulaniec, K. C., "A Numerical Simulation of the Full Two-Dimensional Electrothermal Deicer Pad," Ph.D. Thesis, Univ. of Toledo, Toledo, OH, 1987.

[45] Huang, J. R., “Numerical Simulation of an Electrothermally Deiced Aircraft Surface Using the Finite Element Method,” AIAA Paper 91-0268, 1991.

[46] Stallabrass, J. R., 'Thermal Aspects of Deicer Design," presented at the International Helicopter Icing Conference, Ottawa, Canada, 1972.

[47] Baliga, G., "Numerical Simulation of One- Dimensional Heat Transfer in Composite Bodies with Phase Change," M.Sc. Thesis, University of Toledo, Toledo, Ohio, 1980.

[48] Marano, J. J., "Numerical Simulation of an Electrothermal Deicer Pad," M.Sc. Thesis, University of Toledo, Toledo, Ohio, May 1982.

[49] Gent, R. W. and J. T. Cansdale, "One- Dimensional Treatment of Thermal Transients in Eleceically Deiced Helicopter Rotor Blades," RAE TR 80159,1980.

[50] Roelke, R. J., "A Rapid Computational Procedure for the Numerical Solution of a Heat Flow Problem with Phase Change," M.Sc. Thesis, University of Toledo, Toledo, Ohio, August 1986.

[51] Flemming, Robert J. and Lednicer, David A. "High Speed Ice Accretion on Rotorcraft Airfoils," NASA CR 3910 1985.

[52] Britton, Randall K, "Ongoing Development of a Computer Jobstream to Predict Helicopter Main Rotor Performance in Icing Condition," NASA CR 187076, 1991.

[53] Britton, Randall K, "Development of an Analytical Method to Predict Helicopter Main Rotor Performance in Icing Condition," NASA CR 189110, 1992.

[54] Cebeci, T., "Calculation of Flow Over Iced Airfoils," AIAA Journal, Vol. 27, 1989, pp. 853-861.

[55] G.Zanazzi, G.Mingione, A. Pagano, A. Visingardi, "Ice Accretion Prediction on Helicopter Rotor Blade in Hover Flight," SAE Aricraft and Engine Icing International Conference, SAE Paper 2007-01-3309, 2007.

[56] Bain, J., Sankar, L. N., Nucci, M., Egolf, A., and Flemming, R. J., “A Methodology for Modeling the Effects of Icing on Rotary Wing Aerodynamics,” Proceedings of the 2010 European Rotorcraft Forum, September 2010.

[57] Rajmohan, N., Bain, J, Nucci, M., Sankar, L., Flemming, R. J., Egolf, A., Kreeger, R., " Icing Studies for the UH-60A Rotor in Forward Flight," Proceedings of AHS Aeromechanics Specialists’ Conference, Jan 20-22, 2010.

[58] Bain, J., Sankar, L. N.,Deresz, R., Egolf, T. A., Flemming, R. J., and Kreeger, R., “Effects of Icing on Rotary Wing Loads and Surface Heat Transfer Rates,” AIAA-2011-1100, 49th AIAA Aerospace Sciences Meeting including the New Horizons Forum and Aerospace Exposition, Orlando, Florida, Jan. 4-7, 2011.

[59] Bain, J., Sankar, L. N., Garza, D., Aubert, R. J., and Flemming, R. J., “A Methodology for the Prediction of Rotor Blade Ice Formation and Shedding,” Proceedings of the SAE 2011 Aircraft and Engine icing and Ground Testing Conference, June 13-17, 2011.

[60] Narducci, R. and Kreeger, R., "Analysis of a Hovering Rotor in Icing Conditions," Proceedings of American Helicopter Society 66th Annual Forum, 2010.

[61] Narducci, R., Orr, s. and Kreeger, R., "Application of a High-Fidelity Icing Analysis Method to a Model-Scale Rotor in Forward Flight," Proceedings of American Helicopter Society 67th Annual Forum, 2011.

[62] Scavuzzo, R.J., Chu, M.L., and Kellackey, C.J.; “Impact Ice Stresses in Rotating Airfoils.” AIAA-90-0198, 28th Aerospace Sciences Meeting, January, 1990.

[63] Scavuzzo, R.J., Chu, M.L., and Kellackey, C.J.; “Impact Ice Stresses in Rotating Airfoils.” J. Aircraft, Vol. 28, No. 7, 1990.

[64] Ozgen S., Canibek M., “Ice accretion simulation on multi-element airfoils using extended Messinger model,” Heat and Mass Transfer, Vol. 45, 2009 pp. 305-322.

[65] Min, B. Y., Lee, W., Englar, R. and Sankar, L. N., “Numerical Investigation of Circulation Control Airfoils,” Journal of Aircraft, vol. 46, No. 4, pp. 1403-1410, 2009.

[66] Min, B. Y., " A physics based investigation of gurney flaps for enhancement of rotorcraft flight characteristics", PhD Thesis, Georgia Institute of Technology, Atlanta, GA, 2010.

[67] Rajmohan, N., "Application of Hybrid Methodology to Rotors in Steady and Maneuvering Flight", Ph.D. Dissertation, Georgia Institute of Technology, 2010.

[68] Marpu R. P., Sankar L.N., Makinen S., Egolf T.A., Baeder J.D. and Wasikowski, M., "Physics Based Modeling of Maneuver Loads for Rotor and Hub Design," Journal of Aircraft, 2014.

[69] Michaelides, E. E., *Particles, Bubbles & Drops: Their Motion, Heat and Mass Transfer*, World Scientific Publishing Company, April 2006.

[70] M. Papadakis, K. E. Hung, G. T. Vu, H. Wei Yeong, C. S. Bidwell, M. D. Breer, and T. J. Bencic, "Experimental Investigation of Water Droplet Impingement on Airfoils, Finite Wings, and an S-Duct Engine Inlet," NASA, TM—2002-211700, October 2002.

[71]J. L. Hess and A. M. O. Smith, "Calculation of potential flow about arbitrary bodies," *Progress in Aeronautical Sciences*, vol. 8, pp. 1-138, 1967.

[72] W. Frost, H. Chang, C. Shieh and K. Kimble, "Two-dimensional particle trajectory computer program," Interim Report for Contract NAS3-22448, 1982.

[73] Wenzinger CJ, "Pressure distribution over an NACA 23012 airfoil with an NACA 23012 external-airfoil flap", NACA Report No. 614, 1937.

[74] Schlichting H., "Boundary layer theory," 7th edition. McGraw-Hill, New York, 1979.

[75] Thawites, B., "Incompressible Aerodynamics," Clarendon Press, Oxford, 1960.

[76] Gent, R.W., Dart, N.P., Cansdale JT,"Aircraft icing", Phil. Trans R Soc. Lond. A 358:2873–2911, 2000.

[77] Carslaw, H. S., and Jaeger, J. C., *Conduction of Heat in Solids*, Clarendon, Oxford, 1959, p. 19.

[78] Flemming, R. J., et al., "Oscillating Airfoil Icing Tests in the NASA Glenn Research Center Icing Research Tunnel," SAE/AIAA/AHS International Conference on Aircraft and Engine Icing and Ground Deicing, SAE 2011-38-0016, 2011.

[79] Lorber, P., Flemming, R. J., O′Neill, J., Narducci, R., Reinert, T., Sankar, L. N. and Kim, J. W., " Oscillating Iced Airfoil Pressure Measurement and Computation," AHS 69th Annual Forum and Technology Display, Phoenix, USA, 2013.

[80] Kim, J. W., Sankar, L. N., Marpu, R., Egolf, T. A., and Hariharan, N., " Assessment of Planform Effects on Rotor Hover Performance," 53rd AIAA Aerospace Sciences Meeting, 2015.

[81] Cross, J. F. and Tu, W., "Tabulation of Data from the Tip Aerodynamics and Acoustics Test," NSA TM 102280, Nov., 1990.

[82] Yang, Z., Sankar, L. N., Smith, M. and Bauchau, O., "Recent Improvements to a Hybrid Method for Rotors in Forward Flight," Journal of Aircraft, Vol. 39, No 5, 2002, pp.804~812.

[83] Michael P. Kinzel, Christian M. Sarofeen, Ralph W. Noack, Richard E. Kreeger, "A Finite-Volume Approach to Modeling Ice Accretion," AIAA Paper 2010-4230, June 2010.

[84] H. Beaugendre, F. Morency and W.G. Habashi, "Development of a Second Generation In-flight Icing code", *ASME Journal of Fluids Engineering*, March 2006.

[85] Olsen W., Shaw R., Newton J., "Ice Shapes and the resulting drag increase for a NACA 0012 airfoil", NASA TM-835556, 1994.

[86] Wright, W. B., and Rutkowski, A., "Validation Results for LEWICE 2.0", NASA CR 1999208690, 1999.

[87] Korkan, K.D., Dadone, L., and Shaw, R.J., "Performance Degradation of Helicopter Rotor Systems in Forward Flight Due to Rime Ice Accretion," AIAA Paper 83-0029, January, 1983.

[88] Anderson, D. N., "Further evaluation of traditional icing scaling methods", AIAA-96-0633, January1996.

[89] Anderson, D. N. and Ruff, G.A., “Evaluation of Methods to Select Scale Velocities in Icing Scaling Tests”, AIAA-99-0244, January 1999.

[90] Kreeger, R. E. And Tsao, J., “Ice Shapes on a Tail rotor,” AIAA Paper 2014-2612, 6th AIAA Atmospheric and Space Environments Conference, Atlanta, GA, June 2014.

[91] Kreeger, R. E., Sankar, L. N., Nucci, M., and Kunz, R., "Progress in Rotorcraft Icing Computational Tool Development," SAE Technical Paper 2015-01-2088, 2015, doi:10.4271/2015-01-2088.

[92] Wright, J., Aubert, R., “Icing Wind Tunnel Test of a Full Scale Heated Tail Rotor Model,” American Helicopter Society 71st Annual Forum, Virginia Beach, Virginia, May 5–7, 2015.

[93] Jeewoong Kim, Lakshmi Sankar, Jose Palacios, and Richard E. Kreeger, " Numerical and Experimental Studies of Rotorcraft Icing Phenomena," 41th EUROPEAN ROTORCRAFT FORUM, 2015.

[94] Laforte J.-L. and Allaire M. A., Évaluation du givromètre d’Hydro-Québec à différentes intensités de givrage sec et humide, Hydro-Québec, Études et Normalisation Équipement de Transport, Montréal, Québec, Canada, Rapport HQ-92-02, pp. 2.1-2.5, janvier, 1992.

[95] Bain, J., Cajigas J., Sankar L., Flemming, R. and Aubert, R., " Prediction of Rotor Blade Ice Shedding using Empirical Methods," AIAA-2010-7985, AIAA Guidance, Navigation, and Control Conference, Toronto, Ontario, Aug. 2-5, 2010.

[96] http://web.mit.edu/16.unified/www/SPRING/propulsion/notes/node118.html.

[97] Konstanty C. Masiulaniec, " A numerical simulation of the full two-dimensional electrothermal de-icer pad," NASA CR4194, 1988.

VITA

JEEWOONG KIM

Jeewoong Kim was born in Seoul, Korea. He graduated from Konkuk University, Seoul, Korea. He received a Bachelor degree in Mechanical and Aerospace Engineering from Konkuk University in February 2007 and Master's degree in Aerospace Information Engineering from Konkuk University, Seoul, Korea in February 2009. He joined Georgia Institute of Technology in fall semester of 2010 to pursue a doctorate in school of aerospace engineering.